

Chipless Wireless High-Temperature Sensing in Time-Variant Environments

Vom Fachbereich Elektrotechnik und Informationstechnik
der Technischen Universität Darmstadt
zur Erlangung des akademischen Grades eines
Doktor-Ingenieurs (Dr.-Ing.)
genehmigte

Dissertation

von

Diplom-Ingenieur
Bernd Kubina
aus Olpe

Referent: Prof. Dr.-Ing. Rolf Jakoby
Korreferent: Prof. Dr.-Ing. Martin Vossiek

Tag der Einreichung: 12. Juli 2016
Tag der mündlichen Prüfung: 04. November 2016

D17
Darmstadt 2017

Acknowledgment

The thesis at hand is a result of my work as a research assistant at the Institute for Microwave Engineering and Photonics of the TU Darmstadt. My sincere acknowledgment is therefore addressed to the whole institute and its surroundings.

At the head of the institute and at the beginning of my Ph.D. stands Prof. Jakoby. I wish to thank him for his long-termed trust and guidance. — Prof. Vossiek from the Friedrich-Alexander-Universität in Erlangen has been a valuable project partner and became co-examiner of this work. His efforts are addressed as well. — Core elements of the thesis have grown from an integral team work. Mr. Schüßler and Mr. Mandel are springs and members of this team. Their contributions can hardly be overrated. — A useful idea needs a skilled hand for realization. I am thankful for at least ten of them. They belong to our trustful technicians, Mr. Kießlich, Mr. Semrad, Ms. Boye and Ms. Schober, as well as to Mr. Heyse from the Institute Nichtmetallisch-Anorganische Werkstoffe of the TU Darmstadt. — Experts in the field of material science are Mr. Binder and Mr. Kohler from the Karlsruhe Institute of Technology. Their cooperation is very worth to be mentioned. — On the side of industry, I wish to acknowledge our project partners from the Siemens AG in Munich: Mr. Ziroff and Mr. Müller, who included a further facet with the topic of commercial RFIDs. — Finally, back in the office one sometimes finds topics beyond science. Many thanks to Mr. Mehmood and Mr. Schuster, as well as Mr. González Rodríguez and many more welcomed guests for keeping my head up by sharing their very positive vibes!

Darmstadt, December 2016

Abstract

The wireless sensing of various physical quantities is demanded in numerous applications. A usual wireless sensor is based on the functionality of semiconductor Integrated Circuits (ICs), which enable the radio communication. These ICs may limit the application potential of the sensor in certain specific applications. One of these applications stands in the focus of this thesis: the operation in harsh environments, e.g., at high temperatures above 175 °C, where most available sensors fail. *Chipless* wireless sensors are researched to exceed such chip-based limitations. A chipless sensor is setup as an entirely electro-magnetic circuit, and uses passive Radio Frequency (RF) backscatter principles to encode and transmit the measured value.

Chipless sensors that target harsh environment operation are facing two important challenges: First, the disturbance by clutter, caused by time-variant reflections of the interrogation signal in the sensor environment and second, the design of suitable measurand transducers. These challenges are addressed in the thesis. To overcome the first challenge, three basic chipless sensor concepts feasible for operation in clutter environments are introduced. The concepts are realized by demonstrator designs of three temperature sensors and are proofed by wireless indoor measurements. A channel estimation method is presented that dynamically estimates and suppresses clutter signals to reduce measurement errors. To overcome the second challenge, measurand-sensitive dielectric materials are used as measurement transducers, and are being characterized by a novel high-temperature microwave dielectric characterization method. Complex permittivity characterization results in temperatures up to 900 °C are presented.

Finally, in-depth description and discussion of the three chipless concepts is given as well as a performance comparison in wireless indoor measurement scenarios. The first concept is based on polarization separation between the wanted sensor backscatter signal and unwanted clutter. The second concept separates tag and clutter signals in the frequency domain by using harmonic radar. The third concept exploits the slow decay of high- Q resonances in order to achieve the desired separation in time domain. This concept's realization is based on dielectric resonators and has demonstrated the capability of wirelessly measuring temperatures up to 800 °C without requiring an optical line-of-sight. This performance significantly exceeds temperature- and detection-limitations of commercially available sensors at the current state-of-the-art.

Kurzfassung

Das drahtlose Messen diverser physikalischer Größen ist in zahlreichen Anwendungen notwendig. Ein klassischer drahtloser Sensor basiert auf der Funktionalität von integrierten Halbleiter-Schaltkreisen (ICs), welche die Funkkommunikation ermöglichen. In spezifischen Anwendungen können diese ICs jedoch das Anwendungspotential des Sensors begrenzen. Eine spezifische Anwendung steht im Fokus dieser Arbeit: der Betrieb in rauen Umgebungen, z.B. bei hohen Temperaturen oberhalb von 175 °C, in denen die meisten verfügbaren Sensoren nicht betriebsfähig sind. Dieser Umstand motiviert die Forschung an chiplosen drahtlosen Sensoren, um die chipbasierten Begrenzungen zu überschreiten. Ein chiploser Sensor ist als vollständig elektromagnetischer Schaltkreis aufgebaut und benutzt passive Rückstreuung von Hochfrequenz-Signalen um den Messwert zu verschlüsseln und zu übertragen.

Chiplose Sensoren, welche auf die Anwendung in rauen Umgebungen abzielen, begegnen zwei wichtigen Herausforderungen: Erstens, der Störung durch Clutter, welcher durch zeitvariante Reflektionen des Abfragesignals in der Umgebung des Sensors hervorgerufen wird und zweitens, dem Entwurf geeigneter Messwertumformer. Diese beiden Herausforderungen werden in der vorliegenden Thesis adressiert. Um die erste Hürde zu überwinden werden drei grundlegende chiplose Sensor-Konzepte eingeführt, welche auf die Realisierbarkeit in rauen Umgebungen mit Clutter abzielen. Diese drei Konzepte sind als Temperaturmessungs-Demonstratoren realisiert und in drahtlosen Messungen validiert worden. Es wird desweiteren eine Kanalschätzungsmethode für chiplose Systeme präsentiert, welche Clutter-Signale dynamisch schätzt und unterdrückt, um Messfehler zu minimieren. Zur Überwindung der zweiten Hürde werden Messwert-abhängige Dielektrika als Messwertumsetzer eingesetzt und in einer neuartigen Hochtemperatur-Charakterisierungsmethode im Hochfrequenzbereich analysiert. Ergebnisse der Charakterisierung von komplexen Permittivitäten bei Temperaturen bis 900 °C werden präsentiert.

Schließlich werden sowohl detaillierte Beschreibungen und Diskussionen der drei chip-losen Konzepte, als auch Leistungsvergleiche in Innenraum Mess-Szenarien vorgestellt. Das erste der drei Konzepte basiert auf der Trennung von Sensor-Nutzsignal und Clutter-Störsignal durch Polarisation. Das zweite Konzept trennt Sensor- und Clutter-Signale im Frequenzbereich durch harmonisches Radar. Das dritte Konzept nutzt das langsame Abklingen hochgütiger Resonanzen um die gewünschte Nutz- und Störsignal-Trennung zu erreichen. Die Realisierung des letzteren basiert auf dielektrischen Resonatoren und demonstriert das drahtlose Messen von Temperaturen bis 800 °C ohne die Notwendigkeit einer optischen Sichtverbindung. Diese Leistung erweitert bestehende Detektions- und Temperatur-Begrenzungen kommerzieller Sensoren auf dem aktuellen Stand der Technik signifikant.

Contents

Abstract	iii
1. Introduction	1
1.1. Motivation and Structure	1
1.2. Wireless Temperature Sensors	3
1.2.1. State-of-the-Art of Commercial SAW and Chip-based Sensors	3
1.2.2. Recent Developments of Chipless Temperature Sensors	7
2. Fundamentals of Chipless Wireless Sensors	13
2.1. Passive Backscatter Principles	13
2.2. Chipless Modulation and Sensor Setup	18
2.3. Challenges of Chipless Sensor Systems	20
2.3.1. Challenges related to High-Temperature Sensing	20
2.3.2. Challenges related to the Wireless Communication	22
2.3.3. A basic scenario example	24
2.4. Clutter Countermeasures	26
3. Dielectric High-Temperature Transducers	31
3.1. Materials and Material Characteristics	32
3.2. Microwave High-Temperature Material Characterization	36
3.2.1. Modes and Radiation Characteristics of Dielectric Resonators	37
3.2.2. Resonant High-Temperature Characterization Method	48
3.2.3. Characterization Results	56
4. Chipless Sensing Concepts	59
4.1. The Dual-Polarization Concept	59
4.1.1. Depolarization effects	61
4.1.2. Crosspolar Sensor Tag	66
4.1.3. Sensor Simulations and Measurements	68
4.2. The Harmonic Radar Concept	73
4.2.1. Harmonic Radar Sensor Tags	75
4.2.2. Wireless Measurements and Temperature Sensing	84
4.3. The High-Q Resonator Concept	87
4.3.1. Dielectric Resonator Sensor Tag	89
4.3.2. Wireless High-Temperature Measurements	92
4.4. Comparison and Proof of Concepts	96
4.4.1. Test Scenarios and Measurement Setups	96
4.4.2. Results and Discussion	98

Contents

5. Dynamic Clutter Estimation	109
5.1. Clutter interference	109
5.2. Estimation Method	113
5.3. Measurements	117
5.3.1. Measurement Setups	117
5.3.2. Measurement Results	123
6. Conclusion and Outlook	127
A. Appendix	131
B. Acronyms	133
Bibliography	137
Own Publications	147

1. Introduction

1.1. Motivation and Structure

The onset of the 21st century is witnessing a tremendous increase in the number of installed sensors worldwide. The trend covers sensor applications in various control and monitoring tasks as found in industry, logistics, medicine and consumer electronics. From a business perspective, the increase is globally noted and forecasted with annual market growth rates of at least 7% in the first decades of this century [Con], [Inc]. From a technology perspective, the increasing number of sensors is seen in close relation to the emergence of the Internet of Things, a visionary network of physical objects embedded with electronic communication technology. This vision includes pervasive sensing in the living environments of a smart city and in the production environments of the Industry 4.0. It is motivated by the prospect of economical and ecological benefits, as sensing elements allow for increasing process efficiencies.

Part of the development is the increasing employment of wireless sensors, which are based on radio communication. Compared to a wired sensor, a wireless sensor tag can offer significant advantages, when the tagged object is moving, far away or otherwise hard to access. Selective interest arises in the development of wireless sensors for specific applications, which cannot be served by commercially available sensors at the current state-of-the-art. Such specific applications are found when either very low costs of the sensor node, or its operation in harsh environments is demanded. A harsh environment can for example require operation of the sensor in high temperatures, or under nuclear radiation. It can furthermore require a high integration of the sensor into a product or production cycle as well as high reliability and durability over years.

The case of high-temperature operation is highlighted: silicon-based Integrated Circuits (ICs) are core elements of usual sensor nodes, and reach their temperature operation limit below 175 °C. But various potential sensor application scenarios demand for significantly higher temperature ranges, e.g., in metal foundries, where the temperature of a workpiece shall be controlled from a nearly liquid state to room temperature, in a turbine engine, where measurements of temperature and gas concentrations offer crucial information concerning blade lifetime and combustion efficiency, and in automated metal working, where temperature and torque of drill bits or milling cutters deliver valuable information about the tool wear.

In order to serve such specific application scenarios, *chipless* wireless identification and sensing systems are researched. The chipless system consists of an active reader unit, and a passive ID or sensor tag that is interrogated wirelessly. The chipless sensor

1. Introduction

is setup as an entirely Electro-Magnetic (EM) circuit, and avoids the implementation of integrated semiconductor circuits. It does not require a local power supply and excludes means of energy harvesting. Instead, chipless sensors use passive EM backscatter mechanisms on radio frequencies, usually between 0.5 GHz and 30 GHz. The basic functionality of a chipless system is therefore related to radar principles and the backscatter signal of the sensor tag carries the wanted measurement information. As a consequence, chipless systems can overcome chip-based limitations. Nevertheless, a chipless system has to face unwanted radar clutter interferences, which are caused by reflections of the interrogation signal in the environment of the sensor. This interference is especially critical when the clutter signals are overpowering the wanted tag response and are time-variant due to movements in the environment. It results, that clutter often represents the largest challenge for a successful chipless wireless tag detection.

The main goal of this thesis is the development of a chipless temperature sensor that targets operability in harsh environments, such as in the highlighted high-temperature scenarios. As derived from the scenario considerations, the technical goals of this chipless sensor include: 1) wireless detection in spite of strong and time-variant clutter, as expected due to moving, rotating and vibrating metallic components in the environment; 2) temperature measurement capability in ranges beyond the chip-based limit, i.e., above 175 °C; 3) operability without requiring a strict optical line-of-sight between reader and sensor, as moving elements, such as machine components, dirt or cooling liquids often reduce the optical visibility; and 4) a reasonable large wireless reading range, as hot or moving elements require a certain distance between tag and reader antenna.

All four goals are addressed in the thesis. The first goal of operability under clutter occurrence represents one core motivation. The thesis presents therefore a general investigation of three chipless concepts. These three concepts are based on a physical separation of tag and clutter signals either in Time Domain (TD), in Frequency Domain (FD) or by polarization. Each concept is fundamentally introduced, carried out by a practical sensor realization and validated in wireless measurements. Performance aspects of the concepts are analyzed and compared in indoor measurement scenarios. In extension of these concepts, a channel estimation approach has been developed for chipless systems. The approach targets a further suppression of clutter interferences and the reduction of measurement errors. The three developed concepts as well as the channel estimation method are generally not limited to a specific measurand, but are suitable for various physical quantities. Nevertheless, in this thesis, an exclusive implementation of the temperature sensing is taken, because it allows for a direct comparison of the concepts and because temperature is one of the most widely sensed variables in industry.

The second goal of high-temperature sensing and high-temperature operation leads to the question of a suitable measurement transducer. Under consideration of the mentioned chipless core concepts, this question is reasonably answered by measurand-sensitive dielectrics. Sufficient knowledge of the complex microwave dielectric properties of potential transducer materials is therefore a prerequisite in the

chipless design process. For this purpose, a resonant high-temperature characterization method has been developed and applied.

The structure of this thesis is as follows. A short review on the state-of-the-art of commercially available wireless temperature sensors and on relevant publications on chipless sensors is given in Section 1.2. It is followed by an introduction to the chipless working principles and to challenges concerning chipless sensing in harsh environments in Chapter 2. Chapter 3 discusses dielectric transducer materials and the associated high-temperature characterization method. Afterwards, Chapter 4 presents the three chipless core concepts and developed sensor tags, which includes the dual-polarization concept in Section 4.1, the frequency domain separation concept based on harmonic radar in Section 4.2, as well as the time-domain separation concept based on high- Q resonances in Section 4.3. The chapter is concluded with a performance comparison in Section 4.4. On the final stage, the proposed channel estimation method is described and applied in Chapter 5.

1.2. Wireless Temperature Sensors

Temperature sensors are one of the most widely used sensor types. They are used in numerous applications and as each application brings different demands, a large variety of temperature sensor technologies have been developed. This section gives a classification of commercially available state-of-the-art temperature sensors, as well as an overview on recent works on electromagnetic chipless wireless temperature sensors.

1.2.1. State-of-the-Art of Commercial SAW and Chip-based Sensors

A categorization of different temperature sensing technologies is given in Figure 1.1. The largest amount of employed temperature sensors are *wired* sensors. One representative are resistance thermometers, where the dependence of the electrical conductivity of a certain metal on temperature is used. An example is the classical platinum resistance thermometer, like the Pt100, which is usually used in ranges up to 600 °C [SAB]. A second representative of this group is the thermocouple, which uses the thermoelectric Seebeck effect: if the ends of two one-sided connected metals are exposed to a temperature difference, an electric potential difference is generated. Thermocouples are commonly used in ranges up to 1300 °C [SAB] and have been used in ranges up to 2300 °C in special applications [Kör98]. Further wired sensors are, e.g., fiber optical distributed systems, based on the Raman effect or silicon bandgap sensors. The latter ones use the temperature-dependence of the built-in potential of p-n junctions. As mentioned below, silicon bandgap sensors are also found in chip-based *wireless* sensors, as they are easily integrated in silicon ICs.

The group of *wireless* sensors can be divided into optical, electro-acoustic and purely electromagnetic types. Optical sensors detect thermal radiation, that is emitted by any body warmer than 0K. According to the Stefan-Boltzmann law, the

1. Introduction

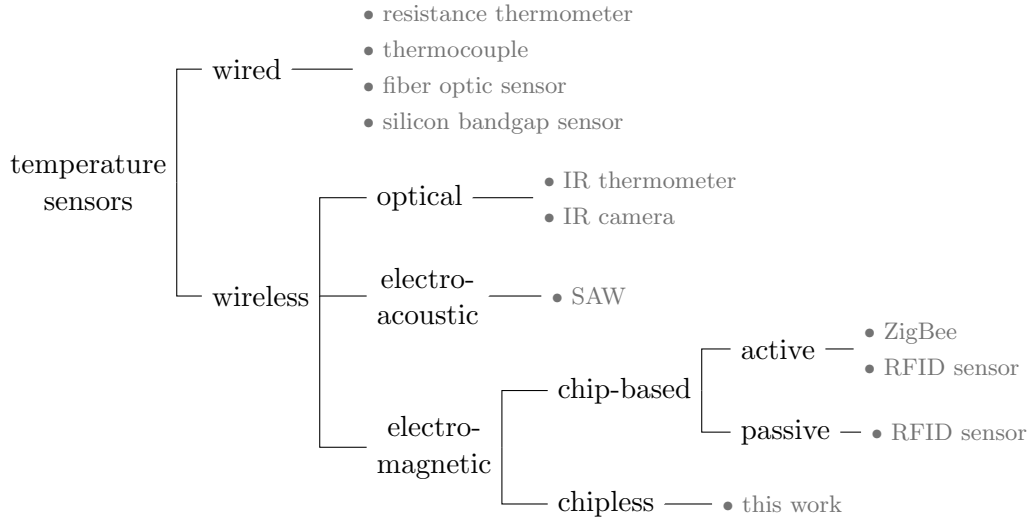


Figure 1.1.: Categorization of temperature sensors.

power P_t radiated from a body grows quartic with temperature, i.e., $P_t \propto \varepsilon_t \vartheta^4$ when ε_t describes the body's material emissivity constant. Wireless optical temperature sensors are, e.g., Infra-Red (IR) cameras and IR thermometers. Commercial products are available for temperature ranges from -40°C to 2000°C [Flu]. Optical sensors are widely used, yet they have drawbacks in three aspects: (1) they require a direct line-of-sight to the measurement point, any obstacle in the line disables the measurement; (2) secondary IR radiators in the environment can lead to faulty measurements, when their IR radiation superimposes with the targeted body's radiation. This can be due to reflections or through-the-target transmission of the secondary radiation; (3) The emissivity constant ε_t is in general material-, frequency- and temperature-dependent. Hence, an accurate measurement requires knowledge of the target material's specific emissivity. Especially metallic objects are hard to measure as their emissivities are low and their IR reflection coefficients are high, especially for planar and smooth surfaces.

The two latter representatives of the wireless group, electro-acoustic and fully electromagnetic chip-based sensors are focus of the following two subsections.

Electroacoustic SAW sensors

Passive wireless sensor and Radio-Frequency Identification (RFID) transponder that are based on Surface Acoustic Wave (SAW) propagation are commercially available. SAW transponder are builtup as an antenna that is connected to a piezoelectric crystalline substrate. Interdigital transducers and reflectors are usually placed onto the substrate as planar metal electrodes. An incoming RF signal will cause surface charge displacement on the substrate which then leads to elastic deformation of the crystal grid based on the piezoelectric effect. The elastic deformation then propagates

on the substrate as an acoustic surface wave. Reflections of the acoustic wave, that are caused by the planar electrodes, will be re-transduced to an electric signal and backscattered towards the SAW reader. [Fin03]

SAW temperature sensors use the temperature-dependence of the propagation velocity of the acoustic wave on the substrate. The difference in propagation delay between reflector elements is used for temperature measurements [Sch+98].

SAW sensors are offered for temperatures up to 400 °C [CTR]. Operation of SAWs in temperature ranges above this point is the focus of research activities [Beh+13]. Difficulties that arise when operating SAWs at higher temperatures are:

- the temperature stability of the substrate,
- the temperature stability of the housing,
- the increasing transmission losses of the substrate, and
- the temperature instability of the electrodes, which includes metal agglomeration, diffusion, degrading, oxidation and loss of adhesion [Hor+98].

These difficulties can lead to a limited life-time and/or reduced backscatter power [BBF11], which in turn, reduces the operability. Typical reading ranges of SAW sensors at room temperature are between 1 m and 4 m, depending on the reader and tag antenna gain [BBF11]. [BBF11] reports a 70 % range decrease of an SAW tag operating at 300 °C in comparison to a tag operating at room temperature. The commercially available SAW sensor in [CTR] is specified for a reading range of 30 cm and an accuracy of ± 2 K for temperatures up to 400 °C.

Electromagnetic chip-based wireless sensors

A number of different chip-based wireless sensor systems are commercially available. These systems can be grouped into active chip-based and passive chip-based transponders. **Active** transponders are usually powered from a local battery and possess a full RF transceiver chain, including up- and downconversion, filtering and signal amplification. This group comprises sensors that operate in wireless local area networks (WLAN), bluetooth or ZigBee radio networks as well as active RFID sensors.

The most popular representative of the group of **passive** chip-based wireless transponders is the RFID. Passive RFID tags do not carry batteries. Instead, they harvest energy from the reader's Continuous Wave (CW) RF signal to power an IC. This powering is usually realized by a rectifier that consists of a diode and a capacitor in the simplest case. The transponder's response signal is generated by backscatter modulation. The basic functionality of this modulation principle is sketched in Figure 1.2. As explained in Section 2.1, any receiving antenna generates a backscatter wave, similar to RF reflection at a material boundary. Herein, the (complex) amplitude of the backscatter wave is strongly dependent on the antenna load. The passive

1. Introduction

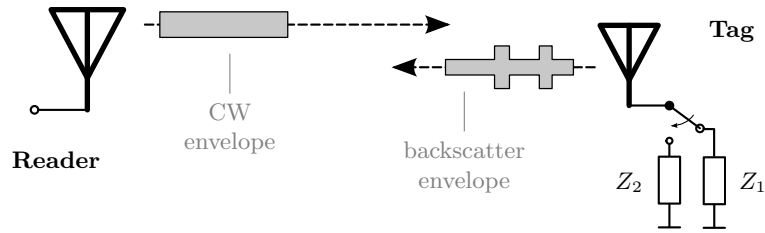


Figure 1.2.: Backscatter modulation in chip-based passive RFIDs.

transponder switches the load of its antenna between two impedance states, and consequently modulates the reflection envelope over time to encode data.

Based on this principle, passive RFID *sensors* have been developed, where both, reading of the tag ID and reading of a temperature measurement value is possible. The additional sensing functionality can be realized by implementing a silicon bandgap sensor inside the tag IC. The achieved measurement value can be transmitted to the reader under support of the UHF EPC Gen. 2 communication protocol with operation at 900 MHz. A few UHF RFID tag ICs with temperature sensing functionality have been realized in CMOS technology: [Yin+10] reports a sensor for temperature ranges from -20°C to 30°C with a read sensitivity of $P_{\min} = -6\text{ dBm}$ and a temperature measurement accuracy of $\pm 0.8\text{ K}$. [EM] offers a commercially available UHF IC for sensor-and-ID RFIDs for temperature ranges of -40°C to 60°C with a read sensitivity of -8 dBm and an accuracy of $\pm 1.0\text{ K}$. In comparison, commercially available UHF RFID chips without sensor functionality (i.e. for ID-only tags) have read sensitivities as low as -18 dBm [NXP]. The read sensitivity determines the minimal input power P_{\min} that has to be delivered to the tag's rectifier in order to power-up the IC. From this sensitivity, the forward-link read range d_{\max} of the passive RFID system can be derived. This range describes the maximum distance d_{\max} between tag and reader that still allows for this power-up. It is given by

$$d_{\max} = \frac{c_0}{4\pi f_0} 10^{(\text{ERP}_{\max} + G_T - P_{\min})/20} \quad (1.1)$$

where G_T describes the gain of the tag antenna (given in dBi), ERP_{\max} the equivalent radiated power level of the reader (given in dBm) and P_{\min} the above mentioned read sensitivity of the tag chip (given in dBm). For an operation frequency of $f_0 = 900\text{ MHz}$, an ERP level equal to the maximum of european regulations of 33 dBm , a dipole antenna with $G_T = 1.76\text{ dBi}$ as well as perfect power matching, this read range is calculated to 11.5 m for the ID-only RFID tag. The sensor-and-ID RFID will see a 68% smaller range with its 10 dB lower sensitivity. Its maximum range is 3.6 m under the same conditions.

Taking a look at the basic setup of such a chip-based transponder, it is obvious that the IC delivers core functionality, such as logic, control and signal handling. These functionalities are delivered from a number of diodes and transistors in the

circuit. Their basis are junctions of doped semiconductors. During standard operation of a semiconductor junction, conduction mechanisms are mainly based on the extrinsic carriers, which originate from the dopants. Intrinsic carriers, in contrast, can be excited across the bandgap, when the junction temperature rises. As a consequence, the number of intrinsic carriers will outnumber the extrinsic carriers for sufficiently high temperatures¹. This effect leads to malfunction of the junction and eventually to thermal breakthrough in the device [Pie96]. The temperature limit of a specific semiconductor material is dependent on its doping concentration and its bandgap energy. [TS02] names 175 °C as the upper application limit of usual silicon semiconductor circuits. Most commercially available ICs are specified to maximum operation temperatures of 125 °C (or less) for reliable operation [Wika].

Other semiconductor materials, such as gallium arsenide or gallium nitride, are used to develop high-temperature electronics as their bandgaps are significantly higher than the one of silicon. Yet, the development of semiconductor systems is connected to extensive costs, and silicon is a standard solution for mass market products. To the author’s knowledge, there is no commercially available chip-based wireless sensor, that is capable of operating in temperatures above 175 °C. This drawback motivates research on *chipless* sensors for high-temperature applications, especially when niche markets are addressed in specific application scenarios.

1.2.2. Recent Developments of Chipless Temperature Sensors

The focus of this thesis lies on chipless wireless sensors. Herein, the term *chipless* refers to a fully electromagnetic circuit, that acts as a passive backscatterer of RF signals. At this stage, an overview on recent publications on chipless temperature sensors is given to complement the intended overview of this chapter. It is noted, that the basic working principles and setups of chipless sensors are introduced in Chapter 2. A few expressions and understandings of Chapter 2 are therefore already anticipated.

Table 1.1 lists 19 different works on chipless temperature sensors, which are classified and compared². Herein, properties are listed that concern the setup of the sensor tags as well as indicators concerning their performance. The setup properties include the transducer, the information encoding, the structural form and the planarity of each sensor tag. The performance indicators include the proof of wireless operation, the maximum operation temperature and the reading range. The properties and indicators are briefly discussed in the following. All works of this comparison operate between 1 GHz and 30 GHz.

The first setup property concerns the temperature-dependent transducer and the transducer material of the sensor. [PK10] and [Gir+12] use commercially available SMD thermistors to modulate the amplitude of a signal with its temperature-dependent ohmic resistance. Bimorph metals are used in [Tha+10a], [SP09], and

¹Compare Appendix Section A for details.

²The given classification is partly based on the overview on chipless *RFID* tags and chipless *strain* sensors in [Man+13].

Table 1.1.: Publications on chipless temperature sensors.

Reference	Transducer material (principle)	Enc.	Struct.	Pl.	Wirel.	θ_{\max} (°C)	d (cm)	#
[AK11]	polyamide (TL resonator)	f	L.A.	✓		-	-	
[Man+11b], [Man+11c]	BST (capacitor)	Ph TD	L.A.	✓		100	-	
[PK10]	metal oxide (SMID resistor)	Am	L.A.	✓		100	-	
[Tha+10a]	bimorph metal (TL resonator)	f	S.A.	✓		-	-	
[Tra+11b], [Tra+11a]	microfluid (short circuit)	Am	L.A.	✓		-	-	
[Zai+14]	polyamide (slot antenna)	f	S.A.	✓		-	-	
[Boc+14]	ceramic (DR)	f	S.A.	✓	✓	700	120	1
[Bou+13]	microfluid (capacitor)	Am TD	L.A.	✓	✓	33	200	2
[CEG12]	ceramic (slot antenna)	f	S.A.	✓	✓	1000	3	3
[Che+15]	ceramic (slot antenna)	f	S.A.	✓	✓	1100	3	4
[Gir+12]	metal (SMD resistor)	Am TD	L.A.	✓	✓	130	100	5
[Kub+12a] ♦	BST (capacitor)	f	L.A.	✓	✓	85	100	6
[Kub+13b] ♦	ceramic (DR)	f	S.A.	✓	✓	370	80	7
Section 4.3.1 ♦	ceramic (DR)	f	S.A.	✓	✓	800	50	8
[Kub+14b], [Kub+14c] ♦	ceramic (DR)	f	L.A.	✓	✓	109	325	9
[Sch+14a]	BST (capacitor)	Am TD	L.A.	✓	✓	80	60	10
[SP09]	bimorph metal (slot antenna)	f	S.A.	✓	✓	300	10	11
[Tha+10b]	bimorph metal (TL resonator)	f	S.A.	✓	✓	60	15	12
[Gha+13], [TCB09]	metal (cavity resonator)	f	L.A.	✓	✓	145	400	13
[Ven+14a], [Ven+14b]	carbon nanotube (resistor)	Am	S.A.	✓	✓	55	20	14

Struct. Tag structure
in Figure 1.3
L.A. Loaded antenna
f Freq.-position Enc. in FD
♦ this work

Pl. Planar
S.A. Shorted antenna (resonator)
Am Amplitude Enc. in FD

Enc. Enc. Am TD Amplitude Enc. in TD

Encoding (Modulation)

Wirel. Ph TD Phase Enc. in TD

Wireless measurements

[Tha+10b], that are deflected by temperature-dependent material elongation. The bimorph structures detune capacities or resonators and hence, allow for modulation of resonance frequencies. The most commonly used material are ceramics with temperature-dependent permittivity. They are either low permittivity dielectrics with $\varepsilon_r < 100$ (called 'ceramic') as in [Boc+14], [CEG12], [Che+15], [Kub+13b] and [Kub+15], or the high permittivity ferroelectric Barium Strontium Titanate (BST) as in [Kub+12a] and [Sch+14a]. All named ceramic sensors, except [Sch+14a], use resonators for frequency-position modulation.

The second property concerns the encoding of the measurand, i.e., the chipless modulation as described in Section 2.2. Here, either amplitude, phase or frequency-position encodings are found and the Rx signal is either evaluated in time or frequency domain. Except for [Gir+12], [Bou+13] and [Sch+14a], all setups use FD evaluation. Furthermore, it becomes obvious that the majority of the setups uses frequency-position encoding of the measurand. This is probably due to its higher suitability for time-variant environments compared to amplitude modulations as discussed in Section 2.2.

The third setup property concerns the sensor structure. All setups are either realized as a loaded antenna (L.A.) or as a shorted antenna/resonator (S.A.), as referred to in Section 2.2. In the former case the temperature transducer either directly forms the load of the antenna or it is embedded in circuitry elements that load the antenna, such as delay lines or filters. The loaded antenna category also includes tags with two antennas. In the latter case, the tag is setup basically as a resonator and the measurand influences this resonator directly.

The last setup property relates to the structural form. Nearly all publications are setup as planar circuits. Only [Bou+13] and [Gha+13] use coaxial cables and horn antennas on the tag side, what makes their setups more bulky and probably only suitable for a few applications³.

Taking a look at the performance indicators, first the verification of the chipless sensor functionality in wireless measurements is noted. This indicator is fulfilled by 13 of 19 publications. Six publications present only simulation or conceptual results.

The second performance indicator is the maximum operation temperature as given in the publication. Many of the publications present operation up to modest temperatures below 100 °C. [SP09; Kub+13b; Boc+14; CEG12; Che+15] prove operability in the high-temperature regime, above the 175 °C limit of silicon. This high-temperature regime is of special interest in this thesis due to its strong link to harsh environment applications.

The third performance indicator is the wireless reading range. As most publications do not directly specify a *maximum* range, the distance d between reader and tag antennas, as given in the wireless setup of each publication, is noted to approximate the range. The reading distance is of special interest when environmental constraints such as high temperature, nuclear radiation, or the movement of machines forbid

³The application scenario of structural health monitoring reasons the non-planar setup of [Gha+13] well and operability of this sensor with a compact loop antenna has also been demonstrated.

1. Introduction

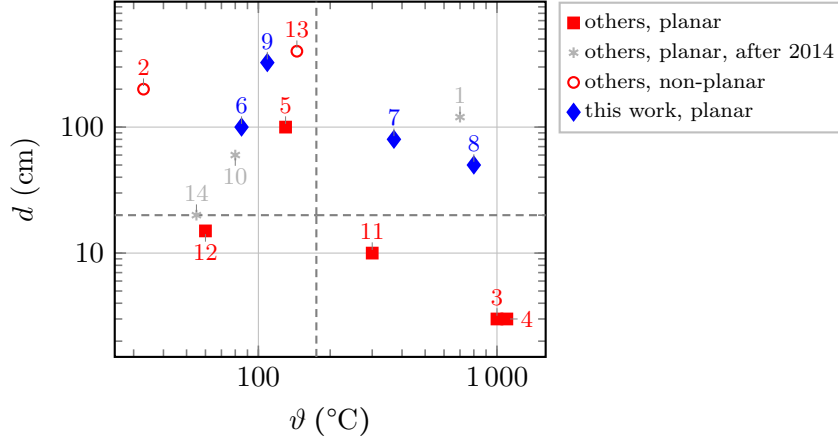


Figure 1.3.: Maximum temperature and reading distance of publications on chipless temperature sensors; Table 1.1 refers.

a short-range placement of the reader unit. The possibility to operate with a large remote distance is expected to be generally beneficial in many applications.

Here, it should be noted that the reading range is usually affected by the constitution of the sensor environment. The impact of clutter and noise (compare Section 2.3) as well as the desired measurement accuracy influence the maximum range⁴. In spite of the lack of perfect comparability at this stage, the range as it is given in the publications is still believed to be an acceptable indicator for the wireless reading quality. Yet, it should not be seen as a very absolute number. Reported reading distances range from 3 cm to 4 m. [CEG12], [Che+15], [SP09] and [Tha+10b] report distances below 20 cm.

Figure 1.3 depicts the two performance properties, range and maximum temperature of all publications that prove wireless reading. Published sensors that are non-planar are marked in the figure, as they can profit in terms of reading range when using horn antennas on the tag side. This profit comes at cost of a significantly larger transponder volume. Inside the figure, also the 175 °C limit and the 20 cm range limit are marked. The 175 °C limit is taken from the mentioned temperature limit of silicon ICs, and marks the onset of the high-temperature regime as understood in this thesis. The 20 cm range limit is understood as a minimum reading distance where operation of wireless sensors in harsh environments becomes applicable. Moving elements in an application environment often require a certain distance between reader and sensor. Furthermore, sensors operating below this limit are likely operating in the reactive near field of the reader antenna, and might therefore be assigned to inductively coupled systems rather than far-field systems.

The publications that evolved out of this thesis are marked in blue in the figure. To

⁴A discussion of the impact of the environment constitution on the range of the sensors of this thesis is found in Section 4.4

1.2. *Wireless Temperature Sensors*

the author's best knowledge, among these publications is the first chipless wireless sensor that has been capable of operating beyond both, the 20 cm and the 175 °C limit [Kub+13b]. Furthermore, there is the first chipless temperature sensor that uses polarization separation of clutter and tag response [Kub+12a], as well as the first realized harmonic radar sensor with frequency-position encoding [Kub+14b]. Finally, it is noted that this harmonic radar concept has enabled the design of the sensor with the largest reading range among all planar setups [Kub+15].

2. Fundamentals of Chipless Wireless Sensors

This thesis investigates chipless sensors. As detailed design and performance aspects of the developed sensors are given in the subsequent main chapters, first an introduction to the underlying chipless principles is given.

A chipless system mainly consists of two elements: a reader, also called interrogator, and a sensor, also called tag, sensor tag, or transponder. In a wireless reading scenario, tag and reader are inside the measurement environment and the tag is facing the reader antenna as shown in Figure 2.1.

The attribute *chipless* in the term *chipless system* refers to the sensor tag only and not the reader. A chipless sensor is understood as a passive wireless sensor that works entirely electromagnetic and that does not employ integrated semiconductor circuits, i.e., ICs and microchips. Furthermore, it does not possess any local power supply like batteries or energy harvesting devices and its operation frequency is within the microwave frequency range, typically between 0.5 GHz and 50 GHz.

The reader is an active element in the chipless system. It usually consists of an RF source, one or two antennas, an RF receiver and a control and evaluation unit. During a reading process, the reader sends an RF signal towards the tag and receives the sensor's response signal, which is generated by passive backscattering of the interrogation pulse by the sensor tag. Subsequently, the reader evaluates the response and derives the measurement value.

The wireless path from the reader towards the tag, the generation of the tag's backscatter response and the wireless path back towards the reader are standing in the main focus of this thesis. Three basic concepts to realize this wireless 'core' are presented and discussed throughout the work.

All three concepts, as well as all previously listed publications in Section 1.2.2, are based on passive backscatter principles. Passive backscattering of RF signals is therefore introduced in the following Section 2.1. Section 2.2 introduces the basic setup of a chipless sensor tag that results from using backscatter principles. Section 2.3 describes challenges that are inherited from the wireless backscatter principle and challenges that arise when targeting high-temperature operation.

2.1. Passive Backscatter Principles

The backscatter principle is based on reflection of EM waves by passive objects. The Fresnel equations describe reflection and transmission of incident planar waves at planar boundaries. For objects which are infinitely large, or at least large compared

2. Fundamentals of Chipless Wireless Sensors

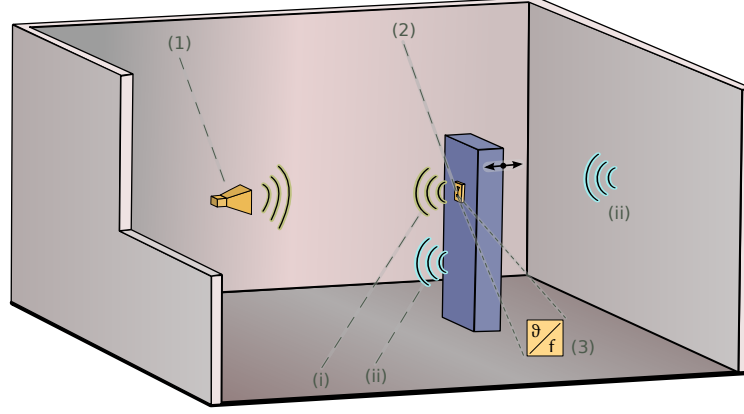


Figure 2.1.: Chipless wireless system in an indoor environment: The reader (1) transmits an RF pulse towards the sensor tag (2), which is equipped with a measuring transducer (3). The wanted tag response (i) and unwanted clutter (ii) from static and moving objects is backscattered.

to the wavelength a reflection factor γ_m can be defined. It depends on the object's material as well as on the field orientation and angle of incidence of the wave. In the simplest case, when a free-space wave incides orthogonal to the object, the reflection coefficient becomes

$$\gamma_m = \frac{Z_m - Z_0}{Z_m + Z_0} \quad (2.1)$$

where the free-space wave impedance is given by $Z_0 = \sqrt{\frac{\mu_0}{\epsilon_0}} \approx 377 \Omega$ and the object material's wave impedance

$$Z_m = \sqrt{\frac{j\omega\mu_m}{\kappa_m + j\omega\epsilon_m}} \quad (2.2)$$

is given in dependence of the material's conductivity κ_m , permittivity ϵ_m and permeability μ_m . The electric and magnetic field vectors of the reflected waves are directly proportional to this reflection factor and to the magnitude of the incident vector. Hence, the reflected power scales proportional to the square of γ_m . Metallic planes with a high conductivity have reflection factors close to -1, i.e., nearly 100 % of the incident RF power is reflected. Dielectric materials such as plastics, glasses, concrete or brick have relative permittivities between 3 and 9, leading to reflection coefficients between 0.27 and 0.5, i.e., 7 to 25 % of the incident power is reflected by the dielectric.

For objects with arbitrary shape and size, the Radar Cross Section (RCS) is commonly used to describe the amount of backscattered RF power. The RCS σ is defined as the magnitude of the reflected power density S_r at an observer point that is spaced by distance r_0 from the object, in relation to the magnitude of the incident

power density S_i at the object position

$$\sigma = 4\pi r_0^2 \frac{S_r}{S_i}. \quad (2.3)$$

Herein, the observer point is distant enough to assume plane wave propagation. The RCS of a specific object, also referred to as radar target, generally depends on its shape, size and material as well as on the wavelength. Furthermore, the orientation of the object to the incident wave as well as to the observer position is of importance. For a monostatic RCS, excitation and observing direction are identical, whereas they are different in a bistatic RCS measurement.

In the monostatic scenario, where the reader's Rx and Tx antennas are identical and have gain G_R , the radar equation

$$P_{\text{Rx}} = \frac{\lambda^2}{(4\pi)^3 d^4} P_{\text{Tx}} G_R^2 \sigma \quad (2.4)$$

describes the Rx power P_{Rx} , received from a scattering object with a certain RCS at distance d . It becomes obvious, that the Rx power is directly proportional to the RCS.

The optical backscatter region is defined as the frequency range where the size of a scattering object is significantly larger than the operation wavelength. In this region the RCS of a metal sphere with radius r_s is independent of wavelength and equal to πr_s^2 . Hence, a metal sphere with a diameter of approximately 1.13 m has an RCS of 1 m^2 . The RCS of a flat metal sheet with area A_p can be approximated as

$$\sigma_s = \frac{4\pi A_p^2}{\lambda^2} \quad (2.5)$$

for normal frontal incidence [Sko08]. At an operation frequency of 3 GHz, a 1 m^2 RCS will be reached by a 16.8 cm long, square sheet. Due to its shape the sheet backscatters significantly more directive than the sphere, so that a smaller physical area can lead to a larger equivalent backscatter area and to a larger backscatter power density in a certain direction.

Taking a look at slightly more complex structures, the backscattering of a tag that possesses an antenna is of high relevance in chipless systems. An RF field, that incides onto an antenna, will couple energy from free space into the antenna load. This is the classical purpose of an antenna. But as currents (and fields) are induced in the antenna, these alternating currents (and fields) will themselves re-induce fields and consequently, re-radiate power into free space. In an equivalent circuit that describes the *transmitting* mode of an ideal antenna, the antenna is usually modeled as a complex impedance $Z_A = R_A + jX_A$ and the power that dissipates in the radiation resistance R_A is radiated. In the *receiving* mode of this antenna the exciting incident RF field is represented by a source and the antenna load Z_L is connected to the antenna terminals as shown in Figure 2.2a. The antenna impedance Z_A can be

2. Fundamentals of Chipless Wireless Sensors

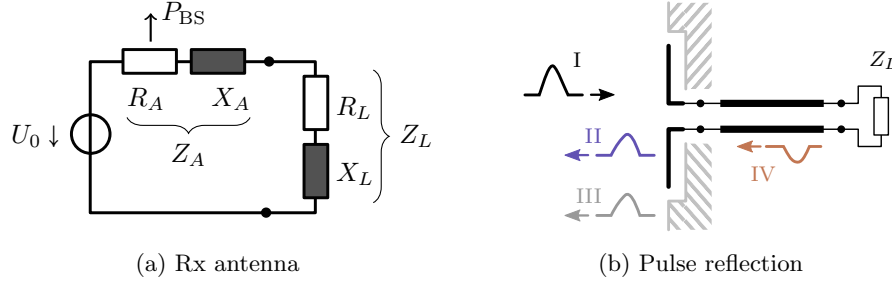


Figure 2.2.: (a) Equivalent circuit of an antenna in Rx mode with antenna impedance Z_A and load impedance Z_L ; (b) Pulse reflection from an antenna: incident pulse (I), structural mode (II), structural reflection (III) and antenna mode (IV).

considered as the generator impedance of the circuit. The power that now dissipates in the ohmic radiation resistance is exactly the re-radiated backscatter power.

As a consequence, one is able to describe the radar cross section RCS_A of an antenna in dependence of its gain G_T , impedance and load. Following the derivation of [NR06], it is given by

$$\sigma_A = \frac{\lambda^2 R_A^2}{\pi |Z_A + Z_L|^2} G_T^2. \quad (2.6)$$

It is observed, that the power density of the wave that reflects from the antenna is proportional to the square of the antenna gain and proportional to the radiation resistance R_A relative to X_A . The latter appears reasonable as the power that dissipates in the imaginary part X_A , does represent stored near-field energy and does not contribute to radiation. In terms of the antenna load, three specific cases of equation (2.6) are noted:

1. if the antenna is terminated with a perfect open, $Z_L \rightarrow \infty$, the RCS vanishes to zero, as there is no current in the equivalent circuit;
2. for the case of a matched load, $Z_L = Z_A^*$, the RCS becomes $\frac{1}{4} \frac{\lambda^2 G_T^2}{\pi}$. If load and antenna impedances are also real-valued, $Z_A = R_A = R_L$, one achieves the maximum possible power transfer from the incident wave to the load. In this case there is as much power delivered to the load as re-radiated into free-space;
3. in the case of a shorted load, $Z_L = 0$, and a real-valued antenna impedance, the backscatter power comes to a maximum. Then, the antenna RCS is

$$\sigma_{A,s} = \frac{\lambda^2 G_T^2}{\pi}, \quad (2.7)$$

and four times larger than in the case of a matched load.

One observes that shorted antennas can be used to generate comparatively strong backscatter signals. This aspect is used in backscatter modulators in chip-based systems, where the antenna load is switched from a matched case to a high-reflection case and in a number of chipless approaches, such as mentioned in Section 1.2.2.

The RCS of a shorted antenna is compared to the RCS of a flat metal sheet in Figure 2.3. The figure indicates that the above mentioned 16.8 cm square sheet has the same RCS = 1 m² as a shorted 12.5 dBi antenna at 3 GHz.

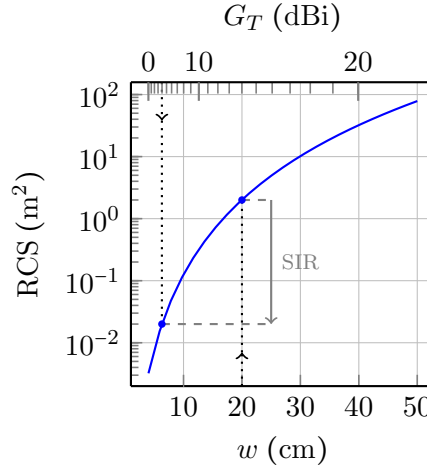


Figure 2.3.: Radar Cross Section (RCS) of a square metal sheet with edge length w , according to (2.5), and of a shorted antenna with gain G_T , according to (2.7), at 3 GHz. The SIR of Section 2.3.3 is marked as an example.

If we now move from a CW consideration to a pulse system, a further aspect of antenna backscattering can be considered. Figure 2.2b, shows an RF pulse which incides onto an antenna that is connected to a transmission line and a load. The incident pulse (I) will cause an initial reflection at the radiating element, e.g. the dipole wire, due to re-excitation as mentioned above. Furthermore, pulse energy will be coupled onto the transmission line. This energy can dissipate in the load, as well as be reflected by the load and backscattered by the antenna. For a short pulse or a long transmission line, the antenna backscatter signal can hence be divided into a *structural mode* (II), i.e. the initial backscatter of the antenna structure and an *antenna mode* (IV), i.e. the secondary backscatter from the load. Case (1) of the antenna RCS of Equation (2.6) may then be interpreted as the case where the structural mode (II) superimposes with the antenna mode (IV) with a 180° phase-shift, leading to a vanishing sum signal. Case (2) may be interpreted as the case of vanishing antenna mode, due to perfect absorption in the load. Then, only the structural mode (II) can be received. Case (3) describes the case of constructive interference between antenna mode (IV) and structural mode (II) that leads to a maximum RCS. For a sufficiently high time- and pulse-resolution, the single backscatter modes become distinguishable in TD [Lin89]. Consequently, the RCS becomes a time-dependent

2. Fundamentals of Chipless Wireless Sensors

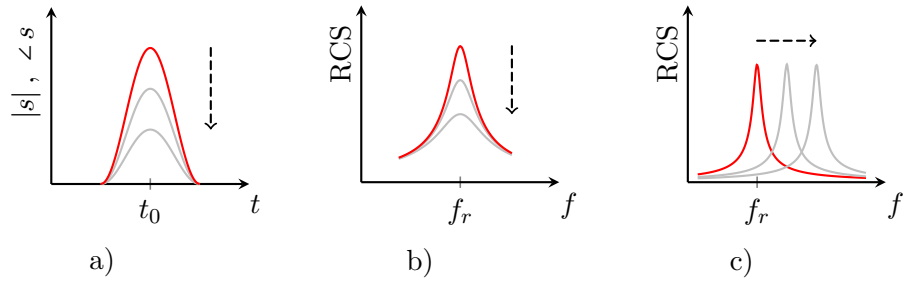


Figure 2.4.: Chipless modulation types: a) amplitude-modulation or phase modulation of the Rx signal s in Time Domain (TD), b) amplitude modulation of the RCS in Frequency Domain (FD), c) frequency-position modulation of a FD signature.

function.

Furthermore, it is noted that the structural mode (II) often directly superimposes with structural reflections (III), such as reflections from the close environment of the antenna (e.g. housing, mounting) or from the antenna ground (e.g. for a patch antenna). This can lead to practical difficulties when trying to determine and differentiate the antenna mode.

2.2. Chipless Modulation and Sensor Setup

Chipless transponders encode measurement information in the backscatter signal. This information is decoded in the reader by measuring and evaluating the backscatter signal. This information encoding can only be realized under consideration of the specific chipless limitations. The lack of (integrated) logic and control functionality makes it very difficult to generate a time-switched carrier-modulated signal. Instead, chipless sensors allow the measurand transducer to directly influence properties of the RF backscatter signal. This influence, i.e. the encoding of information on the tag, is denoted as chipless modulation. Chipless modulation can be distinguished from chip-based modulation by the determination of the system bandwidth. In the latter case, the bandwidth is determined by the modulator, i.e. by the modulation spectrum, whereas in the former case the bandwidth is determined by the reader source and the tag modulator has practically no influence on it¹.

Based on the discussion in [Man+13], the influence of the transducer onto the backscatter signal can either be evaluated in a TD signal observation, referring to time-domain signatures, or in a FD observation, referring to frequency-domain or spectral signatures. In general, these two signature types can be combined with either phase-, amplitude- or peak/pulse position- tuning. This results to six possible chipless modulation types, of which mainly four types are used in literature on

¹except for attenuation of frequency components

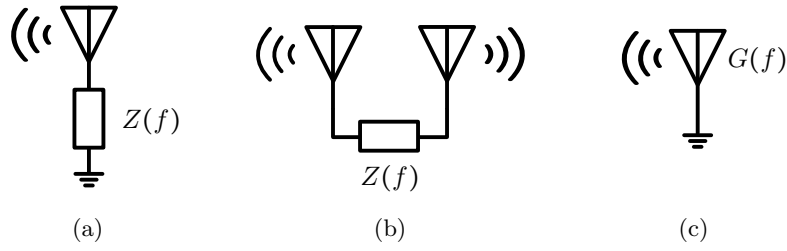


Figure 2.5.: Chipless tag types: (a) loaded antenna, reflection type, (b) loaded antenna, transmission type, and (c) shorted antenna.

chipless sensors. The four principles are sketched in Figure 2.4 and described as:

- *Amplitude modulation of a TD signature* is usually realized by implementing a measurand-sensitive antenna load that leads to measurand-sensitive amplitude of the antenna mode;
- *Amplitude modulation of a FD signature* is usually realized by implementing a resonator, whose losses, and, hence, resonance amplitude is influenced by the measurand;
- *Phase modulation of a TD signature* can be realized by measurand-sensitive complex reflectors on a transmission line loading an antenna; and
- *Frequency-position modulation of a FD signature* is usually realized by measurand-sensitive detuning of resonances.

The term *modulation* may be interchanged by *encoding*. Publications concerning each type are referenced and compared in Section 1.2.2.

In order to implement chipless modulators, a chipless transponder basically comprises an antenna and a load. Yet, a large variety of possible realizations exists, in which each realization differs in its type of antennas, loads and their combinations. Nevertheless, it is possible to distinguish three typical transponder types, which are sketched in Figure 2.5:

- Loaded antenna, reflection type: the transponder receives and backscatters via one antenna, the load is generally complex as well as frequency-dependent and measurand-sensitive. The load can, e.g., be realized as a specifically terminated delay line or as a filter structure. All four modulation types can be realized by this structure.
- Loaded antenna, transmission type: the reader signal is received via a first antenna, coupled to the load and backscattered via a second antenna. The load is principally similar to the load of the first case.

2. Fundamentals of Chipless Wireless Sensors

- c) Shorted antenna: A single antenna receives the reader pulse and backscatters a measurand-sensitive response. Tags of this type usually use frequency-position modulation.

Tag types a) and b) have in common that the load accounts for the encoding of the measurement information. These two types are referred to as 'loaded antenna' (L.A.) in the comparison of Section 1.2.2. Tags of type c) are usually realized as resonators or antenna-like resonators. They are referred to as resonance 'particle' in some publications (e.g. [Man+12]) and denoted as 'shorted antenna' (S.A.) in the comparison of Section 1.2.2.

Concerning the modulation types, a short judgement shall be noted. The analog transmission of the backscatter signal over the radio channel inherits its convolution with the channel's transfer function in TD. For a single line-of-sight channel, the transfer function describes primarily a significant signal attenuation. This attenuation is strongly dependent on the reading range, on the orientation of the antennas, on the presence of media that influences the antenna radiation patterns and on the presence of lossy media on the propagation path. The amplitude of a wireless signal is, hence, highly susceptible to channel parameters. Based on this observation, a chipless amplitude modulation scheme is judged only weakly suitable for dynamic environments. The introduction of amplitude references might decrease the susceptibility to a certain degree [Sch+14a], yet, frequency-position modulation is believed to have higher suitability. The resonance position is not affected by any of the parameters of a single line-of-sight channel named above. Due to this, all developed sensor prototypes of this thesis use resonance-position encoding.

2.3. Challenges of Chipless Sensor Systems

Recalling the backscatter principle of chipless sensors, a couple of challenges arise in their design and operation. Important challenges for practical sensor operation are described subsequently. These challenges (or difficulties) are categorized into two groups, namely challenges that primarily concern the operation at high temperature and challenges that concern the wireless communication channel. This categorization is not to be seen in absolute terms, as cross-links and cross-influences between elements of the same and adjacent group exist, yet it is believed to ease the understanding. The categorization is depicted in Figure 2.6.

Concerning the goal of the development of a chipless high-temperature sensor, the challenges of material losses, related to the temperature, and the clutter, related to the wireless communication, often represent the largest hurdles. Their impacts and their mitigation are core topics of this thesis.

2.3.1. Challenges related to High-Temperature Sensing

The former group of high-temperature related challenges includes the material stability, the sensor transducer and RF material losses. These challenges are briefly

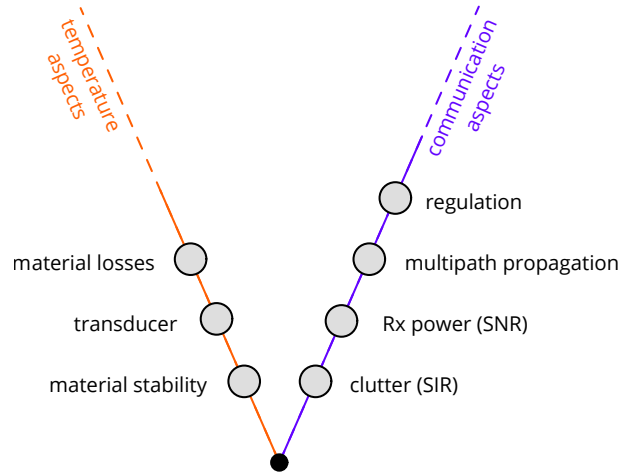


Figure 2.6.: Challenges of chipless sensors.

discussed.

Material stability

Chemical and mechanical material stability is of basic importance as high-temperature operation limits the number of applicable materials. Polymere molecules have melting temperatures typically below $180\text{ }^{\circ}\text{C}$ (Polyethylene), and even specially developed high performance plastics are only stable up to $260\text{ }^{\circ}\text{C}$ (Polyetherimide) [Wikb]. Hence, their applicabilty is strongly limited.

The limited suitability of doped semiconductor materials for circuits at high temperature is discussed in Section 1.2.1. Due to the increase of the intrinsic carrier concentration with temperature, the setup of controlled semiconductor circuits becomes very costly at high temperature, as Silicon ICs reach their limits below $175\text{ }^{\circ}\text{C}$.

Ceramics, in contrast, are usually sintered above $1100\text{ }^{\circ}\text{C}$ and are able to act as suitable dielectrics. Pure metals can form electric conductors up to their melting range, which can be between $660\text{ }^{\circ}\text{C}$ for aluminium and $1768\text{ }^{\circ}\text{C}$ for platin.

Aside from material melting, the material stability of metals is also reduced by corrosion/oxidation processes, diffusion processes, agglomeration and softening. These factors generally increase with increasing temperature. Herein, the increase of the reaction rates of the oxidation and diffusion processes versus temperature can be approximated by the Arrhenius relation.

Measurement transducer

Core element of each sensor is the transducer, which translates the physical measurand to an electric property. In a chipless system this transducer meets high demands as it directly modulates the RF signal. The transducer choice becomes even more difficult at high temperatures.

RF material losses

Due to increasing lattice vibrations material losses, including both conductor and dielectric losses of the RF signal, are usually increasing with increasing temperature. E.g., the conductivity of copper drops by a factor of 5.5 from room temperature to 1000 °C [Mat79]. Increasing conductor as well as dielectric losses inevitably lead to reduced antenna efficiency, increased transmission line loss and decreased resonator quality (Q) factor. These factors in turn lead to decreased Rx power in a chipless scenario and decreased measurement accuracy (compare Sections 4.3.1 and 4.4).

2.3.2. Challenges related to the Wireless Communication

The second group of challenges relates to wireless communication aspects. Herein, the signal detection and signal superposition play important roles. It includes the radar clutter, the weak Rx power, multipath propagation effects as well as legal frequency regulation.

Clutter

The direct reflection of RF waves from passive objects has been introduced in Section 2.1. In radar systems, the term clutter, or radar clutter, describes all unwanted reflections of the RF signal from objects in the ambience of the target. These ambient reflections are (at least partly) received by the reader and superimpose with the wanted target signal. In contrast to classical radar, where, e.g., an airplane is surrounded by air and open space, chipless systems often operate indoors and the sensor is surrounded by plenty of clutter objects. Especially, regarding operation in harsh environments, many metal surfaces in the direct vicinity of the sensor are expected. These objects may include static elements (such as machine housings, mountings, etc.), as well as moving and vibrating elements (such as engines, conveyor belts, die cutters, milling tools, turbine blades, ...). Hence, clutter signals with strong amplitude and time-variant shape and phase have to be expected.

The superposition of this clutter with the sensor backscatter signal can be quantified by the Signal to Interference Power Ratio (SIR)

$$\text{SIR} = \frac{P_t}{P_{cl}}, \quad (2.8)$$

defined as the relation between the power received from the sensor tag P_t to the power of the sum of all received ambient clutter signals P_{cl} .

If we recall the considerations about the RCS of Section 2.1, it becomes obvious that the clutter power P_{cl} will generally scale with the surface area of the environmental objects and for indoor scenarios the surface area is obviously large. The sensor tag, in contrast, is desired to be small in order to be applicable. Consequently, the tag will inevitably show a small backscatter power P_t compared to the clutter power in many scenarios. This relationship is underlined by the scenario example in Section 2.3.3 and by the depiction in Figure 2.3.

The result are SIRs significantly smaller than 1, and the observation that the tag signal will likely drown in the superposition with unwanted signals, which may be several decades stronger. It is stated, that the clutter represents often one of the strongest limitations in a chipless system. For a proper tag detection, especially in time-variant environments, clutter countermeasures are necessary. Four countermeasures are presented and discussed in the main chapters of this thesis.

In addition to its absolute power, the time response of clutter signals is of special interest in chipless systems. The time response is basically depending on three parameters: first, the sensor environment, what includes the size, place and material of objects; second, the radiation pattern of the reader antenna, as it describes the amplitude and phase of the incident interrogation pulse; and third, the bandwidth of the Tx pulse as it describes the time-duration and spatial resolution of the stimulus.

Figure 2.7c sketches the clutter envelope in time domain that is caused by the environment example of Section 2.3.3. This envelope can qualitatively represent typical clutter signals of indoor reading scenarios. The clutter signal starts a few nanoseconds after the Tx pulse is transmitted. This delay relates to the wave's travel time from the source through the antenna into free space and backwards. The initial reflections from the environment will be received first and incide with largest amplitude. Yet, several echoes and multiple reflections from different objects will be received as well and lead to a certain signal decay over time. Depending on the size and material constitution of the room, the clutter decay can extent over some hundred nanoseconds.

Rx power

According to the radar equation (2.4), the Rx power from the sensor tag drops biquadratic with the tag-to-reader distance, $P_{\text{Rx}} \propto d^{-4}$. In other words, the tag-to-reader communication inherits a double free-space path loss. This double loss can be quantified to 84 dB for a distance of 1 m at 3 GHz and increases by 12 dB when doubling the distance. The circumstance of high path losses leads to low Rx powers at the receiver. Consequently, the relation between the powers of the Rx signal and of the receiver noise, usually denoted as the Signal to Noise Power Ratio (SNR), can become critically low. This requires low noise receivers and/or high gain reader antennas. The example of Section 2.3.3 will give a further discussion of this circumstance.

Still, it should be noted that in many chipless scenarios the clutter power is significantly larger than the noise power (compare Figure 2.7). Hence, the clutter interference and its SIR is often more critical than noise interference and its SNR.

Multipath propagation

Multipath propagation in a radio channel describes the superposition of a signal with itself and is caused by the occurrence of multiple propagation paths between transmitter and receiver of the signal. Each non-line-of-sight path is usually gen-

2. Fundamentals of Chipless Wireless Sensors

erated by one or several reflecting environmental objects in the surrounding of the line-of-sight path. In a chipless system, as in any backscatter system, the effect of multipath propagation can occur twice: first, on the Tx direction of the interrogation signal from reader to the tag, and second, on the reverse direction of the desired backscatter signal from tag to reader. The multipath effects on the two directions are generally not identical, as likely neither the radiation patterns of reader and tag are identical, nor are the environments symmetrical.

The multipath superposition can lead to two negative impacts in a chipless scenario: First, destructive superposition occurs when two travelling paths incide with travelling delays around 180° . Then reduced excitation power of the tag and reduced Rx power at the reader occurs. The desired Rx signal is now more vulnerable to noise and clutter. Eventually, the desired Rx signal might even be cancelled out completely. Second, multipath interference generally leads to a frequency dependence of the communication channel's transfer function. Thus, the amplitude of the transfer function shows ripples. Even if the decrease of the Rx power is uncritical, the rippled course may distort the spectrum of the backscatter signal and consequently lead to detection inaccuracy. Section 4.4 discusses aspects of multipath interference.

Frequency regulation

Legal frequency regulation and assignment can limit the operation of chipless systems in practical applications. Limits occur due to limited permitted Tx power, which itself limits reading distances in relation to noise and the SNR, and due to limited frequency ranges, which restrict the operation bandwidth of the chipless sensor.

2.3.3. A basic scenario example

In order to illustrate the aforementioned wireless communication-related challenges in a chipless system, a simple scenario example is regarded in this section. In the scenario a shorted antenna acts as a backscatter sensor and is standing at a distance d_1 in front of the reader antenna. Two metal sheets are located in the measurement environment. The first sheet stands at a distance $d_2 = 1$ m in front of the reader antenna, and the second one at a distance $d_3 = 2$ m behind the reader antenna. The setup is sketched in Figure 2.7a.

Suppose, the tag antenna has a gain of 4 dBi at an operation frequency of 3 GHz, then according to equation (2.7) its RCS is equal to 0.02 m^2 . If the first metal sheet has a size of $20 \times 20 \text{ cm}^2$, according to (2.5), its RCS is 2.01 m^2 and thus, 100 times larger than the RCS of the sensor tag. After (2.8), the SIR is then -20 dB. This SIR is marked in Figure 2.3.

The reader transmits a radar pulse with a power of 0 dBm via a 13 dBi horn antenna. The reader will subsequently receive the horn mismatch reflection, the metal sheet clutter reflection, the wanted backscatter signal of the tag as well as receiver and ambience noise. These initial Rx powers are depicted in Figure 2.7b:

2.3. Challenges of Chipless Sensor Systems

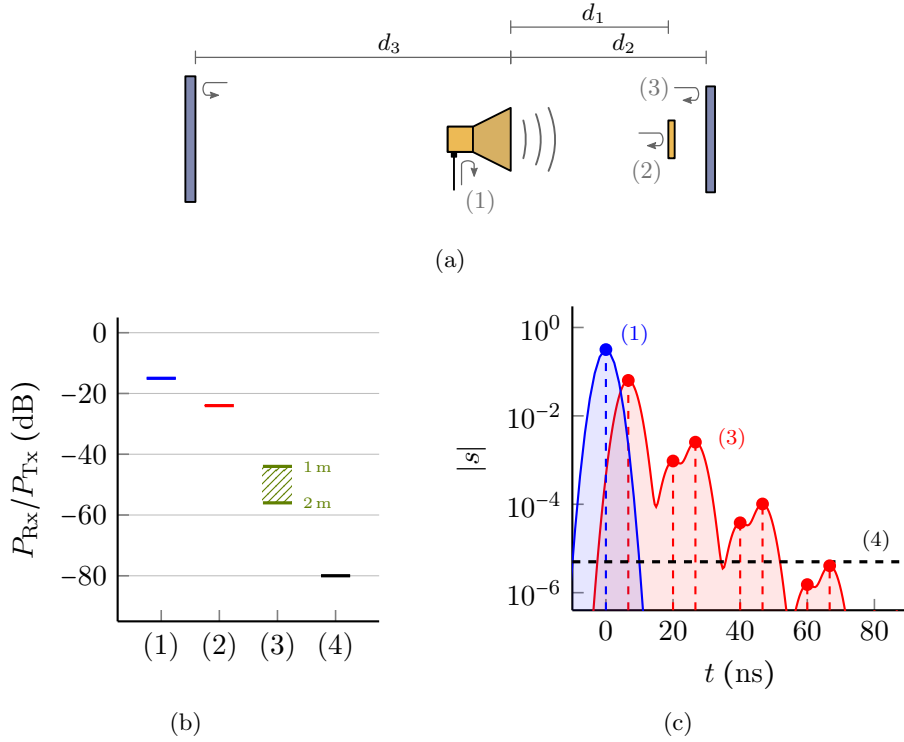


Figure 2.7.: Setup and Rx signals of the scenario Example of Section 2.3.3 with mismatch (1), tag signal (2), clutter (3) and noise (4): a) setup; b) comparison of Rx power levels; c) time response of the Rx signal.

The reflected antenna mismatch level is usually around -10 to -20 dB; the noise level scales proportional to the Rx bandwidth and is typically around -80 dBm or less. After (2.4), the Rx backscatter power of the tag will be at a level of -44 dBm for a distance of $d_1 = 1$ m, and the clutter power is at -24 dBm. The tag power will drop by 12 dB when doubling the tag-to-reader distance.

In contrast to the mentioned low SIR, the SNR will be comparatively high at $+36$ dB at 1 m distance and would decrease down to 0 dB if the tag was moved to 8 m distance.

The clutter reflection of the first metal sheet is not only received by the reader antenna, but it propagates towards the second metal sheet where it is reflected again. This secondary reflection leads to repeated re-reflections of the pulse between the two sheets. The reader will receive each of these reflections when they pass its Rx antenna. Hence, the reader will receive multiple clutter echoes of the Tx pulse². The echo amplitudes will decay exponentially over time, as each reflection scatters the incident wave in space. Figure 2.7c shows the envelope of the Rx signal $s(t)$ in Time Domain (TD). Here, the second sheet has a size of 30×30 cm² and the reader antenna

²For the sake of simplicity, the reflection of the pulse on the structure of the reader antenna is neglected here.

2. Fundamentals of Chipless Wireless Sensors

has a gain of -7 dBi in reverse direction towards the second sheet. The figure shows the clutter echoes that can be considered as a series of dirac pulses for an infinitely short pulse. As the bandwidth of the system will be limited in practice, the finite pulse length will lead to a broadening of the diracs and a continuous time-spread of the clutter superposition. This broadening is shown for a Gaussian Tx pulse with a length of 3 ns, equivalent to a bandwidth of 333 MHz.

The example underlines that even in a simple environment with comparatively small environment objects, a direct tag detection is impossible as the SIR is low and the tag signal will drown in the clutter. Hence, this thesis investigates countermeasures and reading approaches to detect the wanted sensor signal against the clutter. The investigated methods are introduced in the following subsection 2.4 and discussed in the main chapters.

2.4. Clutter Countermeasures

Chipless wireless sensors are using backscatter principles. Their wireless operation has immanent challenges as discussed in the previous Section 2.3. From these challenges, the occurrence of radar clutter is probably the largest hurdle concerning the wireless communication: The sensor environment generates unwanted backscatter signals that superimpose with the wanted tag response. This superposition is especially critical since the power of the clutter is usually significantly stronger than the tag signal and since the clutter signals are usually time-variant. This variance has to be expected in any non-static practical application, where any movement, vibration or rotation of objects in the sensor's environment and of the reader antenna will cause the clutter's time dependency.

In order to operate chipless systems in practical environments in spite of the occurrence of clutter, a number of different countermeasures can be taken. These countermeasures aim at suppressing the clutter impact, and hence at increasing the SIR in order to establish proper tag reading. In the following a number of countermeasures are introduced, which are categorized into two groups.

The **first group** consists of countermeasures with a high suitability for practical application. Each of these measures is analyzed and treated in detail throughout the thesis. The first three of the following suitable measures are put forward into three chipless concepts targeting operation in time-variant environments. The measures are:

- **Polarization separation** of wanted tag response and unwanted clutter signals as discussed in the dual-polarization concept of Section 4.1,
- **Frequency Domain (FD) separation** of tag and clutter signals as discussed in the harmonic radar concept of Section 4.2,
- the **Time Domain (TD) separation** of clutter and tag signals as used in the high- Q resonator concept of Section 4.3, as well as,

- the application of **channel estimation** means as introduced in Chapter 5 in order to dynamically estimate and suppress clutter interferences.

The **second group** consists of measures which are rated as only weakly suitable for chipless operation in high-temperature environments. This rating is reasoned for each measure below. The weakly suitable countermeasures include: clutter reference measurements, a highly directive reader antenna and Ultra Wideband (UWB) pulse operation.

- **Clutter reference measurements:** the clutter signal of a specific setup can be measured by installing the reader antenna and measuring the room’s backscatter signal when the sensor tag is not installed. This Rx signal is then called reference and it is subsequently subtracted from each measurement of the setup *with* the sensor tag. Hence, the method determines the difference between the empty room and the room with the tag, which cancels the largest part of the clutter. This way, the method also measures and cancels the antenna mismatch. The reference measurement approach usually achieves good results, but it is strictly limited to static setups. That means, that each movement of environmental objects in the room, or of the reader antenna, requires re-measurement of the clutter reference. This, in turn, requires the manual effort of de-installation and re-installation of the sensor tag for each re-measurement. This effort is even necessary for slightest movements in the sub- $\frac{\lambda}{10}$ range (i.e. usually sub-cm range) as even small movements lead to a phase difference between the actual clutter and the reference clutter signal. As a consequence, the method is not suitable for time-variant scenarios.

The method of clutter reference measurements is used in several publications on chipless systems, such as [PK09; VPT11; Ven+14a].

- **High directivity reader:** In order to suppress unwanted clutter signals, it appears thinkable to use antennas with very high gain, respectively, very directive radiation pattern. This way a narrow beam could be used to ‘illuminate’ only the tag by a small spot and blend the environment out.

Yet, the very directive reader approach inherits three significant drawbacks, which reason its low suitability: First, as directivity increases and spot size decreases, the placement of the sensor tag is only allowed within the spot, i.e., it becomes more restricted. This contradicts a dynamic scenario, where the tag is allowed to move, as it might be connected to a moving component in a manufacturing process. To countersteer this placement constraint, a scanning beam is thinkable, that searches for the tag. However, this scanning beam requires a tremendous design effort on the reader side, which contradicts an inexpensive realization. Second, very high gain antennas are inevitably large in size. This size requirement is impractical for many application scenarios.

Third, for many application scenarios, the directive reader approach will not lead to sufficiently high SIRs as the antenna focussing is limited by near-field

2. Fundamentals of Chipless Wireless Sensors

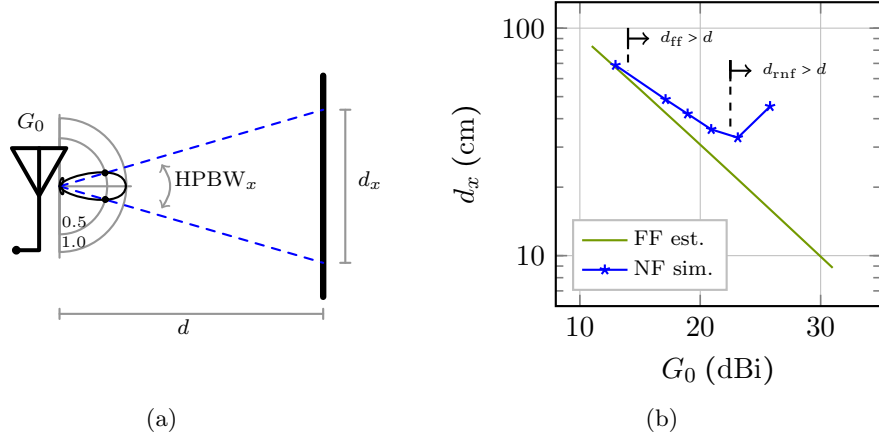


Figure 2.8.: Focus size d_x versus antenna gain of an aperture antenna when using the far-field calculation from the HPBW (FF est.) and of simulated horn antennas including the antenna near field (NF sim.). Parameters: distance $d = 1$ m, operating frequency $f = 3$ GHz, aperture efficiency $\epsilon_{ap} = 0.5$. d_{ff} indicates the far-field border, d_{rnf} the border of the radiating near field.

effects. The gain G_0 of an aperture antenna with rectangular aperture size $W_x \times W_y$ and aperture efficiency ϵ_{ap} increases with increasing size according to $G_0 = 4\pi\epsilon_{ap}\frac{W_x W_y}{\lambda^2}$. The Half Power Beam Width (HPBW) of this antenna will decrease with increasing antenna size. The HPBW scales to $\text{HPBW}_x \propto \frac{\lambda}{W_x}$ in x -orientation and is written accordingly for the y -direction. The directive antenna will generate a field concentration on a surface facing the antenna in a distance d , as sketched in Figure 2.8a. The height d_x of this 3dB spot is calculated as $d_x = 2d \tan(\text{HPBW}_x/2)$ when far-field propagation is assumed. The far-field spot size is plotted in Figure 2.8b versus antenna gain for a distance of $d = 1$ m and an operation frequency of 3 GHz. In direct comparison, the figure also shows the spot size d_x of a horn antenna with increasing size and gain as obtained from 3D full wave simulation. It becomes obvious that the spot size of the simulated horn coincides with the theoretical far-field spot size only for small gains below 15 dBi. For larger directivities, the focal area of the horn hardly increases. This limitation occurs when the focal area of the surface moves into the antenna near-field. Inside the reactive near-field region, the field focus is lost.

If we now consider the scenario example of Section 2.3.3, the spot size limitation becomes comparable to the interference power. For simplification, it is assumed that the spot size can be seen equivalent to the size of a plain metal object in terms of clutter power. From Figure 2.3, it is then concluded that a spot size of less than $6 \text{ cm} \times 6 \text{ cm}$ would be required for SIRs larger than 1. Yet,

Figure 2.8b indicates, that the spot will not focus smaller than 30 cm, which is 5 times larger than required. Consequently, the directive reader approach will only lead to SIRs smaller than 1 in this example.

- **UWB pulse operation:** the rule of constant time-bandwidth products $B_p T_p = c_p$ relates the time period T_p of a pulse to its bandwidth B_p and to a pulse shape-dependent constant c_p . According to this rule, the generation of temporal short radar pulses is possible by spending a large system bandwidth. A short radar pulse allows for spatial separation of backscatter objects in radial direction, as long as the backscatter pulses do not overlap, i.e., as long as the time delay Δt between two pulses is larger than their pulse duration, $\Delta t > T_p$. Hence, the radial spatial resolution Δz is derived as

$$\Delta z = \frac{1}{2} c_0 T_p = \frac{1}{2} c_0 \frac{c_p}{B_p}. \quad (2.9)$$

As an example, a bandwidth of 4 GHz will allow for a spatial resolution of 3.75 cm, assuming $c_p = 1$. If the backscatter response of the sensor tag is now as short as the interrogation pulse, a spatial separation of the tag response against the environment clutter is possible, as long as the tag and the objects are radially spaced by at least a few centimeters.

This UWB approach is used in several publications on chipless systems, such as [Ram+11; Gir+12; Sch+14a]. Yet, the approach fails, when the sensor is directly mounted onto a random environmental object, or when other environment objects are located at practically identical radial distance as the tag, as the required bandwidth would then become infinite. For many practical scenarios the UWB approach is consequently judged unsuitable.

3. Dielectric High-Temperature Transducers

The design of an electromagnetic sensor raises inevitably the question of a suitable measuring transducer. Especially, for a chipless tag that operates at high temperatures, the transducer meets high requirements. Here, the transducer is embedded into the RF signal path, and directly modulates properties of the RF signal as described in Section 2. As the goal of this thesis is the design of a temperature sensor, the desired transducer will convert the local temperature of the tag to an electric property.

In an equivalent circuit of a chipless sensing system, the transducer can be regarded as a temperature-sensitive passive impedance. Principally, the measurand can influence ohmic properties, i.e., the real part, of this impedance or its imaginary part. In the former case, metallic or dielectric temperature-dependent losses can influence the RF signal amplitude. This principle is used in a few chipless amplitude-modulation approaches, as introduced in Sections 2.2 and 1.2.2. In the latter case, inductivities or capacities are influenced by temperature-dependent permeabilities or permittivities. This allows realization of chipless phase or frequency-position modulation approaches, as introduced in Section 2.2.

This thesis focuses on the realization of frequency-position modulation techniques under support of temperature-dependent capacitive transducers. This choice is motivated due to two reasons. (a) Frequency-position modulation is believed to benefit from its propagation loss- and propagation phase-independent signal detection. This stands in contrast to most amplitude and phase modulation techniques (compare Section 2.2). (b) The setup of suitable inductors for radio frequencies in the gigahertz range is usually more complicated than the setup of capacities. Increasing ohmic losses and parasitic effects commonly decrease the inductive behaviour with increasing frequency. Additionally, a continuous and reversible temperature-dependency of the permeability is not given by most materials in the high-temperature regime.

As a consequence, dielectrics are the primary basis for all temperature transducers of this thesis and all of these transducers are capacitive. Dielectric material properties, such as the relative permittivity, its temperature-dependency and the dielectric loss are in the focus of this section. A comparison of dielectric properties of a few materials at room temperature is given in Section 3.1. Properties and usage of the ferroelectric BST is introduced in Section 3.1.

The knowledge of dielectric properties of many materials at high temperatures is limited. Especially concerning microwave properties, the dielectric characterization in high temperature ranges requires considerable effort. This topic is addressed in

3. Dielectric High-Temperature Transducers

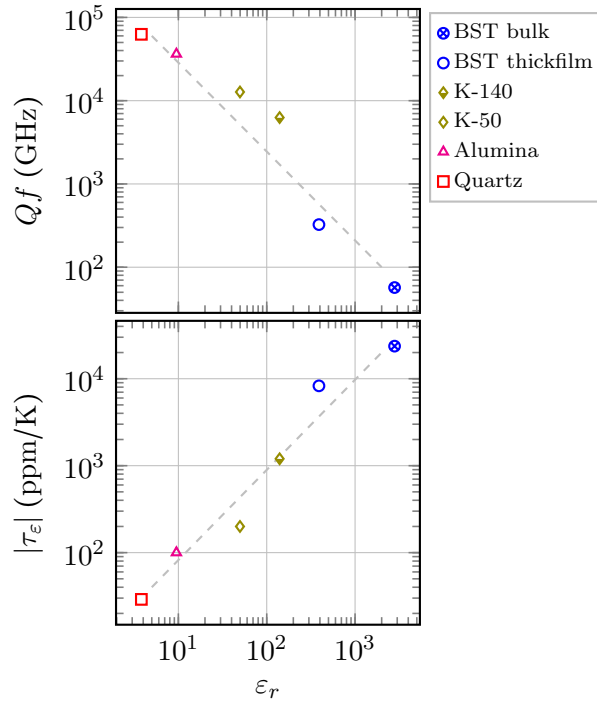


Figure 3.1.: Properties of a few dielectric materials at room temperature; frequency range between 1 GHz and 10 GHz.

Section 3.2. There, a novel resonant high-temperature characterization method for high- Q materials as well as characterization results, are presented.

3.1. Materials and Material Characteristics

In principle, a large variety of dielectric materials is known. For application at high temperature, especially ceramic dielectrics are suitable. [Seb08] presents a noteworthy review of developed ceramics for application at microwave frequencies. It lists more than 2200 different compounds and 36 single crystals, that have been manufactured and characterized.

Relevant material properties are the relative permittivity ϵ_r and the dielectric loss tangent, given as the inverse of the material Q -factor, i.e., $Q_{\text{mat}} = 1/\tan \delta$. The Q factor is often given in the product with the measurement frequency, named Qf . This product accounts for the typical increase of the material loss with frequency and often allows for a better comparison of different materials.

The variation of the permittivity in a certain temperature interval $\Delta\vartheta$ is usually given by the temperature coefficient τ_ϵ

$$\tau_\epsilon = \frac{1}{\epsilon_r} \frac{\Delta\epsilon_r}{\Delta\vartheta}, \quad (3.1)$$

which normalizes the permittivity change to the absolute value of the permittivity. For a chipless sensor, the change of the material permittivity is supposed to result in a shift of the resonance frequency, in order to transduce the measurand to an electric property, that is suitable for wireless reading. The normalized change of the resonance frequency in the given temperature interval

$$\tau_f = \frac{1}{f_0} \frac{\Delta f_0}{\Delta \vartheta}, \quad (3.2)$$

is called temperature coefficient of the resonance. An increasing material temperature coefficient will usually lead to an increasing frequency shift. For a simple *LC* resonator, the relation between material and resonance coefficients can be approximated by $\tau_f \approx -\frac{1}{2}\tau_\epsilon$ for small temperature intervals.

Figure 3.1 shows quality factors and temperature coefficients of a few ceramics at room temperature for microwave frequencies around 1 GHz to 10 GHz. The plot includes pure SiO₂ (Quartz) with a permittivity of 3.8 (properties taken from [Sha+16]); alumina with a permittivity of 9.5 (own measurement); two non-specified ceramic compounds from manufacturer TCI, namely K-50 with a permittivity of 49.8 (own measurement) and K-140 with a permittivity of 140 (properties from [TCI]); as well as a BST thickfilm with $\epsilon_r = 390$ (own measurement) and a BST bulk ceramic with $\epsilon_r = 2800$ (own measurement). The plot indicates the highest Qf of 62×10^3 GHz for the lowest permittivity material, Quartz, and the lowest Qf of 57 GHz for the highest permittivity material, bulk BST. A general trend of increasing dielectric loss with increasing permittivity is concluded. This trend is also stated in [Seb08]. The magnitude of the temperature coefficients of the listed materials range from 29 ppm/K for Quartz, up to 23.7×10^3 ppm/K for bulk BST. A general increase of the permittivities' temperature dependencies is observed with increasing permittivity. It is noted that the sign of the temperature coefficient τ_ϵ is usually positive for low permittivity materials and negative for high permittivity materials [Seb08].

For the design of a chipless temperature sensor, the choice of an adequate transducer dielectric must be oriented on those mentioned properties. It seems that a certain material cannot provide maximum temperature-sensitivity and highest material quality simultaneously. The material choice will likely require a compromise and include given constraints, such as size, operation frequency, desired accuracy or temperature range.

Ferroelectric transducer

The ferroelectric BST is among the materials with highest permittivity and highest temperature coefficient. Its permittivity is tunable by applying an electrostatic field across the material. This tunability has been studied [Tan+03] [Men+11] and applied in number of voltage-tunable RF components, such as varactors, phase shifters and filters [Mau+11].

3. Dielectric High-Temperature Transducers

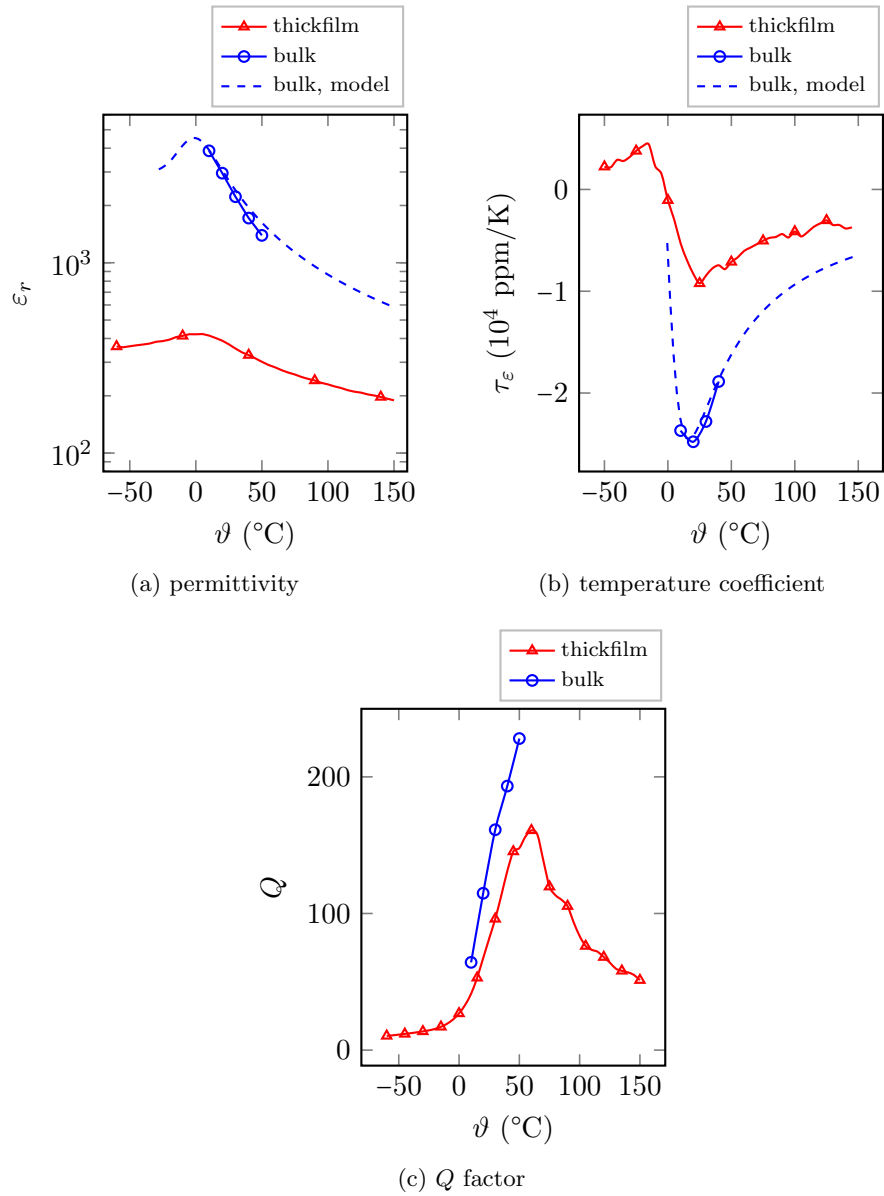


Figure 3.2.: Dielectric properties of BST: a measured thick-film at 5 GHz, a measured bulk ceramic at 1 GHz, and a fitted bulk model from [VZ00].

3.1. Materials and Material Characteristics

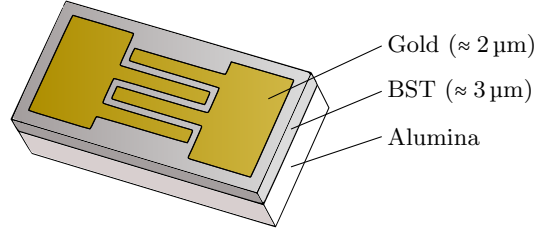


Figure 3.3.: Drawing of an interdigital BST thickfilm varactor.

For temperatures above the Curie temperature, the material is in its paraelectric phase. Here, the permittivity decreases hysteresis-free with increasing temperature. Figure 3.2a shows the measured permittivity of a BST thickfilm over the range of -50°C to 150°C at 5 GHz as well as of a BST bulk ceramic from 10°C to 50°C at 1 GHz. Additionally, modeled material characteristics, as described in [VZ00], are given in relation to the bulk permittivity. Both samples have a Curie temperature of approximately 0°C . It is evident that the bulk ceramic shows a significantly higher permittivity. At 20°C the bulk permittivity is 2800 and seven times higher than of the one of the thickfilm. The normalized slope of the permittivity is plotted in Figure 3.2b as the τ_{ϵ} versus temperature. The maximum slope is observed at 20°C and decreases slightly towards higher temperatures.

The Curie temperature of BST depends on the Barium to Strontium relation in the compound, and increases with increasing Barium content. This allows for a shift of the permittivity curve and temperature sensitivity maximum. It principally enables the design of a maximally sensitive material at a given operation temperature.

Figure 3.2c takes note of the material Q factors. A maximum Q of 160 is reached at 60°C for the thickfilm (at 5 GHz) and 230 for the bulk (at 1 GHz). The Q decreases with further increasing temperature.

Due to its high sensitivity, BST has been chosen as the transducer material in the chipless crosspolar sensor of Section 4.1. Based on the development and material handling experience of tunable BST varactors, the transducer is realized as an interdigital capacitor as drawn in Figure 3.3. The capacity is formed by planar fingers with a length of roughly $200\ \mu\text{m}$, that are electroplated on a $3\ \mu\text{m}$ thick BST film. The setup of an interdigital capacitor on a bulk BST, in comparison to the film, could increase the temperature sensitivity further, expectedly by a factor of up to 2.2.

The manufactured BST thickfilm capacitor shows a component quality factor of 30 at 3 GHz, which includes metallic losses arising from the RF current in the conductor layer. The capacity of the component is $0.5\ \text{pF}$ at room temperature and decreases for increasing temperatures, as expected from the permittivity decrease in Figure 3.2a. The precise course of the capacity of the element versus temperature is plotted in Figure 4.10 in Section 4.1.

3.2. Microwave High-Temperature Material Characterization

As a matter of course, the employment of dielectrics as transducer materials in RF components requires knowledge of their RF properties. This refers especially to the dielectric properties at high temperatures, above 175 °C.

The dielectric microwave characterization of materials at high temperature holds a couple of difficulties. The difficulties include, e.g., the temperature control of the sample, the thermal limits of RF cables and measurement equipment as well as the increasing metallic losses with increasing temperature. Nevertheless, a number of high-temperature dielectric characterization setups have been presented. Among them are broadband, non-resonant transmission/reflection methods, who are using either a) coaxial probes, b) hollow waveguides or c) free-space setups:

- a) [Ger+99] presents a stainless steel open ended coaxial probe for measurements up to 1000 °C and frequencies between 0.3 and 6 GHz. The complex permittivity of a porous alumina composite and of nephelene syenite has been determined. The authors state that their method is limited for $\tan \delta \geq 0.05$ due to reduced accuracy of low loss determination.

[Har+91] presents results measured with a coaxial probe for silicon nitride and a phosphate bonded alumina at temperatures up to 500 °C and frequencies between 2 and 18 GHz. Loss tangents are in the range of 0.2.

- b) [FGL11] presents a high-temperature setup for reflection measurements in a hollow waveguide. Characterizations between 3.3 and 4.9 GHz and temperatures up to 1600 °C are possible. The permittivity of an alumina sample is determined, yet, the material's loss tangent appears uncertain.

[LSE11] presents a transmission-type waveguide setup, that is made of the steel Inconel and operates in the frequency band from 8 to 12.5 GHz and temperatures up to 1000 °C. The ceramic Macor has been characterized and the lowest loss tangent is in the range of 0.005. The authors discuss inaccuracies arising due to thermal expansion of the setup and sample as well as corresponding correction methods.

[HK96] presents a partially heated waveguide for transmission measurements as well as a temperature-compensating calibration approach. Measurement results of a combustion compound for temperatures up to 1000 °C in the frequency range of 7.5 to 12.5 GHz are given. The measured loss tangent is in the range of 0.004. The authors state capability of measuring tangents that are close to 0.001.

- c) [Var+91] presents a free-space setup where the sample is placed inside a furnace and between two spot focusing horn antennas. The furnace is heated up to 850 °C and the operation frequency ranges from 13 to 17.4 GHz. The dielectric constants of quartz and boron nitride are given. The authors comment that

3.2. Microwave High-Temperature Material Characterization

their transmission characterization approach is reliable for loss tangents down to 0.025.

It appears, that these broadband techniques can deliver good results in terms of the determination of the dielectric constant in various ranges. Yet, the accuracy of the loss tangent is limited in all setups, and not suitable for low loss materials with $\tan \delta < 1 \times 10^{-3}$. This result generally agrees with findings of standard broadband characterization methods, which operate at room temperature [She09].

Higher precision of low loss material characterization can be achieved with resonant techniques. Here, only few setups are found that show results at elevated temperatures. Besides its transmission method, the free-space setup of [Var+91] shows the capability of measuring thickness resonances. Here, loss tangents as low as 0.005 have been presented. [Ho88] presents a waveguide cavity, that allows for sample characterization under support of the cavity perturbation method at 35 GHz. The sample is heated up to 1100 °C, while the cavity is evacuated and water-cooled to remain at temperatures below 100 °C in order to keep metal losses as low as possible. The characterization of an alumina sample is presented with loss tangents as low as 3×10^{-4} .

In this section a novel resonant high-temperature characterization method is presented. The method aims at combining the benefits of a free-space setup with the precision of resonant characterization. This way, the necessity for elaborate cooling and vacuum installations is avoided and the heating is performed inside a commercially available furnace. At the same time loss tangents approaching 1×10^{-4} are measured. Furthermore, the method is suitable for various sample sizes, as no precise and temperature-stable sample fitting is necessary.

The characterization is based on resonances inside a cylindrical dielectric, i.e., inside a free Dielectric Resonator (DR). As mentioned before, the term *free* denotes, that the DR is only, or almost only, surrounded by air. This free placement stands in contrast to classical resonant characterization methods, where the sample is surrounded by metal boundaries, either in direct contact (e.g. in the Hakki-Coleman method [HC60]) or at a defined distance (e.g. in the cylindrical cavity resonance method [She09]). Resonant behaviour of free DRs is therefore introduced in Section 3.2.1, while the characterization method as well as characterization results are presented subsequently in Sections 3.2.2 and 3.2.3.

3.2.1. Modes and Radiation Characteristics of Dielectric Resonators

This section studies electromagnetic resonance behaviour inside dielectric objects, usually referred to as free DRs. The term *free* denotes, that the sample is only surrounded by air and not by metallic or magnetic boundaries. Free DRs are used in the material characterization method of Section 3.2 and in the chipless sensor of Section 4.3.1. For both applications a basic understanding of properties of the resonant modes is required.

3. Dielectric High-Temperature Transducers

The following descriptions refer to cylindrical shaped dielectrics, but may be transferred to other shapes as well¹. Section 3.2.1 introduces the occurrence of resonances inside free dielectrics, whereas Section 3.2.1 describes radiation characteristics of DRs when excited with plane waves. The far-field excitation is used to analyze application in backscatter systems as described in Sections 3.2 and 4.3.1.

Modes

A cylindrical DR with permittivity ϵ_r , height h and radius ρ_0 , oriented in z -direction, is sketched in Figure 3.4. Resonant behaviour of the DR is understood when taking a look at wave propagation in a dielectric rod. The rod is formed by longitudinal extension of the height of the DR, i.e., by $h \rightarrow \infty$. The fields of the rod waveguide are subsequently briefly described. In-depth derivations and discussion is found in [KG98].

Every electromagnetic field that fulfills the wave equation, given exemplarily by

$$\frac{1}{\rho} \frac{d}{d\rho} \left(\rho \frac{d}{d\rho} E_z \right) + \frac{1}{\rho^2} \frac{d^2}{d\phi^2} E_z + \frac{d^2}{dz^2} E_z + k^2 E_z = 0 \quad (3.3)$$

for a longitudinal E -field component in cylindrical coordinates, can propagate in the dielectric rod as a wave with wave number $k = \frac{2\pi}{\lambda}$. The wave equation can be solved by separation of variables, i.e., by separation of the dependencies in z -, ρ - and ϕ -direction. The separation leads to harmonic differential equations for z - and ϕ -dependencies and to a Bessel equation in ρ -dependency. Requiring finite field amplitudes and periodicity in ϕ leads to longitudinal fields in the form of

$$E_{z,1} = A_1 J_m(k_{\rho 1} \rho) \sin(m\phi - \phi_0) e^{(-j\beta z)} \quad , \quad \rho < \rho_0 \quad (3.4)$$

inside the dielectric and

$$E_{z,2} = A_2 K_m(k_{\rho 2} \rho) \sin(m\phi - \phi_0) e^{(-j\beta z)} \quad , \quad \rho > \rho_0 \quad (3.5)$$

in the free-space outside the rod. The fields travel with propagation constant β in z -direction. Here, $k_{\rho 1}$ and $k_{\rho 2}$ denote the material- and frequency-dependent radial wave numbers, of which the former is valid inside the rod and the latter outside the rod. A_1 and A_2 are the amplitudes of the E -field. The z -components of the corresponding H -field of this wave are written simultaneously to Equations (3.4) and (3.5). These H -components have amplitudes A_3 and A_4 . Equations (3.4) and (3.5) indicate, that the harmonic differential equations are solved by complex and real-valued oscillations in z and ϕ . The Bessel equation for the ρ -dependency is solved by Bessel functions of the first kind J_m and modified Bessel functions of the second kind K_m , each of order m . Under support of the Maxwell equations, the

¹For example, rectangular shaped dielectrics for application in Dielectric Resonator Antennas (DRAs) are presented in [MI97].

3.2. Microwave High-Temperature Material Characterization

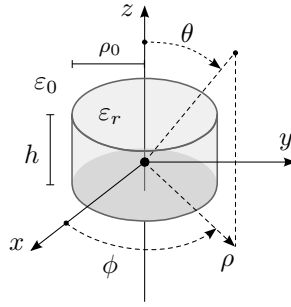


Figure 3.4.: A free Dielectric Resonator with relative permittivity ϵ_r .

corresponding ϕ - and ρ -components of \vec{E} and \vec{H} are derived from the z -components above. As an example, E_ϕ becomes

$$E_{\phi,1} = \frac{1}{k_{\rho 1}^2} \left(j\beta m \frac{A_1}{\rho} J_m(k_{\rho 1} \rho) + j\omega \mu_0 k_{\rho 1} A_3 J'_m(k_{\rho 1} \rho) \right) \sin(m\phi) e^{-j\beta z} \quad (3.6)$$

inside the dielectric ($\rho < \rho_0$) and

$$E_{\phi,2} = \frac{-1}{k_{\rho 2}^2} \left(j\beta m \frac{A_3}{\rho} K_m(k_{\rho 2} \rho) + j\omega \mu_0 k_{\rho 2} A_4 K'_m(k_{\rho 2} \rho) \right) \sin(m\phi) e^{-j\beta z} \quad (3.7)$$

outside of the rod ($\rho > \rho_0$).

The four field amplitudes A_i can only be determined, when the continuity conditions of the tangential field components are fulfilled. These conditions yield four equations, each one for E_z , E_ϕ , H_z and H_ϕ at $\rho = \rho_0$. Searching for non-trivial solutions of these four equations under support of matrix notation leads to the determinant condition

$$F_1(x) F_2(x) - F_3(x) = 0 \quad (3.8)$$

with

$$F_1(x) = \frac{J'_m(x)}{x} + \frac{K'_m(y) J_m(x)}{\epsilon_r y K_m(y)} \quad (3.9)$$

$$F_2(x) = \frac{J'_m(x)}{x} + \frac{K'_m(y) J_m(x)}{y K_m(y)} \quad (3.10)$$

$$F_3(x) = \frac{\beta m}{k_0 \sqrt{\epsilon_r}} J_m(x) \left(\frac{1}{x^2} + \frac{1}{y^2} \right) \quad (3.11)$$

when the material-dependent wave numbers are substituted in $x = k_{\rho 1} \rho_0$ and $y = k_{\rho 2} \rho_0$. For each order m , a number of n solutions of condition (3.8) can be found. Herein, the number of eigenvalues n is limited, when only guided waves are considered. Hence, the dielectric rod waveguide possesses a set of field modes, denoted with indices m and n . For $m = 0$, Transversal Electric (TE) and Transversal Magnetic (TM) waves are propagating in the waveguide, that show no ϕ -variation. For

3. Dielectric High-Temperature Transducers

$m > 0$, hybrid modes (HEM) propagate, with both E - and H -components in transversal and longitudinal directions. It is important to note, that finding the modes of a dielectric waveguide requires numerical efforts, as (3.8) cannot be solved analytically.

Moving from a dielectric waveguide to a dielectric resonator, discontinuities in z -direction are introduced. These discontinuities are given by two additional dielectric-to-air boundaries distanced by the DR height h (see Figure 3.4). An initial waveguide field will be partially reflected two times at each of these boundaries, leading from a travelling wave to a standing wave inside the DR. Hence, one observes resonances. Furthermore, the discontinuities lead to radiation. For lossless dielectric media, a straight rod waveguide will deliver the full amount of propagating power to the end of the line, whereas the open DR eventually radiates 100% of its field energy into free-space.

The field distributions of the resonant DR modes are based on the field distributions of the guided modes. Yet, the additional z -boundaries increase the effort of deriving and describing them significantly:

An accurate mathematical description of the electromagnetic field in a dielectric resonator is considerably more complicated than the field description in a hollow waveguide resonator. [KG98]

This circumstance has brought up a number of different approaches of solving the resonant field problem. Approximate models, such as the Cohn model [Coh68] and the Itoh-Rudokas model [IR76], have been proposed. The Cohn model assumes a perfect magnetic conductor on the DR surface, which replaces the dielectric-to-air boundary. Itoh and Rudokas develop approximations by inserting perfect metallic boundaries at a distance of the DR. These approximate models give a reasonable insight into basic DR modes, yet they are limited in accuracy and/or focus on shielded DRs as used in filters or oscillators. [KG98] presents an *accurate* numerical approach to solve DR modes. It uses the surface integral equation technique, in which a set of electric and magnetic currents on a phantom surface serve as field excitation. The solution requires significant computational efforts, including application of the method of moments. [KGJ84] presents field plots of the five lowest modes, that have been calculated by the integral equation technique.

One main field of application of DRs are DRAs, where the radiating nature plays a major role. In this context, [MB94] presents curve-fitted formulas of resonant frequencies and radiation quality factors of the first basic DR modes. These comprehensive descriptions have been achieved by inclusion of several publications on DRs, including publications on the above mentioned approximate and numerical models.

As this thesis focuses on the radiation characteristics of basic and higher order modes in order to use DRs in backscatter scenarios, RCS-analyses of cylindrical DRs have been performed. The results presented in this chapter have been achieved by plane wave excitation, using the commercial 3D EM solver CST Microwave Studio.

In close similarity to the modes of the dielectric waveguide, the DR modes are classified into transversal TE and TM, and into hybrid modes (HE, EH or HEM). The field variation in azimuth ϕ - and radial ρ - directions are denoted with indices

3.2. Microwave High-Temperature Material Characterization

m and n as described above. Additionally, index $p + \delta$ with $p = 0, 1, 2, \dots$ denotes the number of variations along the z -axis, wherein the symbol δ holds for a "non-full" variation, as the field zeros are found at $z \rightarrow \infty$.

The first/fundamental mode of a DR is usually (depending on the geometry relation $\frac{\rho_0}{h}$) the $\text{TE}_{01\delta}$. Radiation characteristics of this basic and higher order mode are presented in the following section.

Some higher order modes are attributed to whispering gallery field distributions, where the major field concentration is found in a ring along the outer edge of the DR. These modes are often referred to as $\text{WGE}_{mnp+\delta}$ or $\text{WGH}_{mnp+\delta}$ modes. For the former modes, the electric field is dominantly lying in planes transversal to the propagation direction, and in the latter case, the magnetic field is dominantly transversal [KEM96]. In the notation, m still holds for the azimuth variation of the field components and it is usually high, i.e., $m \gg 1$.

Radiation Characteristics

In order to use DRs in chipless backscatter scenarios, important characteristics are the backscattered power, taken as the RCS, the radiation pattern and the resonance bandwidth.

The **radiation quality factor** Q_{rad} of a certain DR mode is defined as the ratio between the stored energy W_{EM} , i.e., the EM energy inside the DR and its near-field, and the amount of radiated energy W_{rad} , i.e. the energy radiated by the DR in one oscillation cycle,

$$Q_{\text{rad}} \stackrel{\text{def.}}{=} 2\pi \frac{W_{\text{EM}}}{W_{\text{rad}}} \quad (3.12)$$

under the assumption, that no other loss mechanism is present. In an equivalent circuit of the resonator², where the DR is described by a series RLC circuit, the radiation quality factor Q_{rad} describes the relation between the radiation resistance R_{rad} and the inductive and capacitive elements L_r and C_r of the resonator

$$Q_{\text{rad}} = \frac{1}{R_{\text{rad}}} \sqrt{\frac{L_r}{C_r}}. \quad (3.13)$$

In a backscatter system, the radiation quality factor of a specific mode describes a lower limit of the resonance bandwidth, that can be observed when measuring the RCS of the DR versus frequency. This limit can be measured if the dielectric losses of the DR tend to zero, i.e., $\tan \delta \rightarrow 0$, as the relation

$$Q_{\text{rad}} = \frac{f_r}{\text{BW}_0} \quad (3.14)$$

between the resonance frequency f_r and the 3 dB-bandwidth BW_0 of the peak.

The **radiation pattern** of a fundamental DR mode shows strong analogy to the pattern of a dipole. The basic modes $\text{TM}_{01\delta}$ and $\text{TE}_{01\delta}$ are represented by

²compare Figure 4.19a

3. Dielectric High-Temperature Transducers

longitudinal-oriented single electric or magnetic dipoles [MB94]. Using the orientation of Figure 3.4, these dipoles are consequently z -oriented and located on the origin of the coordinate system, i.e., on the center point of the DR. If the electric or magnetic dipole is oriented transversal, it represents the hybrid mode $\text{EH}_{11\delta}$ or $\text{HE}_{11\delta}$.

The radiation pattern of a higher order, non-fundamental, mode shows analogy to a multi-pole, i.e., an array-arrangement of dipoles. This array may consist of an even number N_d of either electric or magnetic dipoles in symmetrical arrangement. As the potential number of dipoles and the number of symmetry planes in a cylindrical shape is theoretically unlimited, an infinite number of higher order modes exists.

Although the analogy between dipoles and DR modes holds primarily for their far-fields and associated radiation patterns, distinct similarities are also found in the **field distributions** of their near-fields. Yet, the dipole representation cannot hold for the dielectric-to-air permittivity discontinuities and their induced Bessel-shaped radial amplitude dependencies as indicated in Equations (3.6) and (3.7).

Figure 3.5 compares four different modes of a cylindrical DR. It shows the dipole representation, and the normalized RCS-backscatter pattern in two planes, namely in the transversal xy -plane and in the longitudinal yz -plane, of the $\text{TE}_{01\delta}$, $\text{TE}_{011+\delta}$, $\text{HEM}_{22\delta}$ and $\text{WGE}_{60\delta}$ mode. The $\text{TE}_{01\delta}$ is represented by a single magnetic dipole with its typical omnidirectional pattern and a maximum directivity of $D = 1.5$. The $\text{TE}_{011+\delta}$ is represented by two magnetic dipoles ($N_D = 2$), stacked in z -direction. Its pattern is rotationally symmetric and has four maxima in a longitudinal cutplane. The $\text{HEM}_{22\delta}$ is represented by $N_D = 4$, vertically oriented magnetic dipoles in regular arrangement. The pattern shows four main lobes and four nulls, each spaced in ϕ by 90° . Compared to the single-pole, the directivity of this mode has more than doubled to $D = 3.4$. The $\text{WGE}_{60\delta}$ mode shows six E -field maxima and six E -field minima inside the DR in a regular circular arrangement. It is therefore analog to $N_D = 12$ electric dipoles in vertical orientation. The pattern shows 12, equally strong lobes with 30° spacing and a directivity of $D = 5.1$. Both, the patterns and directivities of the 2-pole, 4-pole and 12-pole modes indicate an element spacing approximately equal to $\lambda/2$ in the analog dipole models.

Figure 3.6 shows the normalized E -field distributions of the modes. As examples, the E_x components of the $\text{TE}_{01\delta}$ and $\text{HEM}_{22\delta}$ modes, and the E_z component of the $\text{WGE}_{60\delta}$ are plotted along the radial y -axis at resonance, for an aspect ratio of $\frac{\rho_0}{h} = 1$. As expected from Equations (3.4) to (3.7), the field distribution of each mode in radial direction is a combination of Bessel functions of the first and second kind. Distinct field maxima inside the dielectric ($y < \rho_0$) and increasing field concentrations towards higher order modes are recognized.

The maximum resonance amplitude values of the E -fields, when excited with a plane wave with amplitude $E_i = 1 \text{ V/m}$ and resonance at $f_r = 3.8 \text{ GHz}$ are given in Figure 3.7. The figure also shows the maximum values of the RCSs of each mode. The $\text{TE}_{01\delta}$ exhibits a maximum amplitude of 6 V/m for $\varepsilon_r = 25$, which nearly doubles when increasing the permittivity to $\varepsilon_r = 50$. The DR radius ρ_0 reduces approximately proportional to $1/\sqrt{(2)}$ when doubling the permittivity under the constraint of con-

3.2. Microwave High-Temperature Material Characterization

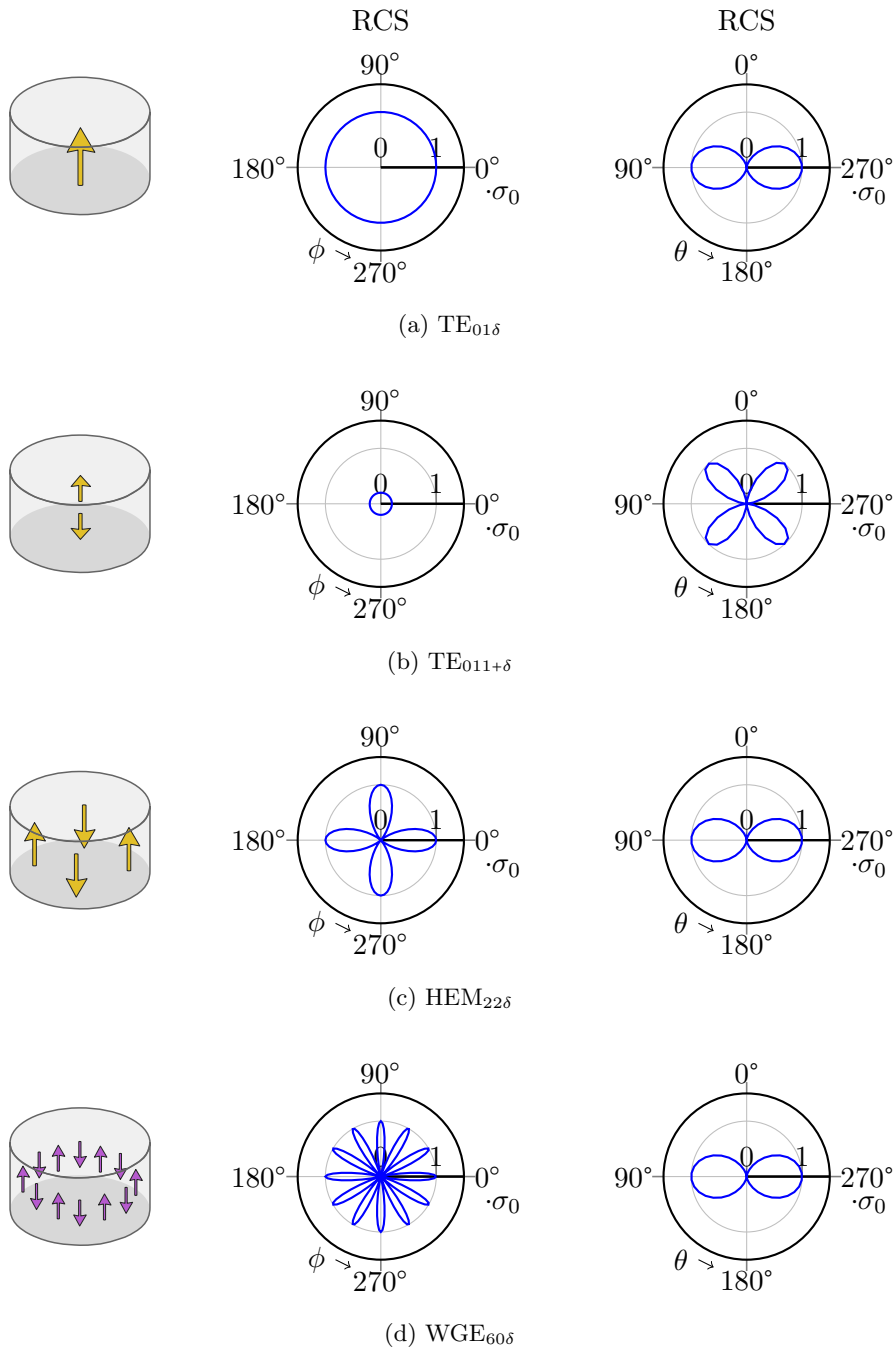


Figure 3.5.: Resonant backscatter radiation pattern of DR modes: (left side) mode representation with magnetic (yellow) and electric (violet) dipoles; (center) pattern versus ϕ for $\theta = 90^\circ$; (right) pattern versus θ for $\phi = 90^\circ$ (aspect ratio $\frac{a_0}{h} = 1$).

3. Dielectric High-Temperature Transducers

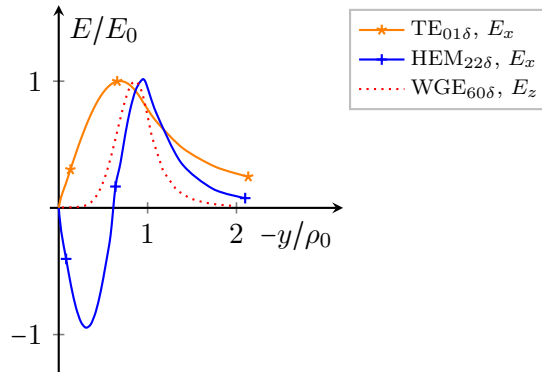


Figure 3.6.: E -field distributions of the DR modes in radial direction along the y -axis.

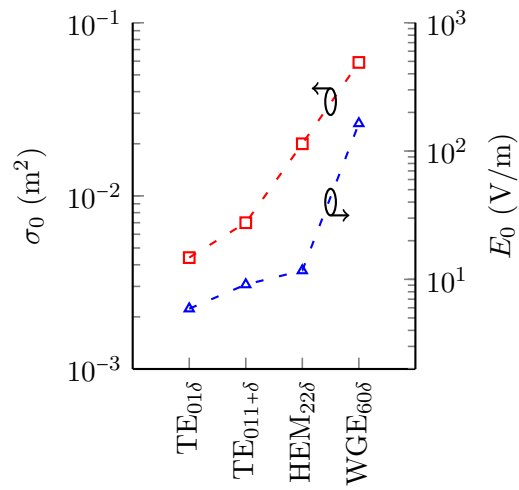


Figure 3.7.: Maximum values of the RCS and of the field strengths (for $\epsilon_r = 25$ and a plane wave excitation with amplitude 1 V/m) of the DR modes.

3.2. Microwave High-Temperature Material Characterization

stant resonance frequency. For the $\text{HEM}_{22\delta}$, the field strength shows two maxima and two minima as the y -line crosses two of the four dipoles. The absolute field maximum quadruples when increasing ε_r from 25 to 50. The field of the $\text{WGE}_{60\delta}$ tends to zero in the inner part of the DR and has a maximum of 160 V/m for $\varepsilon_r = 15$ at $y = 0.85\rho_0$. It becomes obvious that the field strength increases significantly with increasing mode order N_D and with increasing relative permittivity.

When excited with a plane wave with amplitude E_i , the coupling of the DR to free-space and the RCS pattern determine the amount of power accepted by the DR. For a lossless dielectric this accepted power is equal to the re-radiated power of the resonance and can be calculated from the bistatic RCS if the structural reflection of the DR can be neglected³. The radiated power of the resonance mode is then given by the closed surface integral over the power density of the backscatter wave, given by

$$P_{\text{rad}} = \frac{E_i^2}{4\pi Z_0} \int_{\theta} \int_{\phi} \text{RCS}(\theta, \phi) \sin(\theta) d\theta d\phi. \quad (3.15)$$

For a constant resonant frequency, this radiated power increases with the mode order: The HEM mode radiates approximately double, and the WGE radiates approximately four times the power of the fundamental TE mode. This increase is caused by the increasing physical and electrical sizes of the higher order modes. In combination with the increasing directivity, the higher order HEM and WGE have 4.5 and 13.6 times higher RCS amplitudes than the TE.

The distribution of E - and H -fields inside and around the dielectric allows for a determination of the EM field energy stored by a specific mode. The field energy inside a given volume of isotropic media is given by the volume integral

$$W_{\text{EM}} = \frac{1}{2} \int_{\rho} \int_{\phi} \int_z (\varepsilon E^2 + \mu H^2) \rho d\rho d\phi dz, \quad (3.16)$$

which includes both electrical and magnetic energy densities. Figure 3.8a displays the energy of the three introduced modes versus volume size ρ_v . The volume is defined as a cylinder, which is centered to the DR, and given by $\rho \leq \rho_v$ and $z \leq \rho_v \frac{h}{\rho_0}$. Herein, the relation $\frac{\rho_0}{h} = 0.5$ is chosen equal to the DR proportion. Although, the energy densities are locally different, at resonance, the stored energy consists in equal parts of electric and magnetic components (in average), when the chosen volume is large enough. The stored energy increases rapidly with increasing volume size up to $\rho_v = \rho_0$, where the integral volume is equal to the DR volume. Above this point, i.e., when the integral volume stretches into the air, the energy increase slows down significantly. For the $\text{TE}_{01\delta}$, with $\varepsilon_r = 25$, 87% of the total EM energy inside the volume $\rho_v \leq 2\rho_0$ is located inside the DR. For the $\text{HEM}_{22\delta}$ with $\varepsilon_r = 50$ this fraction is already 98%.

Furthermore, it is observed, that the total EM energy of each mode increases with increasing permittivity, although the absolute volume size decreases due to the constraint of constant resonance frequency. The energy increases as well, and even

³compare Section 2.1 for an explanation of structural antenna reflection.

3. Dielectric High-Temperature Transducers

more significantly, with increasing mode order N_D . The WGE mode with $\varepsilon_r = 15$ stores 4.5×10^3 times more energy than the TE with $\varepsilon_r = 50$.

Figure 3.8b takes a look at the radiation quality factors Q_{rad} of the three modes. These Q factors are derived from full-wave simulations and calculated as defined in Equation (3.14). The quality factor increases exponentially with increasing permittivity

$$Q_{\text{rad}} \propto \varepsilon_r^P, \quad (3.17)$$

where the exponent P is mode dependent. The figure shows both the quality factors, as obtained from RCS full-wave simulations of the three discussed modes, as well as interpolation curves for each mode. In double-logarithmic scale these courses appear as straight lines. The line slope allows for a direct determination of the exponent P , which results to $P = 1.3$ for the $\text{TE}_{01\delta}$, to $P = 2.4$ for the $\text{TE}_{011+\delta}$, to $P = 3.0$ for the $\text{HEM}_{22\delta}$ and $P = 5.6$ for the $\text{WGE}_{60\delta}$ mode. These results are supported by [MB94], who states that the exponent P is nearly independent of the aspect ratio of the DR and lies between 1.27 and 2.49 for dipole ($N_D = 1$) and quadrupole ($N_D = 2$) modes. Consequently, one expects even higher exponents for increasing N_D , as found in this work. Table 3.1 summarizes radiation characteristics of the three modes.

Table 3.1.: Comparison of radiation characteristics of DR modes. ($\frac{\rho_0}{h} = 1$)

Mode	$\rho_{0,n}$	$P_{\text{rad},n}$	D	$Q_{\text{rad}}(\varepsilon_r = 25)$
$\text{TE}_{01\delta}$	1.0	1	1.5	27
$\text{HEM}_{22\delta}$	1.8	2	3.4	200
$\text{WGE}_{60\delta}$	2.9	4	5.1	1.6×10^6

The permittivity- and mode-dependency of the radiation- Q is directly related to the size of the DR. As mentioned in Sections 2.2 and 4.3.1, the DR can be modeled as a shorted antenna. As a consequence, similarities between the radiation- Q of a DR and the radiation- Q of an antenna appear likely. The Chu-Harrington limit relates the lowest achievable radiation- Q of an antenna to its size, precisely, to the radius r_c of the smallest possible sphere that encloses this antenna [Chu48] [Har60]. This limit is derived by expressing the antenna's radiation by a spherical mode of order n_c , which in turn can be represented by an equivalent circuit of order n_c . The circuit describes a concatenation of LC -elements and the ohmic radiation resistance of the antenna. The quality factor of this resonant circuit is equal to the radiation- Q of the antenna and given by

$$Q_{\text{rad},C} = \frac{(k_0 r_c)^3 (H' H_1 - H H_1') - 2 k_0 r_c H^2}{H} \quad (3.18)$$

where $H = h_{n_c}^{(2)} h_{n_c}^{(2)*}$ and $H_1 = \text{Re} \left\{ h_{n_c}^{(2)*} h_{n_c+1}^{(2)} \right\}$. Herein, the term $h_{n_c}^{(2)}$ expresses the spherical hankel function of the second kind and order n_c [Han81].

Figure 3.8c plots the Chu-Harrington Q -factor for mode orders up to $n_c = 7$ versus the size of the antenna sphere, normalized to the free-space wave length, $k_0 r_c$.

3.2. Microwave High-Temperature Material Characterization

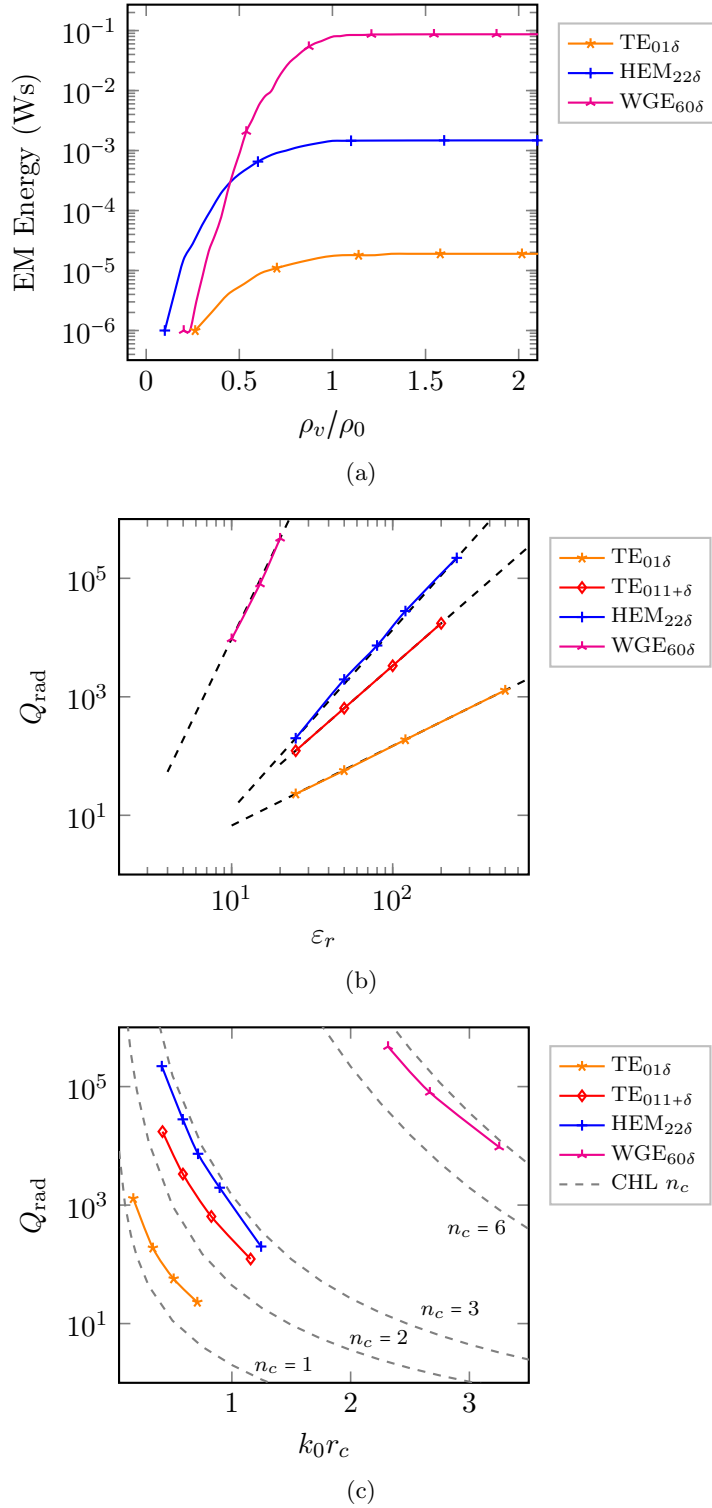


Figure 3.8.: DR mode properties: (a) EM energy versus volume size; (b) radiation quality factor versus DR permittivity; (c) radiation quality factor versus DR size in correlation to the Chu-Harrington limits (CHL) of order n_c .

3. Dielectric High-Temperature Transducers

It becomes obvious that the Q increases rapidly for electrically small antennas. Moreover, it is obvious that, for a fix antenna size, the fundamental order $n_c = 1$ shows the lowest Q , and increasing the order leads to a continuous increase of the radiation quality factor.

Figure 3.8c also shows the radiation- Q of the three discussed DR modes. Here, the size of the DR relates to the size of the antenna sphere as $r_c = \sqrt{\rho_0^2 + (h/2)^2}$. The Q of the DR modes show distinct correlation to the Chu-Harrington limits, even though, small simulation inaccuracies are recognizable: The fundamental $\text{TE}_{01\delta}$ is lower-bound by the fundamental Chu-Harrington order $n_c = 1$, the $\text{TE}_{011+\delta}$ and $\text{HEM}_{22\delta}$ are lower-bound by $n_c = 2$ and the $\text{WGE}_{60\delta}$ by $n_c = 6$. It becomes obvious that for each DR resonance the number of analog dipoles N_D relates to a certain Chu-Harrington order n_c : For fundamental modes $n_c \hat{=} N_D = 1$. For higher order DR modes the dipole arrangement inside the DR is seen in relation to the excitation of the plane wave. The four dipoles of the $\text{HEM}_{22\delta}$ mode consist of two pairs, one pair of dipoles in phase with the excitation and two dipoles with 180° phaseshift. The two pairs relate therefore to $n_c \hat{=} \frac{1}{2}N_D = 2$. This observation holds as well for the $\text{WGE}_{60\delta}$. Here, the 12 electric dipoles are again pairwise in-phase and equally coupled to their neighboring dipoles, which results to $n_c \hat{=} \frac{1}{2}N_D = 6$.

The number of reactive elements in the equivalent circuit of Chu's wave model increases with increasing mode order n_c . This in turn, leads to a higher energy storage in the circuit. In the dipole representation of the DR mode, a physical analogon is seen: An increasing number N_D of dipoles increases as well the capability of storing energy. Each dipole will couple parts of his energy into its neighboring dipoles and vice versa. The energy storage increases and each single dipole radiates less energy into free space. By definition, this increases the radiation quality factor.

Concerning the mode and RCS properties it is noted:

- the field strenghts inside the DR, the stored energy inside the DR and the radiation quality factor increase with permittivity ε_r and mode order.
- the resonant RCS amplitude is generally independent from the radiation- Q , and from the DR permittivity (for a certain mode and constant resonance frequency). The RCS amplitude does depend on the mode, on the excitation field strength, and (slightly) on the aspect ratio ρ/h of the DR.
- according to Equation (2.7), the resonant RCS amplitude is inversely proportional to the square of the resonance frequency, i.e., $|\text{RCS}| \propto f_r^{-2}$.

These mode aspects play an important role when choosing a suitable mode for a chipless backscatter system. Especially, the possibility of generating high resonance quality factors, even for low permittivity dielectrics, is used in Sections 3.2 and 4.3.1.

3.2.2. Resonant High-Temperature Characterization Method

The presented dielectric characterization method excites dielectric resonance modes and evaluates the backscatter radiation of the resonance. This way the method is

3.2. Microwave High-Temperature Material Characterization

linked to chipless sensing principles. In particular, it is strongly related to the high- Q temperature sensing approach of Chapter 4.3.1.

Furthermore, the characterization method is oriented on the specific needs of this sensing approach. Therefore, the method targets the dielectric characterization of low loss materials, and is only weakly suitable for high loss material. The method has been developed for cylindrical shaped ceramic material samples. Yet, it generally allows for characterization of arbitrary shapes as well.

The procedure of the characterization method includes basically four steps: 1) Measurement of the DR sample in a low reflective environment at room temperature, 2) measurement of the sample inside a furnace at elevated temperatures, 3) determination of the mode's properties, i.e., resonance frequency and radiation Q , and finally, 4) calculation of the complex dielectric properties from findings of steps 1) to 3).

The characterization method is based on the assumption that the furnace setup of step 2 does not significantly influence the radiation properties of the DR mode, that is chosen for characterization. This assumption is reasoned by the observation in Section 3.2.1, that the majority of resonance energy is usually concentrated inside or close to the DR. This holds especially for higher order modes and high permittivities, i.e., for modes with high radiation quality factors. The environment in a certain distance of the sample will consequently only slightly influence the resonance energy. Nevertheless, the placement of the sample and the sample holder (in steps 1 and 2) are important aspects, and should be realized with care. This placement as well as further details on the four steps are explained as follows.

Step 1: Measurement of the sample at room temperature

The DR is placed inside an environment that approximates an infinite free space. The sample is afterwards excited with an RF signal that approximates a plane wave. For this purpose, the sample can be placed on a styrofoam holder, whose permittivity is close to 1, and placed on top of microwave absorbers as shown in Figure 3.9a. A horn antenna is placed above the sample and connected to a network analyzer. The network analyzer excites the RF signal and measures the backscatter from the DR. Resonance modes of the DR can be easily identified in the backscatter signal by simple time gating of the complex scattering parameter S_{11} . This method for resonance identification is explained in detail in Section 4.3.1. The absorber and styrofoam holder will provide a fast decaying clutter signal, as well as the avoidance of multipath effects, so that a clean and free resonance behaviour should be observable. Under consideration of the findings in the previous Section 3.2.1, an adequate mode with sufficiently high radiation Q is selected. The resonance frequency f_r and the total quality factor $Q_{0,f}$ of the peak of the chosen mode are measured and noted.

3. Dielectric High-Temperature Transducers

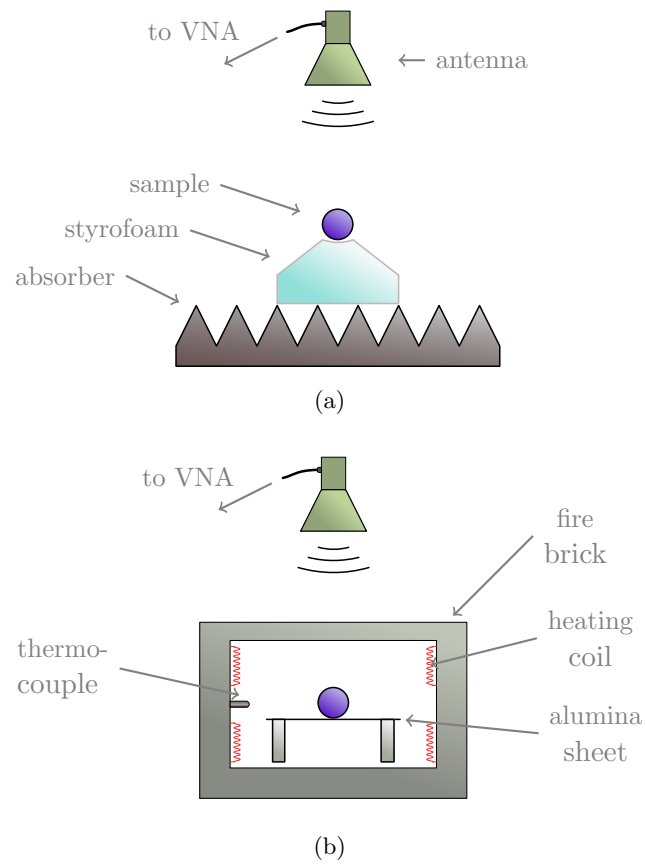


Figure 3.9.: Setup of the dielectric characterization method: a) free setup, b) inside oven.

Step 2: Measurement of the sample at elevated temperature

The sample is placed inside a furnace as shown in Figure 3.9b. Inside the furnace a thin alumina sheet can function as the sample holder. This sheet should have only slight influence on the resonance behaviour of the chosen mode in comparison to setup 1. The interior of the oven should be large enough to surround the sample with adequate air space. The horn antenna is mounted in equal orientation to the sample as in the room temperature setup. Furthermore, the oven frame has to allow for penetration of the EM wave. Metal covers should at least partly be removed.

The chosen resonant mode of step 1 is excited and observed at the desired elevated temperatures. At room temperature, the difference Δf_s of the sample's resonance frequency between in-oven and free setup is noted.

Step 3: Determination of the mode properties

The radiation quality factor Q_{rad} of the chosen mode of the sample as well as the resonant frequency f_r for a certain permittivity can be determined from approximation formulas, such as given in [MB94], from models and accurate solutions, such as mentioned in Section 3.2.1, or from fullwave simulations of the sample. Herein, the determination of these two resonance properties has to cover the permittivity range of the sample as well as the sample's thermal expansion range over the desired temperature range. The radiation properties are consequently modeled in dependence of two parameters

$$f_r = f(\varepsilon_r, \alpha_\vartheta) \tag{3.19}$$

$$Q_{\text{rad}} = f(\varepsilon_r, \alpha_\vartheta) \tag{3.20}$$

if the thermal expansion is described by the expansion factor α_ϑ .

Step 4: Calculation of the dielectric properties

The complex dielectric properties of the sample are calculated in this last step. Therefore, the measured peak resonance positions f_r and the measured peak bandwidths BW_p at all measured temperatures are taken into account.

The time-gating used in the measurements relates to a convolution of the resonance peak with the window function in FD. This convolution has two impacts on the resonance peak: first, it decreases the peak amplitude, as part of the resonance energy is "cutted away". This reduction is usually uncritical for sufficient SNRs. Second, the convolution leads to a deformation of the peak, that usually increases the 3-dB bandwidth. The peak broadening is determined by the relation between the resonance's time decay constant τ and the length of the gate window T_w . Herein, an increasing window length in TD leads to a lesser increase of the peak bandwidth. In order to get an accurate knowledge of the resonance Q of the sample, this peak broadening is corrected, i.e., the true peak quality factor Q_0 is calculated from the

3. Dielectric High-Temperature Transducers

measured peak bandwidth BW_p . For sufficient SNR and SIR, the true peak Q_0 can also directly be calculated from the energy decay τ of the signal envelope in TD⁴.

After determination of the true resonance Q_0 , the dielectric properties at room temperature ϑ_0 are determined under support of the mode characteristics found in step 3. The permittivity

$$\varepsilon_r(\vartheta_0) = f(f_r) \quad , \quad \vartheta = \vartheta_0 \quad (3.21)$$

is derived from the measured resonance position when inserted into Equation (3.19). The material losses at room temperature are derived when the true resonance quality factor Q_0 and the previously found permittivity at room temperature are inserted into (3.20). The material losses are then given by the loss equation

$$Q_{\text{mat},f}(\vartheta_0) = \left(\frac{1}{Q_{0,f}} - \frac{1}{Q_{\text{rad}}(\varepsilon_r, \alpha_\vartheta)} \right)^{-1} \quad , \quad \vartheta = \vartheta_0. \quad (3.22)$$

At room temperature the thermal expansion of the sample is usually zero, and the expansion factor $\alpha_\vartheta = 1$.

For elevated temperatures inside the oven setup, the measured peak properties are taken and correction terms from the free space setup are added. As mentioned above, herein only a slight influence of the environment of step 2 onto the resonance mode is assumed. Therefore, comparatively simple correction is applied.

The permittivity at higher temperatures is determined by correction of the resonance shift Δf_s and insertion into (3.19)

$$\varepsilon_r(\vartheta) = f(f_r + \Delta f_s) \quad , \quad \vartheta > \vartheta_0. \quad (3.23)$$

The oven environment introduces a further loss mechanism that influences the radiation Q . In first line, dielectric losses occur inside the alumina sheet in the direct vicinity of the sample. These losses are summed up in the quality factor of the holder and the environment, named Q_H : It leads to the loss equation

$$Q_{\text{mat}}(\vartheta) = \left(\frac{1}{Q_0} - \frac{1}{Q_{\text{rad}}} - \frac{1}{Q_H} \right)^{-1} \quad , \quad \vartheta > \vartheta_0, \quad (3.24)$$

which allows for determination of the dielectric loss tangent of the sample. The environmental Q is herein calculated by

$$Q_H = \left(\frac{1}{Q_0(\vartheta_0)} - \frac{1}{Q_{\text{mat},f}} - \frac{1}{Q_{\text{rad}}(\varepsilon_r(\vartheta_0))} \right)^{-1} \quad , \quad (3.25)$$

that takes into account the material Q calculated from the free space setup, as well as the measured quality factor inside the oven at room temperature and its corresponding radiation Q . This approach corrects the material Q of the oven setup at room temperature to the same value as the free setup.

⁴compare Figure 5.2a in Section 5.1

3.2. Microwave High-Temperature Material Characterization

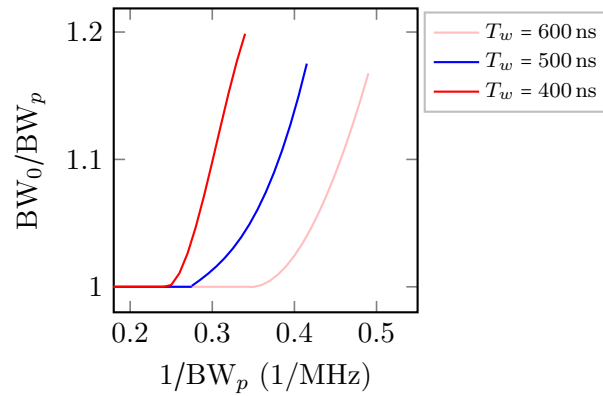


Figure 3.10.: Relation between true peak bandwidth and measured peak bandwidth for the time-gated measurements.

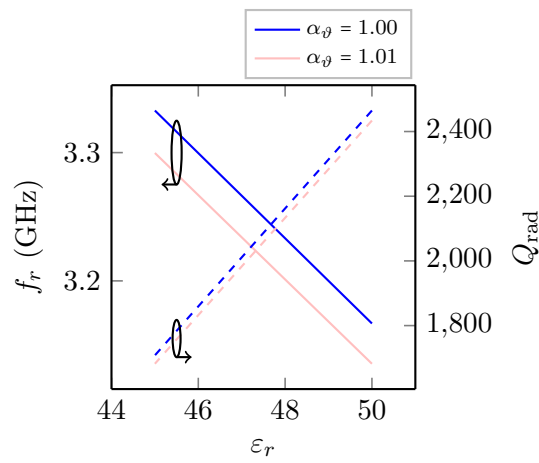


Figure 3.11.: Mode properties of the $HEM_{22\delta}$ used for characterization of the K-50 sample.

3. Dielectric High-Temperature Transducers

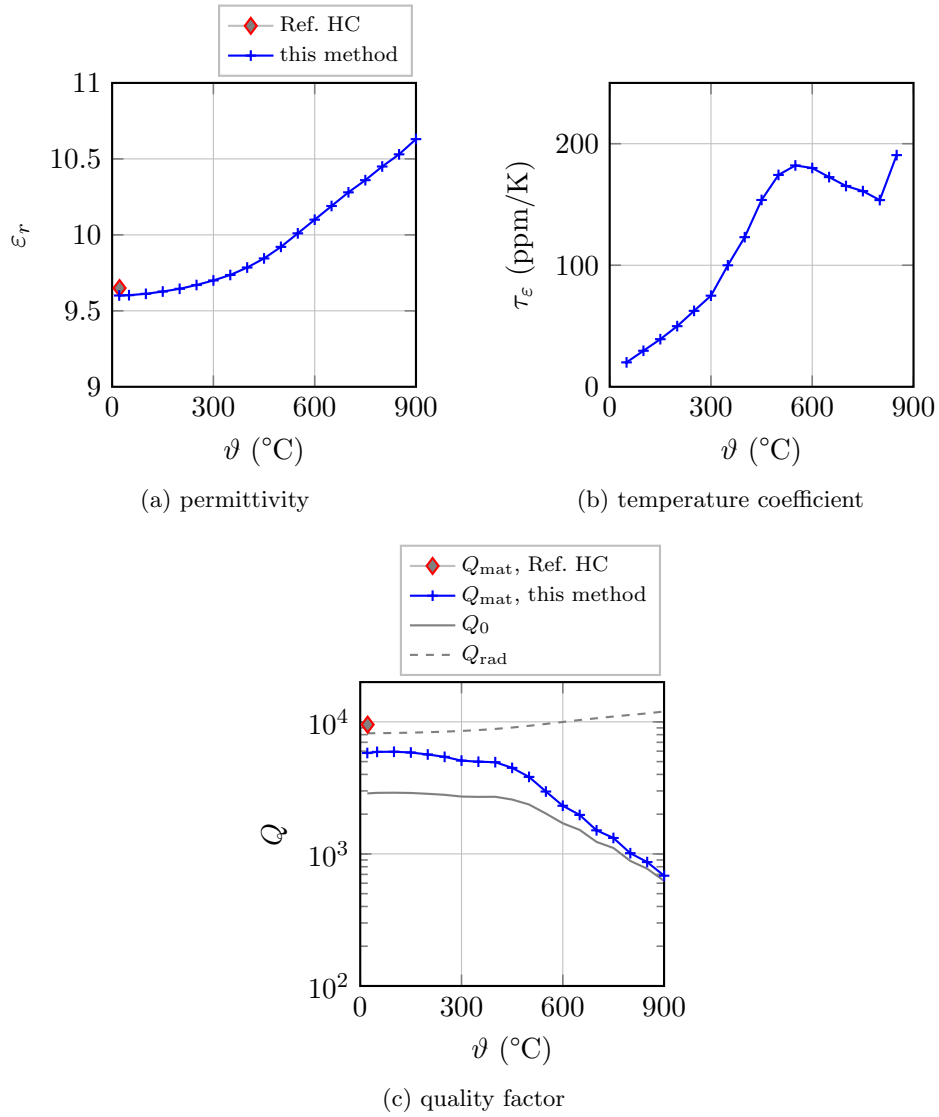


Figure 3.12.: Dielectric material properties of the alumina sample at 6.8 GHz. (Ref. HC: Hakki-Coleman characterization at 3.3 GHz)

3.2. Microwave High-Temperature Material Characterization

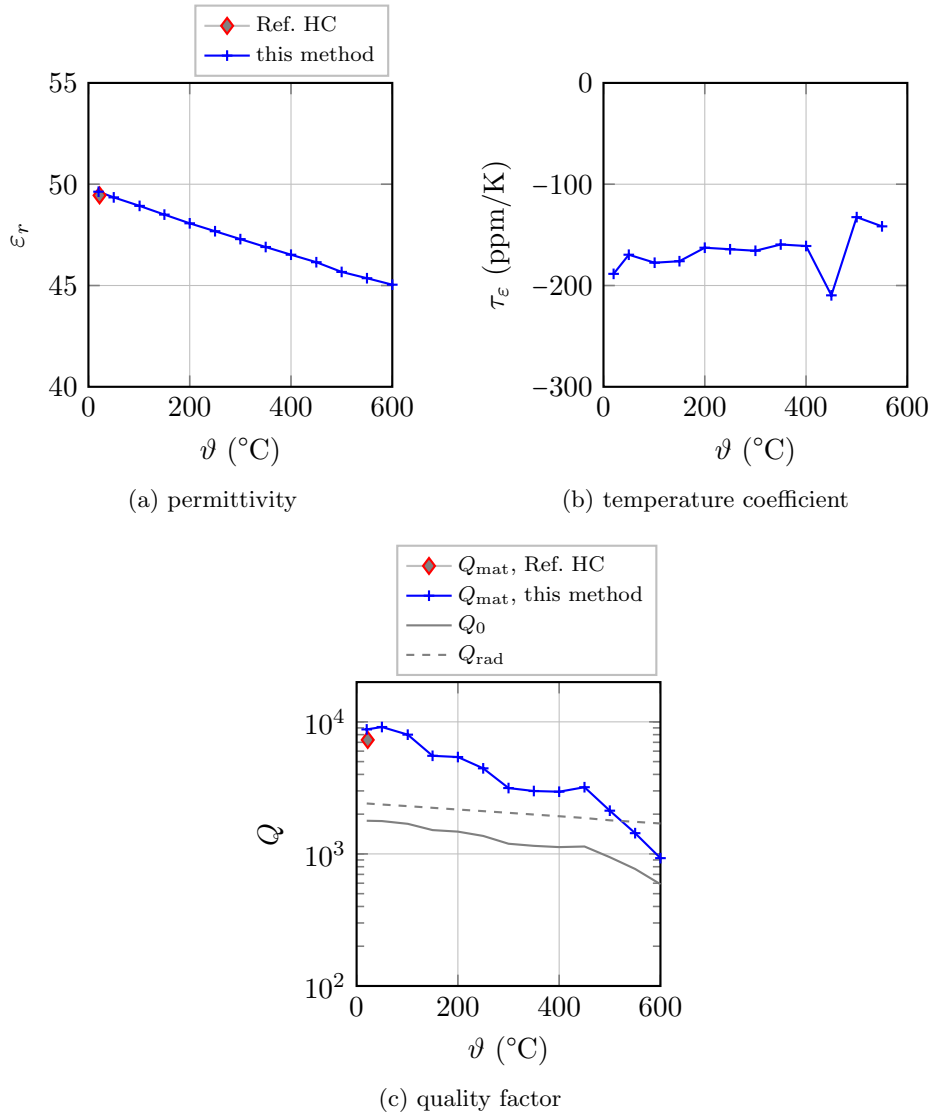


Figure 3.13.: Dielectric material properties of K-50 sample at 3.2 GHz. (Ref. HC: Hakki-Coleman characterization at 2.4 GHz)

3. Dielectric High-Temperature Transducers

3.2.3. Characterization Results

Two ceramic samples have been measured with the previously described free DR high-temperature method. The first sample is a cylinder measuring 41 and 20 mm in diameter and height, made of a 99.5% alumina from manufacturer Ceratec (Kreuztal, Germany). The second sample measures 24 and 13 mm and is made from the ceramic K-50 from manufacturer TCI Ceramics (Pennsylvania, USA) [TCI].

The two samples are measured, according to the description in the previous Section 3.2.2, in free space and inside a furnace. The chosen modes are the whispering gallery mode $WGE_{60\delta}$ for the alumina sample, with resonance around 6.8 GHz at room temperature; and the hybrid mode $HEM_{22\delta}$ with resonance around 3.2 GHz for the K-50 sample. These two modes have been discussed in Section 3.2.1.

The thermal expansion of the samples is included in the characterization in order to achieve a precise determination of the permittivity. The thermal expansion coefficients of the two samples have been taken from the manufacturer's datasheets, and are in the range of 7 ppm/K and 10 ppm/K for the alumina sample and the K-50 sample. The latter sample will consequently grow approximately by 1%, equivalent to $\alpha_{\vartheta} = 1.01$, for a temperature difference of 1000 K.

The mode parameters of the $HEM_{22\delta}$ mode of the K-50 sample are plotted in Figure 3.11 for 0 and 1% thermal expansion. The radiation quality factor of this mode decreases from 2400 to 1800 when reducing the sample permittivity from 50 to 45, and is only weakly influenced by the thermal expansion. The resonance frequency decreases noteworthy by 30 MHz when the sample expands by 1% in the plotted permittivity range.

The measurement results also include a correction of the peak bandwidth in order to counteract inaccuracies resulting from the time-gating. These inaccuracies relate to the resonance time decay, i.e. to the peak bandwidth, and to the length of the window. Figure 3.10 plots the relation between true resonance bandwidth and measured bandwidth for three different window lengths. The results are obtained under usage of a Fast Fourier Transform (FFT) transformation with a Hann windowing. As expected, for a large peak bandwidth, the peak width before and after the gating is equal, whereas increasing peak Q increases the bandwidth difference.

The obtained complex dielectric properties of the two samples are shown in Figure 3.12 for the alumina sample and in Figure 3.13 for the K-50 sample. At room temperature, the results are compared to a reference characterization of the identical samples, which has been conducted with a standard Hakki-Coleman setup. This reference is labeled 'Ref. HC' in the figures and relates to characterization frequencies of 3.3 GHz for the alumina sample and 2.4 GHz for the K-50 sample.

The relative permittivity of the alumina sample increases from 9.60 to 10.63 when heating from 21 to 900 °C. Herein, the measured permittivity at room temperature agrees well with the Hakki-Coleman reference, which gives 9.65, equivalent to a tolerance of only 0.5%.

The permittivity of the K-50 sample has been determined to 49.63 at room temperature with the presented free DR method. This value is compared to 49.45, which

3.2. Microwave High-Temperature Material Characterization

results from the Hakki-Coleman method. It is equivalent to a tolerance of 0.4 %. The sample's permittivity decreases to 45.0 when heating to 600 °C.

The material losses of the two samples are shown in Figures 3.12c and 3.13c. The figures include the measured peak quality factors Q_0 and the modeled radiation quality Q_{rad} . The resulting material quality factor of the alumina sample decreases from 5800 to 680, when heating to 900 °C. The material quality of the K-50 sample has been determined to 8760 at room temperature and decreases to 930 at 600 °C. At 600 °C the loss tangents of the K-50 sample are 2.5 times higher than the ones of alumina.

Discussion

The proposed method provides high-temperature material characterization of low loss materials with a simple setup.

The determination of the relative permittivity has shown agreements with uncertainties of less than 0.5 % at room temperature. For higher temperatures, the characterization of the permittivity of alumina has shown a 10.7 % increase from room temperature to 900 °C. This increase agrees to the findings of [Ho88], who has noted a 12 % increase of alumina's permittivity at 35 GHz in the same temperature range.

Concerning the material losses, the proposed method has shown capability of determining loss tangents as low as 1×10^{-4} . Yet, visible differences between the loss values of the Hakki-Coleman method and the proposed method exist. Three remarks concerning these differences are noted:

- The Hakki-Coleman method refers to different measurement frequencies than the proposed free DR method. For the alumina, the measurement frequencies differ by a factor of more than two. This frequency increase is likely to lead to an increase in loss tangent. Characterization at similar frequencies will decrease the uncertainty.
- The Hakki-Coleman measurement results include a correction of the metal losses of the setup. This correction is based on the derivations in [HC60], but includes uncertainties in relation to the conductivity and surface roughness of the metal.
- The accuracy of the loss tangent calculation of the free DR method is strongly related to the knowledge of the radiation quality factor. Here, possible inaccuracies are found in the simulation setup, that is used to determine the radiation Q .

Finally, concerning elevated temperatures, an impact of the furnace environment including the alumina sheet holder, represents a possible error source. The calculations in step 4 (see Section 3.2.2) can be extended in order to include a temperature- and frequency dependent radiation Q inside the furnace. This will likely increase the accuracy of the loss characterization. Besides, further reference values of the tested

3. Dielectric High-Temperature Transducers

materials, especially at high temperature, will allow for a better judgement of the material Q determination accuracy of the proposed method.

4. Chipless Sensing Concepts

This chapter presents three basic chipless sensor concepts. Each concept is designed to allow for a tag detection in environments with strong time-variant clutter signals. This way, the concepts target application in harsh environments as found, e.g., in industry.

The chipless concepts are subsequently presented and realized with dedicated temperature sensor designs. Briefly introduced, the concepts are:

- Polarization separation, where clutter and tag response are lying on different polarization planes. This approach is investigated in Section 4.1 with a sensor tag, that uses a dual-polarization scheme, i.e., it receives the reader interrogation signal on a linear polarization plane and backscatters on an orthogonal polarization plane.
- Frequency Domain (FD) separation of clutter and tag response is used in the harmonic radar approach of Section 4.2. Here, the sensor tag generates and backscatters the first harmonic of the fundamental interrogation frequency. As the clutter occurs only at the fundamental frequency, clutter and tag are easily separated.
- The Time Domain (TD) separation of clutter and tag signals is used in the high- Q resonator approach in Section 4.3. The interrogation pulse excites a resonator in which energy decays slower than the backscatter energy of clutter reflections. The detection of the tag signal is then possible at late time instants, after the clutter has decayed sufficiently.

The temperature sensing functionality of the three realized tags is proofed with wireless measurements. Furthermore, a performance comparison of the tags in three wireless indoor scenarios is presented in Section 4.4.

4.1. The Dual-Polarization Concept

This Section introduces a chipless temperature sensor that is based on a dual-polarized reading scheme. The reading scheme uses two linear orthogonal polarization planes: one plane to transmit the RF power from the reader towards the tag and the second plane to backscatter a signal from tag to reader. The concept is therefore also referred to as a crosspolar scheme.

As introduced in Section 2.3 a passive backscatter system has to handle the occurrence of clutter signals, which can hinder the detection of the chipless sensor

4. Chipless Sensing Concepts

response. The presented dual-polarization concept aims at separating the backscatter response of the chipless tag from unwanted reflections in order to achieve a clean tag detection. The unwanted reflections include (a) the mismatch reflection of the reader's Tx antenna and (b), more important, clutter reflections from the environment.

For the former case (a) of antenna mismatch reflection the crosspolar system will use two reader antennas in orthogonal orientation¹. The first antenna will be used for Tx and the second for Rx. Due to this effort, antenna mismatch is completely cancelled out as the mismatch reflection will travel towards the generator only and not into the receiver. Yet, the dual antenna system will see antenna coupling from Tx to Rx side, which 'replaces' the mismatch as unwanted signal. Nevertheless, the coupling power will usually be significantly weaker than the mismatch power, especially when the antennas stand in orthogonal orientation.

In many application scenarios it is possible to (at least partially) cancel mismatch and coupling signals by time-gating, when time and spatial resolution are sufficient, or by subtraction of an a-priori characterization, when mismatch or coupling have been measured beforehand. These attempts will often not lead to a perfect cancellation, but, the remaining error signal, due to inaccuracies, will be weaker when the absolute power of the unwanted signal is weaker. The crosspolar approach is here consequently advantageous.

The latter separation of the tag response against clutter, (b), is based on basic principles of EM wave reflections. As already mentioned in the introductory Section 2.1, a plane wave that incides onto an infinite dielectric or metallic boundary is reflected with a material dependent reflection factor. Moreover, for normal incidence, a linear polarized wave will be reflected in the same polarization plane. This holds for both, dielectric and metallic boundaries. Hence, a linear polarized reader interrogation signal will cause clutter signals only in its excitation polarization plane, assuming an normally oriented infinite environment. If the tag now backscatters in the orthogonal plane, a clutter-free detection becomes possible. This observation will of course also hold for moving boundaries, allowing for chipless sensing in time-variant environments as desired.

Nevertheless, depolarization of the clutter can occur at finite sized boundaries and under oblique incidence. Section 4.1.1 analyzes depolarization effects, that can limit the performance of the approach.

A chipless temperature sensor has been designed in order to proof the crosspolar concept and to evaluate its limits in practice. The designed transponder consists of a temperature-dependent notch filter and two patch antennas, which are oriented orthogonally. The setup is presented in Section 4.1.2 and has been published [Kub+12a].

The concept is partly based on [PK09], where it had been introduced for a chipless RFID. Further works on crosspolar chipless transponders are found in [Man+11a],

¹The two antennas can, of course, be integrated into a single dual-polarized antenna with two feeds.

where a displacement sensor is presented and in [VPT13], that presents RFID tags based on strip resonators.

4.1.1. Depolarization effects

This section takes a look at depolarization effects that can generate unwanted cross-polar clutter signals. The crosspolar clutter signals interfere with the wanted crosspolar tag signal. First, depolarization at infinite dielectric boundaries with oblique incidence is considered and second, crosspolar excitation at finite metal boundaries with normal incidence.

The reflection of plane EM waves at infinitely large media boundaries is described by the well known Fresnel equations, which are derived in the literature [Poz05], [Col01]. Here, the Fresnel description is extended to describe crosspolarization at infinite dielectric boundaries. For oblique incidence of a plane EM wave onto a dielectric boundary usually a separation of two cases, namely the p- and the s-case is taken. The p-case describes an incident wave, where the E -field vector lies completely in the cross-plane of incidence. The s-case describes a wave, where the H -vector lies in the cross-plane of incidence. In the s-case case the E -vector is normal to the cross-plane, hence cases p and s are orthogonal to each other.

An arbitrary orientated, linearly-polarized, incident wave can be expressed by the summation of two waves in order to derive the polarization of the reflected wave. For this purpose, the orientation of the incident E -field vector \vec{E}_0 is described by angles β and ϕ_e in a cartesian coordinate system with the xy -plane parallel to the boundary as shown in Figure 4.1a. The angle β describes the tilting of \vec{E}_0 in the xy -plane and angle ϕ_e the tilting of its propagation direction towards the dielectric boundary with permittivity ε_r . The vector \vec{E}_0 is subsequently splitted into its p- and s-case components E_{0p} and E_{0s} . The former component is parallel to the y -axis and the latter parallel to the x -axis. The reflected wave with E -field vector \vec{E}_r , is as well a summation of p- and s-vectors

$$\vec{E}_r = E_{rs} \vec{e}_y + E_{rp} \vec{e}_x = \gamma_{m,p} E_{0p} \vec{e}_y + \gamma_{m,s} E_{0s} \vec{e}_x, \quad (4.1)$$

which are each one caused by the p- and s-components of the incident field. The reflected components are calculated with the Fresnel reflection factors $\gamma_{m,p}$ and $\gamma_{m,s}$, which fulfill the condition of a continuous tangential E -field at the dielectric boundary. Following [Col01], they are

$$\gamma_{m,p} = \frac{Z_m \cos(\phi_d) - Z_0 \cos(\phi_e)}{Z_m \cos(\phi_d) + Z_0 \cos(\phi_e)} \quad (4.2)$$

and

$$\gamma_{m,s} = \frac{Z_m \cos(\phi_e) - Z_0 \cos(\phi_d)}{Z_m \cos(\phi_e) + Z_0 \cos(\phi_d)} \quad (4.3)$$

with the transmission angle $\phi_d = \sin^{-1}(\sin(\phi_e) \frac{1}{\sqrt{\varepsilon_r}})$, the vacuum wave impedance of the incident space $Z_0 = \sqrt{\frac{\mu_0}{\varepsilon_0}} \approx 377 \Omega$, and the wave impedance of the dielectric medium $Z_m = \sqrt{\frac{\mu_0}{\varepsilon_0 \varepsilon_r}}$.

4. Chipless Sensing Concepts

In order to describe the depolarization, the reflected E -field \vec{E}_r , which had been summed up of s- and p-components, is decomposed into copolar and crosspolar components with respect to the incident field. The reflected field \vec{E}_r is tilted from the y -axis by angle $\beta' = \tan^{-1}\left(\frac{E_{rs}}{E_{rp}}\right)$. The magnitude of the copolar component E_{rCo} is then

$$E_{rCo} = \cos(\beta' - \beta) E_r \quad (4.4)$$

and the magnitude of the crosspolar component

$$E_{rX} = \sin(\beta' - \beta) E_r. \quad (4.5)$$

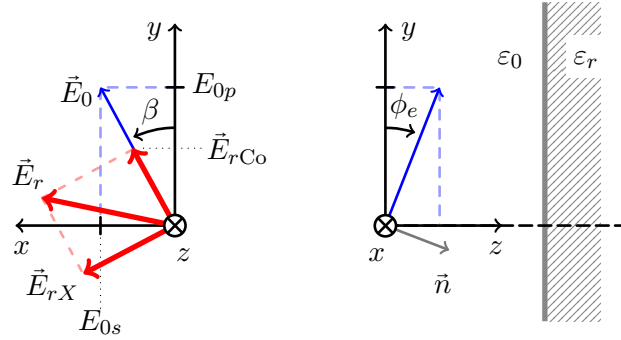
One observes, that the crosspolar component of the reflection is dependent on the orientation of the incident field to the boundary and on the permittivity of the boundary material. In fact, the combination of s- and p-case leads to a tilting of the E -field as the p- and s- components are reflected with different magnitude, according to r_p and r_s in (4.2) and (4.3). As the continuity criterion forces a transmission of the E -field into the dielectric medium, the two-angle dependent incidence leads to a two-angle dependent tangential E -field and hence, to depolarization.

The result of this depolarization is plotted in Figures 4.1b and 4.1c for a lossless dielectric with $\varepsilon_r = 5$. The plots show the magnitude of the crosspolar reflection in relation to the total field strength of the reflected field, i.e., E_{rX}/E_r , and in relation to the total field strength of the incident field, i.e., E_{rX}/E_0 . The crosspolar component tends to zero along the $\beta = 0^\circ$, $\beta = 90^\circ$ and $\phi_e = 0^\circ$ axes. These are the ‘pure’ p-, ‘pure’ s- and normal incidence cases. The crosspolarization increases for oblique β angles between 0° and 90° and towards ‘steep’ incidence $\phi_e \rightarrow 90^\circ$. In this example, the Brewster angle lies at $\phi_e = 65.9^\circ$, which leads to a locally vanishing reflection of the p-component, as the p-component travels completely into the dielectric media. Then, the reflected wave is completely s-polarized, which in turn leads to a strong crosspolar component. The crosspolarization is larger than 90% in the range for ϕ_e close to the Brewster angle and β around 25° as seen in Figure 4.1b. As the Brewster angle also leads to a weaker overall magnitude of E_r , this Brewster effect is not seen in the crosspolarization relative to the incident field, shown in Figure 4.1c.

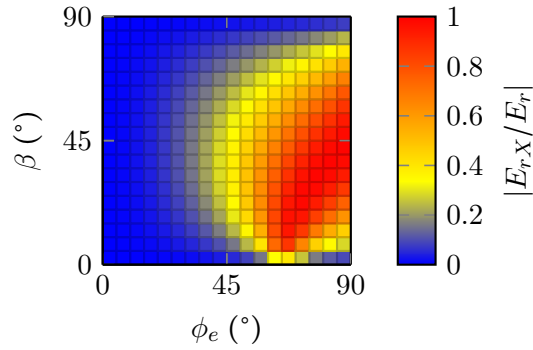
As a conclusion, it is noted that arbitrary oblique incidence of a wave at a dielectric boundary can lead to significant crosspolar backscatter signals. Following Snell’s law of refraction, the crosspolar reflections are travelling away from the surface under the same angle as the angle of incidence ϕ_e . That means, that the largest part of the crosspolar reflection does not directly travel towards the reader. Yet, the crosspolarized wave can propagate against secondary boundaries inside an indoor environment. After secondary reflection it will likely be received by the reader, leading to a crosspolar talkover from transmit to receive side. Furthermore, reflection at finite dielectric objects will lead to a larger scattering in space and consequently, also to a primary reception by the reader antenna.

An evaluation of Equation (4.5) shows that *infinite* conductive boundaries with $Z_m \rightarrow 0$ do not excite crosspolar components. This circumstance is also seen in the p- and s-reflection coefficients in (4.2) and (4.3), that both tend to -1, independent of

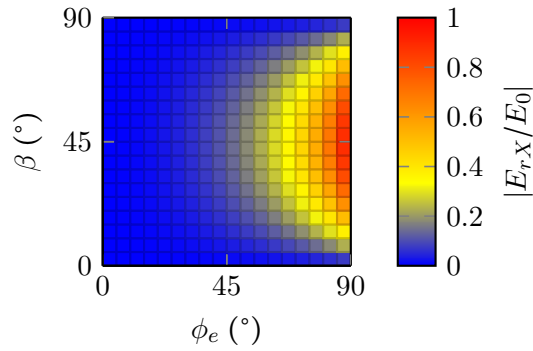
4.1. The Dual-Polarization Concept



(a) Incident and reflected E -field



(b) E_{rX}/E_r



(c) E_{rX}/E_0

Figure 4.1.: Depolarization at dielectric boundary, $\epsilon_r = 5$, $\tan \delta = 0$: (a) incident and reflected E -field, (b) and (c) magnitude of the reflected crosspolar component E_{rX} versus angles of incidence.

4. Chipless Sensing Concepts

ϕ_e . Nevertheless, crosspolar fields can be excited by *finite* conductive materials. In order to analyze the co- and crosspolar backscatter of finite surfaces, the definition of the Radar Cross Section in (2.3) can be extended: The copolar RCS denotes a backscatter wave with copolar E -field magnitude and field intensity $S_r = E_{rCo}^2/Z_0$

$$\text{RCS}_{Co} = 4\pi r_0^2 \frac{E_{rCo}^2}{E_0^2} \quad (4.6)$$

and the crosspolar RCS

$$\text{RCS}_X = 4\pi r_0^2 \frac{E_{rX}^2}{E_0^2} \quad (4.7)$$

refers to the crosspolar field component correspondingly.

Figure 4.2b shows simulation results of the bistatic copolar and crosspolar RCS of a rectangular $20 \times 20 \text{ cm}^2$ metal sheet at 3 GHz. The incident E -field is oriented in z -direction, and the sheet is tilted by angle α as shown in Figure 4.2a. The spherical angles θ and ϕ describe the position of the bistatic observation of the RCSs.

As given by Equation (2.5), the sheet shows a maximum copolar RCS of 2 m^2 ($\hat{=} 3 \text{ dBm}^2$) in the monostatic observation, that is for $\phi = 0^\circ$. The bistatic observation, shows, as expected, a directive beam in broadside direction for the copolar RCS shows a directive beam in broadside direction. This beam is nearly independent on the sheet orientation α . The crosspolar fields are, in contrast, strongly dependent on the sheet orientation and strongly dependent on the bistatic observation point. Figure 4.2b shows, that the crosspolar components tend to zero for parallel orientation of the sheet, i.e., $\alpha = 0^\circ$. But, for tilted sheets, $\alpha > 0^\circ$ and oblique observation angles, the crosspolar components are noticeable. The maximum crosspolar RCS, observed for $\alpha = 30^\circ$ at $\theta = 70^\circ$, is about 24 dB weaker than the broadside monostatic copolar RCS.

The physical explanation of the angle-dependence of the crosspolar RCS is found, when taking a look at the surface currents excited by the incident field. As schematically depicted in Figure 4.2a, the majority of currents flows in parallel orientation to the incident field and excites the copolar backscatter. But, at the sheet corners and edges, the currents are distorted due to the material discontinuity. The currents close to the edge will at least partly orient to the edge and hence, excite components in crosspolar orientation for $\alpha \neq 0$ and $\alpha \neq 90^\circ$. The radiation pattern of the crosspolar components is consequently not a beam-pattern of a homogeneously excited radiating aperture, but that of distributed radiating edges, which are spaced by the sheet size and oriented by the sheet shape. The radiating edges consequently create pattern-nulls and local maxima. This way, the crosspolar radiation strength is highly dependent on the shape, orientation and size of the object as well as on the bistatic observation point. Even in a monostatic observation, the power relation between the co- and crosspolar RCS can be lower than 1, e.g., for a very thin strip oriented with $\alpha > 45^\circ$ to the incident field, where the edge currents are dominant.

Nevertheless, the crosspolar chipless approach will often lead to a significant reduction of clutter interference as chipless systems usually operate monostatic and environmental objects are often large and oriented close to normal incidence. Crosspolar

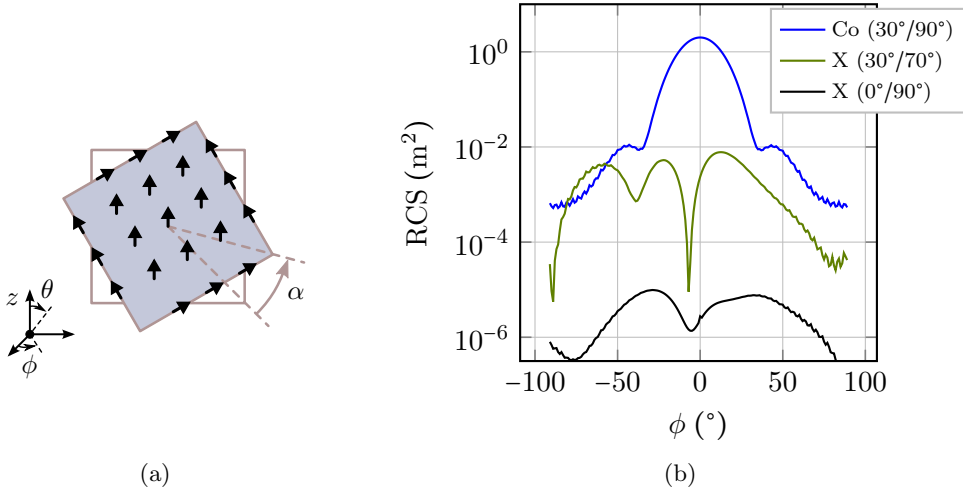


Figure 4.2.: Depolarization at a $20 \times 20 \text{ cm}^2$ metal sheet: (a) schematic depiction of surface currents, (b) simulated copolar (Co) and crosspolar (X) Radar Cross Section (RCS) for (α/θ) cut planes at 3 GHz.

rejection levels of 20 to 40 dB can be expected in primary reflections for many environmental objects.

In this context, the simple chipless scenario of Section 2.3.3 is regarded for comparison. In the example an SIR of -20 dB between transponder and copolar clutter backscatter power is seen. Suppose that in this example, the sheet would dynamically rotate in angles up to $\alpha = 30^\circ$, then according to the result of Figure 4.2b, the usage of a crosspolar reading scheme would reduce the monostatic clutter by at least 24 dB and the SIR became at least +4 dB.

As a last step, the time-dependence of the crosspolar clutter rejection in relation to multiple secondary reflections is considered. Figure 4.3 shows exemplarily the measured clutter signal of an indoor lab room versus time. The baseband time signal is obtained from the Inverse Fast Fourier Transform (IFFT) of a 2 GHz to 4 GHz measurement with two horn antennas. Here, both the copolar and crosspolar reflections have been measured and the relation between the received copolar power P_{Co} and the received crosspolar power P_{X} is plotted. The Rx signals show a strong stochastic random-like behaviour with strong spikes, yet, the general trend can be seen in a moving average. It is visible that in the first time instants the crosspolar Rx power is significantly smaller than the copolar. The initial reflections from the environment are suppressed by more than 20 dB. After 20 ns, secondary echoes arrive and the crosspolar rejection generally decreases. The measurement underlines the effect of clutter-depolarization by multiple reflections at dielectric and metallic objects. A high suitability of the dual-polarization approach for chipless tags with a short response signal is consequently concluded. A short tag signal can profit from the primary crosspolar clutter rejection.

4. Chipless Sensing Concepts

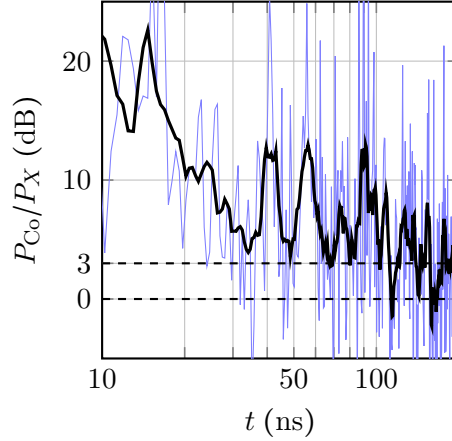


Figure 4.3.: Measurement of clutter of an indoor room: copolar to crosspolar component.

4.1.2. Crosspolar Sensor Tag

The developed chipless temperature sensor system uses a dual-polarized reading scheme with two polarization planes as shown in Figure 4.4. Due to the orthogonal orientation of these two planes the tag is also denoted as the crosspolar sensor tag. It has been presented in [Kub+12a].

The sensor tag consists mainly of three elements, that are integrated on a single planar Printed Circuit Board (PCB) substrate. The three elements are: an Rx antenna, that receives the reader signal on the first linear polarization plane, a temperature-dependent notch filter, that encodes the measurand, and a Tx/backscatter antenna, that backscatters the tag signal towards the reader on the second polarization plane. The reader receives and evaluates the backscatter signal. The measured temperature relates directly to the resonance frequency of the notch filter.

The tag operates in a 200 MHz transmission band at 3 GHz. The common substrate is a Rogers RT/duroid 5880 with 3.2 mm thickness. The three tag elements are designed in microstrip technology with a line impedance of $Z_w = 100 \Omega$, and are introduced in the following.

The Tx and Rx antennas are supposed to cover the transmission band in order to allow feeding of the filter and backscattering of the filter signature. In order to serve the crosspolar scheme, the antennas are meant to have a strict linear polarized radiation pattern (i.e., a high axial ratio) and low crosstalk. Furthermore, a broadside radiation pattern is desired to achieve a high transmission power and to enable mounting of the tag on a metal surface as expected in industrial application scenarios. In order to fulfill these requirements patch antennas have been chosen, which are line-fed from the microstrip. The two patches are placed in orthogonal orientation, at a distance of 7 cm from each other, as shown in Figure 4.5a. Each patch measures 31 mm \times 37.5 mm and is fed with an inset of 7.9 mm in order to match

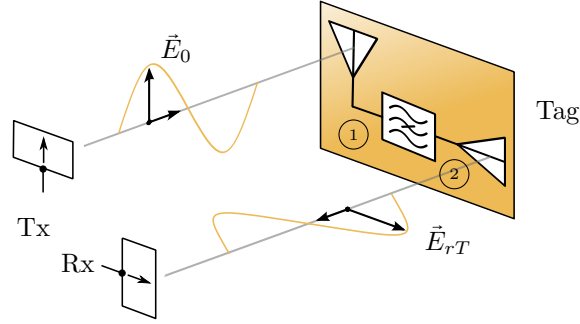


Figure 4.4.: Schematic of the dual-polarized sensor principle with an incident electric field vector \vec{E}_0 and the backscatter field vector \vec{E}_{rT} .

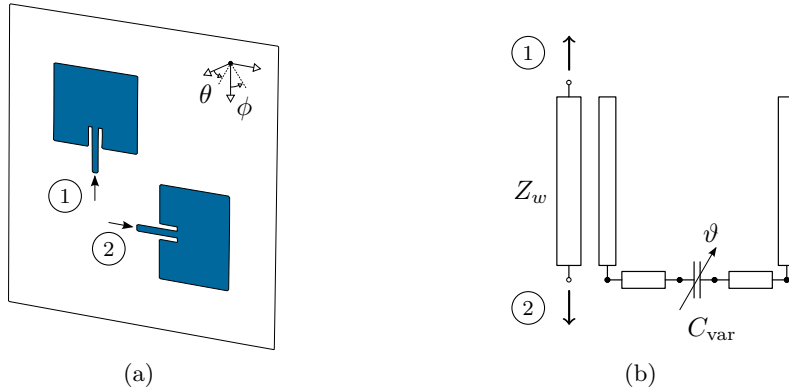


Figure 4.5.: Components of the tag: (a) setup of the two patch antennas, (b) schematic drawing of the notch filter; © 2012 IEEE, [Kub+12a] refers.

to the line impedance of 100Ω . Figure 4.6 shows simulation results of the two patch antennas. The simulated antenna matching is better than 4.6 dB in the range from 2.9 to 3.1 GHz, with an inter-patch crosstalk below -32 dB (see Figure 4.6a). The maximum antenna directivity is 7.4 dBi in broadside direction and the axial ratio, defined as the relation between co- and crosspolar field components in the far-field, exceeds 15 dB for azimuth observation angles $\theta < \pm 50^\circ$ (see Figure 4.6b).

The temperature-dependent notch filter is designed as a coupled line filter. A resonating open-ended line segment, with an electrical length of $\lambda/2$, is partially coupled to the microstrip that connects the two patch antennas as shown in Figure 4.5b. A BST varactor is inserted in the center of the transmission line resonator. The varactor consists of an interdigital capacity on a thick-film BST substrate with temperature-dependent permittivity. Details on the temperature-dependence of BST and on the varactor setup are found in Section 3. As the capacity is placed in the current maximum at the center of the line, it detunes the resonance frequency in dependence of temperature. This detuning is seen in the notch position as shown in Figure 4.7. A capacity reduction from 0.50 pF to 0.35 pF leads to a 180 MHz shift

4. Chipless Sensing Concepts

of the resonance frequency from 2.90 GHz to 3.08 GHz. The notch depth remains approximately constant at -8.5 dB.

Figure 4.7 shows as well results from a wireless simulation of the whole sensor tag. The wireless transmission from two orthogonally oriented reader antennas has been calculated by a full wave simulation. This simulation is setup with a distance of 25 cm between reader and tag. It shows the bandpass characteristic of the patch antennas with a maximum transmission level of -29 dB around 3 GHz. Inside the patch antenna band, the desired filter notches are recognized inside the transmission spectrum. The wireless notch positions coincide well with the notches of the 'standalone' notch filter. The 'standalone' notch positions differ by less than 3.4 MHz from the 'wireless' tag notch positions. These slight offsets are most likely caused by impedance matching offsets between filter and patch antennas: Towards the edges of the antennas' Tx band, i.e., $f \rightarrow 2.9$ GHz and $f \rightarrow 3.1$ GHz, the patch impedances drift slightly away from 100Ω as seen in the matching of Figure 4.6a. Nevertheless, the shift is uncritical for the wireless operation.

When operating the crosspolar tag in the far-field of the reader antennas, the received power in the reader P_{RX} can be derived from a two-way link budget consideration. The power P_{TX} that is transmitted by the reader with an antenna of gain G_R , is partly received by the tag with patch antenna gain G_T . The power that is backscattered towards the reader on the orthogonal plane, is reduced by the notch filter loss a_f . The Rx power is hence written as

$$P_{RX} = P_{TX} + 2G_R - 2a_{fs} + 2G_T - a_f \quad (4.8)$$

in logarithmic scale, when the two free-space path losses are given by

$$a_{fs} = 20 \log_{10}(4\pi d f / c_0) \quad (4.9)$$

at the operation frequency f and the gains of the transmitting and receiving antennas of the reader and tag are assumed identical.

4.1.3. Sensor Simulations and Measurements

The crosspolar temperature tag has been fabricated in a standard PCB process. The BST varactor has been glued onto the resonator with conductive paste. A photo of the 12×12 cm² tag assembly is shown in Figure 4.8a.

The chipless tag has been tested and verified in wireless indoor measurements. Figure 4.8b shows the setup, where the tag is mounted on a tripod and placed 1 m in front of the reader. The reader consists of two horn antennas in orthogonal orientation and a Vector Network Analyzer (VNA) for transmission of the interrogation signal with a Tx power of 6 dBm and reception of the backscatter.

In order to proof the temperature-sensing concept, a heat gun has been placed next to the tag and the temperature has been controlled under support of an infra-red camera.

The received backscatter signal in the setup consists of three superimposed parts: first, the crosstalk between the two reader horn antennas, which is at a level of

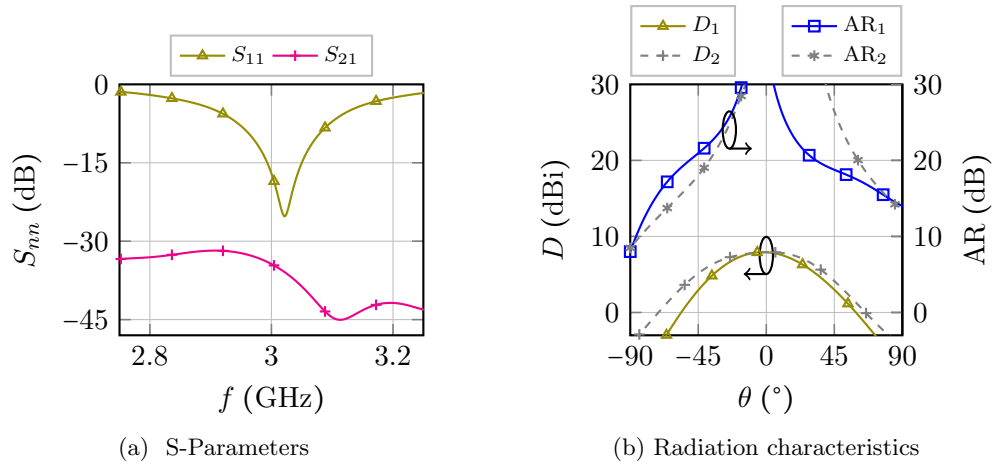


Figure 4.6.: Simulation result of the patch antennas (compare Figure 4.5a): (a) scattering parameters for matching and crosstalk; (b) directivity (D) and axial ratio (AR) in the $\phi = 0^\circ$ plane for patch antenna 1 and in the $\phi = 90^\circ$ plane for patch antenna 2.

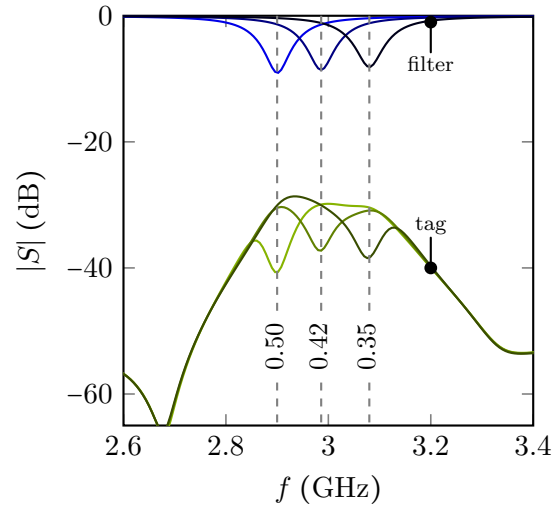


Figure 4.7.: Simulated normalized Rx signal of the crosspolar tag (lower part) and transmission behaviour of the notch filter (upper part), given for three different capacitance values. The capacitance value C_{var} in pF is labeled on the dashed notch marker.

4. Chipless Sensing Concepts

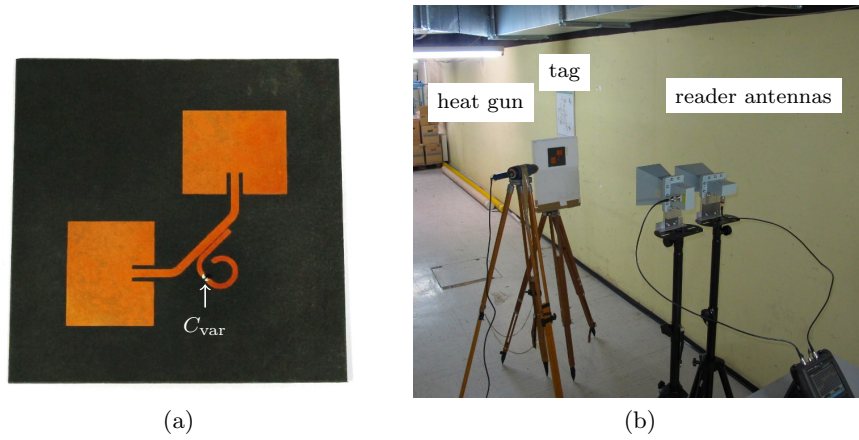


Figure 4.8.: (a) A photograph of the dual-polarized sensor tag with the BST varactor from Section 3.1 and (b) a photograph of the wireless measurement setup with a tag-to-reader distance of 1 m; © 2012 IEEE, [Kub+12a] refers.

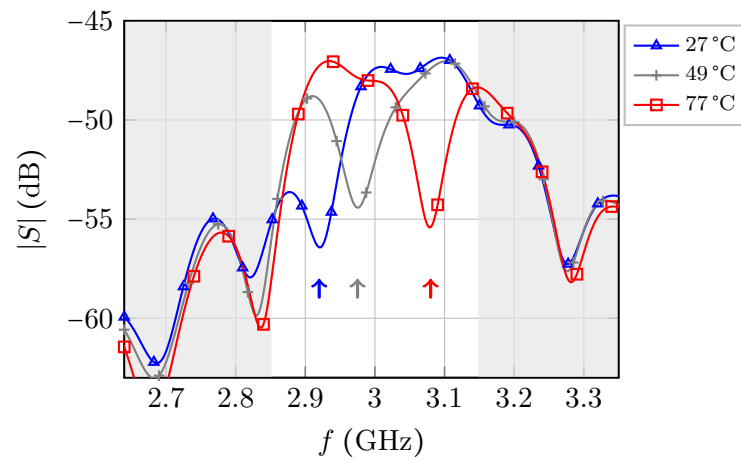


Figure 4.9.: Measured Rx signal of the dual-polarized sensor tag for different temperatures.

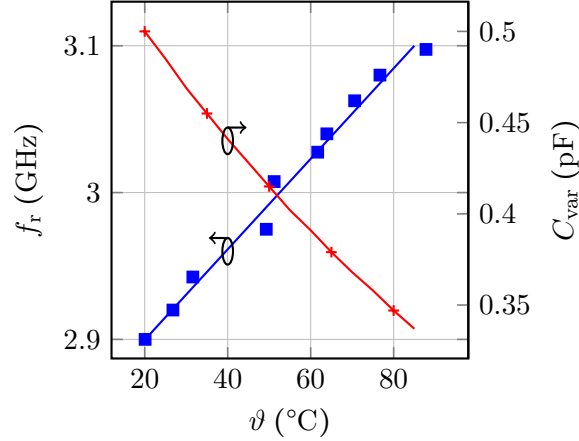


Figure 4.10.: Measured resonance frequency f_r and capacitance C_{var} in dependence of the temperature ϑ .

–40 dB normalized to the Tx power, second the wanted tag signal, and third reflections from the environment, i.e. the depolarized clutter. The tag signal represents a filtered and attenuated reflection of the Tx signal. It can be extracted from the signal superposition by time-gating, as the crosstalk arrives at early time instants and the clutter at late instants. In the given scenario the tag signal is detected by gating from 10 to 24 ns. In order to setup the gating, an approximate knowledge of the tag-to-reader distance d is beneficial.

The gated response is plotted in Figure 4.9 for three different temperatures. It shows the bandpass transmission response of the patch antennas as well as the notch of the transmission line filter. The notch shifts to higher frequencies with increasing temperature, as has been expected from simulations. A careful comparison between measured and simulated backscatter signals, Figure 4.9 versus Figure 4.7, shows undoubtedly the predicted transmission behaviour. Yet, the measurement signal carries additional ripples, that are caused by truncation of the tag signal by the time gating and by weak interferences of non-cancelled crosspolar clutter. These ripples decrease with decreasing tag-to-reader distance d . In the given scenario, the ripples can be accepted for a successful readout for distances up to 1.25 m.

The shift of the resonance notch has been evaluated in dependence of temperature ϑ and plotted in Figure 4.10. The notch is detuned from 2.9 GHz upwards by 198 MHz, when heating from 20 °C to 85 °C. This temperature dependence is linearly approximated as shown with the regression curve in the figure, from which slight measurement offsets are visible. These offsets are mainly caused by measurement inaccuracies related to the temperature control with heat gun and infra-red camera. According to the resonance shift, the sensor shows an absolute sensitivity of $\Delta f_r / \Delta \vartheta = 3.1 \text{ MHz/K}$.

As mentioned earlier, the resonance shift is caused by the varactor's temperature-dependent capacity. This dependence is derived from the resonance shift and plotted

4. *Chipless Sensing Concepts*

as well in Figure 4.10. The capacity decreases by 32.6 %, from 0.5 pF at room temperature to 0.34 pF at 85 °C.

The presented measurements proof the crosspolar chipless concept. A wireless detection of the tag temperature is possible when applying adequate time-gating. The approach is suitable as long as the environment does not cause strong crosspolar clutter within the time-frame of the tag backscatter signal.

Further analysis of the performance of the wireless reading is found in Section 4.4.

4.2. The Harmonic Radar Concept

A harmonic radar system uses two frequency bands, the fundamental transmit band at f_1 and the harmonic response band at f_n , where the harmonic frequency is an integer multiple of the fundamental $f_n = n f_1$. Consequently, Tx and Rx paths are split in frequency domain. For a chipless system this approach can bring a significant advantage: The radar clutter² that often causes serious disturbance of the wanted signal, is caused by linear reflection of the incident radar pulse at dielectric or metallic boundaries. This way it occurs only at the fundamental frequency. The wanted tag signal, in contrast, lies at the harmonic frequency, as it is generated by non-linear harmonic generation. As a result, the backscatter reading is practically clutter-free and a simple detection of the wanted tag signal becomes possible. It is noted, that, under close observation, environmental objects can as well show non-linear reflection behaviour. [Dan10] reports on harmonic signals generated by metallic objects, such as cable shackles or vehicle components. Yet, their backscatter strength is usually negligible.

The basic idea of harmonic radar has been used in a limited number of applications. In most cases, harmonic radar tags are used to provide simple remote information with passive tags:

- in shopping centers for anti-theft protection; harmonic radar tags that are attached to textiles are detected at the shop's exit, when not removed or deactivated at the cash desk [Fin03].
- in avalanche rescue systems; harmonic radar tags are sewed into mountain sportswear in order to ease the localization of people buried under the snow [REC].
- in localization tasks; miniature harmonic tags have been mounted onto insects to detect and track their movements [Ril+96].

In these applications the harmonic tag supplies principally only notification about its presence or absence³, which can be referred to as 1 bit of information.

The subsequently presented temperature sensor extends the harmonic radar concept in order to transmit more information from the tag to the reader: In addition to the presence information, an analog temperature measurand. Only few publications are found which discuss such chipless harmonic radar sensors. A theoretical [Bac+12] and a practical study [Vol+08] use amplitude modulation of the harmonic in order to measure gas concentration or metal corrosion. These amplitude modulations have the downside of being sensitive to the reading distance, to the antenna orientation and to the existence of objects in the line of sight and are hence, only

²Compare Section 2.3 for an introduction of the term clutter.

³Even in localization tasks, run-time and direction information comes rather from the reader, than from the tag.

4. Chipless Sensing Concepts

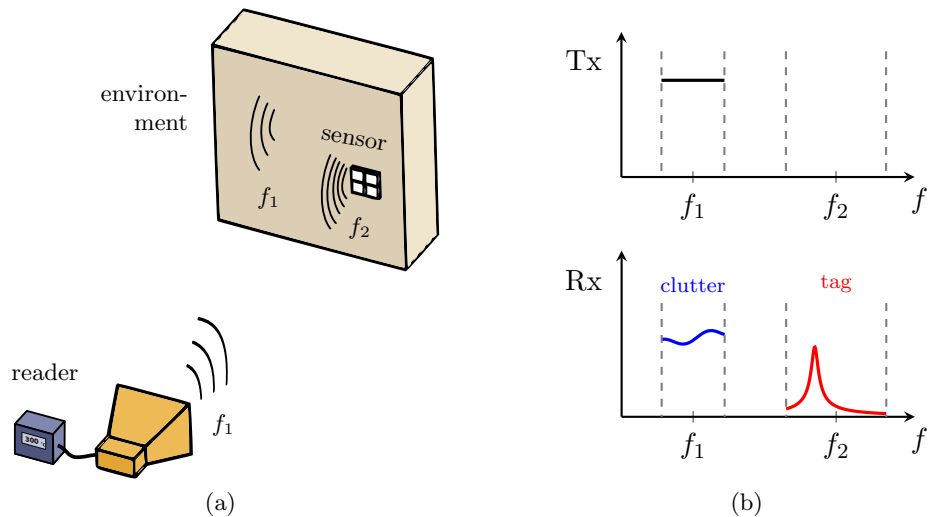


Figure 4.11.: Harmonic radar sensor principle.

weakly suitable for dynamic application scenarios. In order to circumvent this drawback, the subsequently presented sensing method uses frequency position encoding⁴ of the measurand. With this approach two temperature sensor tags have been developed. They are presented in the following subsections and have been published in [Kub+14b], [Kub+14c] and [Kub+15].

The principal setup of the approach is sketched in Figure 4.11. The harmonic radar sensor is placed inside the measurement environment. The reader radiates the interrogation signal at the fundamental frequency band at f_1 . The sensor receives the interrogation signal, doubles its frequency to f_2 , bandpass-filters the signal to create a transmission peak and backscatters the filtered harmonic. The reader will receive the harmonic backscatter and derive the measurand from the peak position. As described above, the environmental clutter lies in the band at f_1 and hence, will not interfere with the useful harmonic. A key element of the sensor tag is then the harmonic generator, which requires a passive non-linear transmission element. Here, principally any device non-linearity can be exploited. Yet, for chipless wireless sensors tags, low input powers and the non-existence of a biasing voltage or pump power have to be considered in the choice. Zero-bias Schottky diodes show comparatively high suitability and have been chosen for the presented tags.

In this context, the non-linear element/diode might open up a question about the denotation as *chipless*. In a strict sense, the tag diode might not hold for the description *operation without semiconductors*. Yet, the tag still operates passive, battery-less and does not harvest energy. Neither, does a single unbiased diode provide (digital) logic. A single diode will probably also not count as an integrated circuit. Therefore, the denotations ‘chipless’ [Pal+15], ‘quasi-chipless’ [Kub+14b],

⁴Compare Section 2.2

‘zero-power’ [AR13], ‘powerless’ [Man+14] or simply ‘harmonic’ [Vol+08] are found for tags with non-linear elements in literature. Throughout this thesis no strict differentiation between the terms chipless sensors and non-linear-chipless sensors is taken as the proof of harsh environment operation is not directly expressed by any of the terms. By replacing the silicon diode by a suitable non-silicon semiconductor diode (e.g. [Ves+97]), a metal-insulator-metal junction or a metal-to-metal junction high-temperature operability of the harmonic sensors can be developed.

4.2.1. Harmonic Radar Sensor Tags

Two harmonic radar temperature sensors have been developed, namely tag A, which has first been published in [Kub+14b] and tag B, which has been published in [Kub+15]. Their setups and performance characteristics are described in the following. Wireless measurement results of the whole tags are found in Section 4.2.2 and in Chapter 4.4. Both sensor tags have a similar working principle: They both receive the reader’s radar pulse, double its frequency to the first harmonic, generate a transmission peak by bandpass filtering and backscatter the filtered harmonic signal. This way, the Rx power P_{Rx} , that is received by the reader can be described by a modified link budget equation. For a tag-to-reader distance d , it is given in logarithmic scale

$$P_{\text{Rx}} = \underbrace{P_{\text{Tx}} + G_{r1} - a_{fs1} + G_{t1} - a_{t1}}_{P_{\text{in}}} + G_{\text{HG}}(P_{\text{in}}) + G_{t2} - a_{fs2} + G_{r2} \quad (4.10)$$

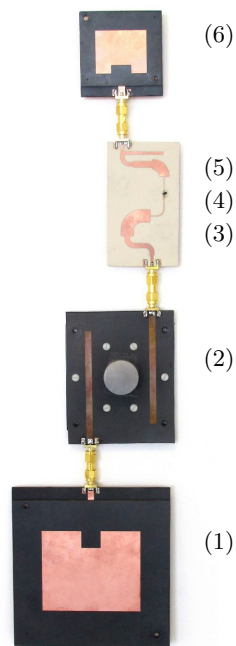
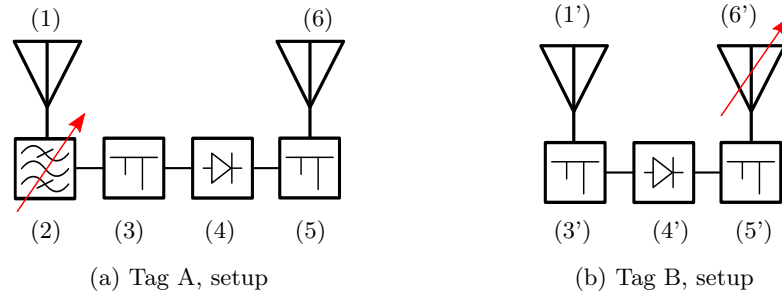
when the reader’s Tx power is given by P_{Tx} , the reader’s Tx and Rx antenna gains by G_{r1} and G_{r2} and the free-space path loss at the fundamental frequency by $a_{fs1} = 20 \log_{10}(4\pi d f_1/c_0)$ and by $a_{fs2} = 20 \log_{10}(4\pi d f_2/c_0)$ at the harmonic frequency. The tag receives and backscatters the reader interrogation with antenna gain G_{t1} and G_{t2} , and introduces additional tag losses (e.g. on transmission lines or the filter) expressed by a_{t1} . The input power P_{in} , that is fed into the harmonic generator on the tag, is hence, strongly dependent on the parameters of the fundamental link and influences the gain G_{HG} of the non-linear conversion from fundamental to harmonic frequency.

Tag A operates with a fundamental frequency bandwidth of 180 MHz at 1.56 GHz. The operating frequency of tag B is approximately double the one of tag A. Tag B’s fundamental band lies at 3.05 GHz with a bandwidth of 100 MHz. Both tags are setup planar, use microstrip transmission lines and have been fabricated in a standard PCB process.

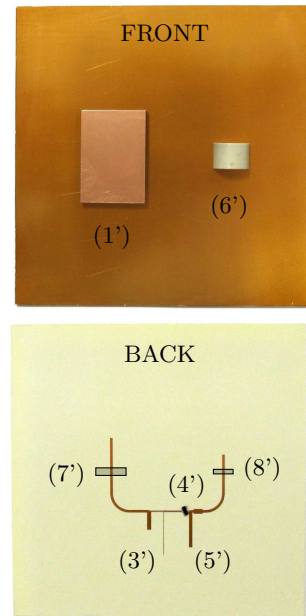
Tag A

Tag A is setup modular and consists of four components as shown in Figures 4.12a and 4.12c. Each component is manufactured on a single substrate, the substrates are interconnected with SMA adapters. The four components are a receiving antenna,

4. Chipless Sensing Concepts



(c) Tag A, photo



(d) Tag B, photo

Figure 4.12.: Components and photographs of the two harmonic radar sensors. (1), (1') Rx antenna; (6), (6') Tx antenna; (2) temperature-tunable filter; (3), (3') input matching network; (4), (5') diode; (5), (5') output matching network; (7'), (8') coupling slot. For c) © 2014 IEEE, [Kub+14c] refers; for d) © 2015 IEEE, [Kub+15] refers.

a temperature-dependent bandpass filter, a harmonic generator and a transmitting/backscatter antenna:

- The **Rx antenna** is setup as a stacked patch antenna that is center-fed from a microstrip line. This antenna type has been chosen in order to cover the desired frequency bands, to achieve a broadside radiation pattern and in order to allow for on-metal mounting as expected in many sensing environments. The **Tx antenna** is designed in analogy to it. The antenna consists of two radiating metal patches, each on a Rogers RT/duroid 5880 substrate with 1.58 mm thickness. The patches measure $74.4 \times 62.0 \text{ mm}^2$ for the reception at 1.56 GHz and $36.6 \times 30.5 \text{ mm}^2$ for the harmonic band. The lower patch element uses an inset feed to match the impedance of the radiator to 50Ω .

The measured antenna gain of the backscatter antenna is plotted in Figure 4.14a versus frequency. It is maximally 6.5 dBi, and larger than 3.5 dBi in the band from 2.94 to 3.3 GHz. The 3 dB bandwidth of the stacked patch is about 2.5 times larger than the bandwidth of a simple patch on the same substrate.

- The **bandpass filter** is designed as a symmetric microstrip-coupled DR as sketched in Figure 4.13a. An incoming RF signal is coupled to the output port only when exciting resonance in the DR. In detail, the $\text{TE}_{01\delta}$ is excited in the design, which is coupled mainly magnetically to the open-ended microstrips. The center of the DR is therefore placed at the H -field maxima at $\lambda/4$ from the open ends and the distance between DR and microstrip determines the coupling coefficient. The resonance frequency of the DR on the substrate can be approximated by the model of Itoh and Rudokas [IR76] in order to ease the design process.

With a radius of 12.7 mm, a height of 10.4 mm and a relative permittivity of 85, the filter is designed for a center frequency of 1.56 GHz at room temperature. The measured forward transmission characteristic of the filter is shown in Figure 4.14c. The transmission peak shows a resonance Q -factor of 510. Due to the temperature-dependence of the ceramic dielectric with a temperature coefficient⁵ of $\tau_\epsilon = -760 \text{ ppm/K}$ at 20°C , the resonance peak shifts towards higher frequencies with increasing temperature.

- The layout of the **harmonic generator** of tag A is shown in Figure 4.13c. The generator consists of a single unbiased Schottky diode, namely Avago HSMS2850 and two matching networks. The complex diode impedance, which shows a small real part and highly capacitive imaginary part, is matched to the 50Ω line impedance on the input and output side by the matching networks. This matching is realized with stepped impedance $\lambda/4$ lines to match the real parts and a high-impedance line to match the imaginary parts. The matching networks are designed comparatively broadbanded to cover a fundamental frequency band from 1.47 to 1.65 GHz. Furthermore, a $\lambda/4$ open stub is placed

⁵Compare Section 3

4. Chipless Sensing Concepts

on the output side to suppress transmission of the fundamental frequency and to increase the conversion gain.

The measured conversion gain of the harmonic generator is plotted in Figure 4.15b versus input frequency and in Figure 4.15c versus input power at a center frequency of 1.56 GHz. For an input power of -20 dBm, which represents a typical value in a wireless scenario, the conversion gain is -28.5 dB at the center frequency and decreases with decreasing input power. The course of the conversion gain versus frequency in Figure 4.15b shows perceptible ripples, which indicate a leakage of the harmonic frequency to the input side. This leakage can influence the conversion gain when the input side is not perfectly matched to $50\ \Omega$ at the harmonic frequency. The harmonic leakage is then reflected back into the diode. This case is given in the assembled tag due to the rejection of the DR filter ahead. The conversion gain of the tag is hence only known with an uncertainty of about 3 dB, the height of the ripple.

Tag B

Tag B consists of three components, that are integrated onto a single hybrid substrate as shown in Figures 4.12b and 4.12d. The components are a receiving antenna, a harmonic generator and a temperature-tunable backscatter antenna, that is setup as a DRA:

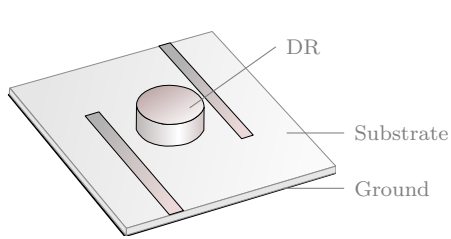
- the **Rx antenna** is setup as an aperture-coupled patch antenna. The rectangular radiating patch element measures $21.5 \times 30.5\ \text{mm}^2$ and is made from a 3.18 mm thick Rogers RT/duroid 5880 substrate. The patch is placed centered onto a coupling slot and glued onto the front side (ground side) of the base substrate. The RF signal is then coupled through the slot to the $50\ \Omega$ microstrip line on the backside.

The simulated radiation pattern of the patch antenna is shown in Figure 4.14b for the H -plane. It shows a broadside beam with a half-power beamwidth of 66° and a backside radiation rejection of at least 15.2 dB. The maximum gain is calculated to 8.1 dBi as plotted in Figure 4.14a versus frequency. The 3 dB bandwidth ranges from 2.96 GHz to 3.2 GHz.

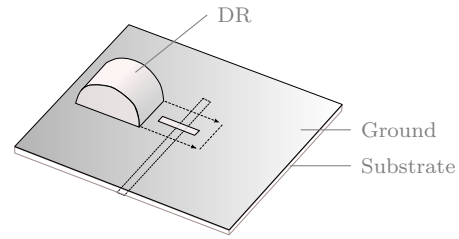
- the **harmonic generator** of tag B is placed on the back side of the substrate. It uses the same diode as tag A. Matching networks are placed at the input and output side of the diode in order to match to $50\ \Omega$ and to maximize the conversion gain. The matching is realized with stepped impedance lines and open stubs as shown in the layout of Figure 4.13d. Additionally, two $\lambda/4$ open stubs are used to reject transmission of the fundamental frequency to the output side and leakage of the harmonic frequency to the input side.

The result of the matching efforts are shown in Figure 4.15a. The measured reflection coefficient is lower than -4.1 dB at the input side in the fundamental

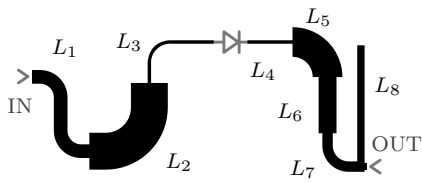
4.2. The Harmonic Radar Concept



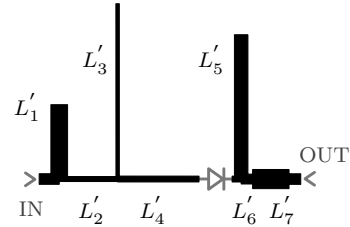
(a) Tag A, DR filter



(b) Tag B, DR antenna



(c) Tag A, harmonic generator



(d) Tag B, harmonic generator

	l	Z_w
L_1	$\lambda_1/4$	33Ω
L_2	$\lambda_1/4$	15Ω
L_3	$\lambda_1/5$	100Ω
L_4	$\lambda_2/5$	100Ω
L_5	$\lambda_2/4$	18Ω
L_6	$\lambda_2/4$	27Ω
L_7	$\lambda_2/4$	40Ω
L_8	$\lambda_1/4$	50Ω

(e) Tag A, line segments

	l	Z_w
L'_1	$\lambda_2/4$	40Ω
L'_2	$\lambda_1/12$	73Ω
L'_3	$\lambda_1/3$	100Ω
L'_4	$\lambda_1/8$	69Ω
L'_5	$\lambda_1/4$	44Ω
L'_6	$\lambda_2/60$	50Ω
L'_7	$\lambda_1/8$	36Ω

(f) Tag B, line segments

Figure 4.13.: Tag components: a) temperature-tunable DR filter, b) temperature-tunable DR antenna, c), d) layouts of the harmonic generators, e) f) transmission line length and impedances of c) and d).

4. Chipless Sensing Concepts

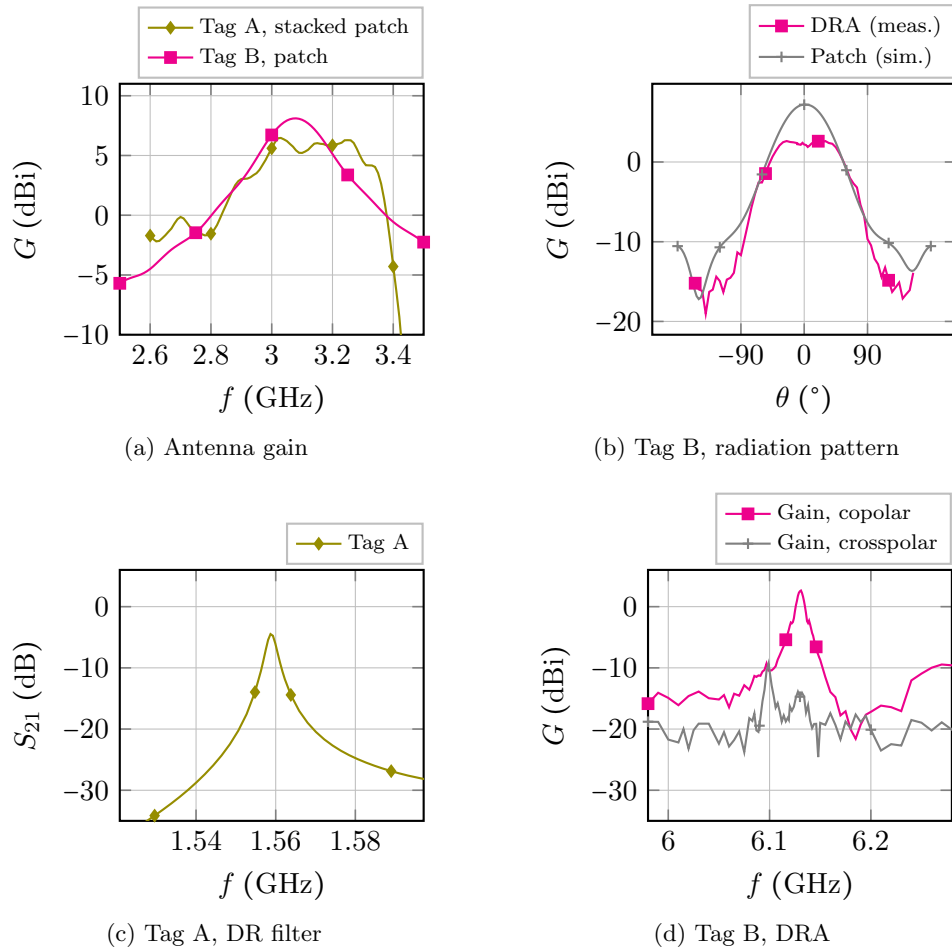
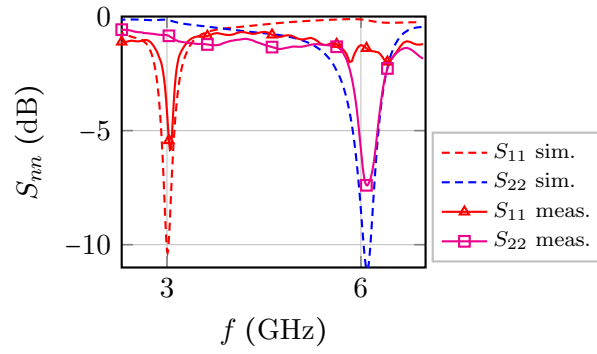
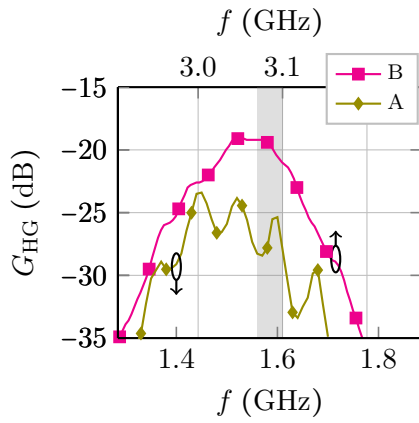


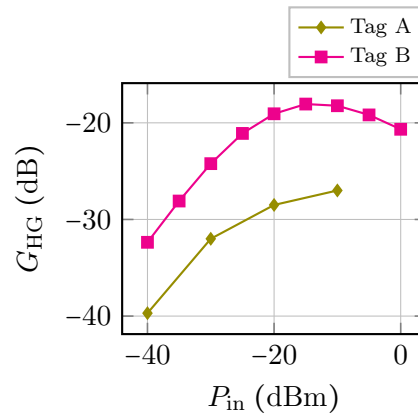
Figure 4.14.: Measured characteristics of the (broadband) tag antennas of Tag A and B, of the temperature-dependent (narrowband) filter of Tag A, and of the temperature-dependent (narrowband) DRA of Tag B.



(a) Tag B, HG matching



(b) HG, conversion gain vs. frequency



(c) HG, conversion gain vs. input power

Figure 4.15.: Measured and simulated characteristics of the harmonic generators (HG) of Tag A and B.

4. Chipless Sensing Concepts

band from 3.0 to 3.1 GHz and lower than -5.8 dB at the output side in the backscatter frequency band from 6.0 to 6.2 GHz. The desired leakage rejection is indicated by the non-matched reflection levels at other frequencies. The figure also shows the simulation result of the matching circuit. The simulated matching is notably better than the measured, which is in first line caused by fabrication and mounting tolerances in relation to the diode impedance and its package.

The measured conversion gain of the harmonic generator is plotted in Figure 4.15c versus frequency for an input power of -20 dBm. The conversion gain has a maximum of -19.1 dB and is higher than -22.6 dB throughout the frequency band of 6.0 to 6.2 GHz. At the center frequency, the measured conversion gain (which is not shown in the plot) is only 2.4 dB lower than the simulated one. This difference indicates the potential for gain improvement by further matching optimization. Figure 4.15b shows the conversion gain versus input power at the center frequency of 6.1 GHz. The plot describes a reduced conversion gain for decreasing input powers, as expected at large tag-to-reader distances in a wireless scenario. For large input powers, above -10 dBm, the conversion gain decreases as well. This behaviour is caused by the power-dependence of the diode impedance, which leads to a reduced impedance matching.

- the **DRA** of tag B fulfills two functionalities: temperature-dependent bandpass filtering and backscattering of the harmonic signal. The DRA consists of a half-split ceramic cylinder on the front side ground of the base substrate and its feeding from a microstrip line on the back side via a coupling slot. The DR is glued centered onto the slot as sketched in Figure 4.13b. Inside the DR the (half-split) $\text{EH}_{111+\delta}$ mode is excited. This mode can be described by two electric dipoles standing normal on the ground area. The mode has been chosen due to its comparatively high radiation quality factor and broadside radiation beam as described in Section 3.2.1. The high Q factor generates a transmission peak, that is narrow compared to the bandwidth of the Rx antenna and to the conversion-bandwidth of the harmonic generator.

Important aspect in this antenna design is the coupling from the microstrip to the DR. First, the coupling strength determines the loading of the resonator to the $50\ \Omega$ system impedance. An increasing coupling strength leads to an (undesired) decrease of the resonance Q on the one hand, but also to a (desired) increase of the antenna gain on the other hand. Second, does the slot introduce metallic losses, which reduce the antenna efficiency. Third, a ‘clean’ excitation only of the desired mode and not of neighboring or parasitic modes is of high importance. Due to the latter reason, has the ground-side of the half-cut cylinder (with exception of the slot area) been metallized by evaporation and electroplating. As a perfect planar fit of the DR onto the substrate ground is practically impossible, this additional metallization circumvents the existence of a metal-air-dielectric transition from substrate ground to ceramic

and creates instead a metal-air-metal transition. This effort has eased the excitation of the $\text{EH}_{111+\delta}$ mode significantly. The coupling slot is aligned centered, perpendicular to the propagation direction of the microstrip line and placed at $\lambda/4$ from its open end. This way, the microstrip's perpendicular H -field can couple into the DR and locally excite the azimuth H -fields of the electric dipoles of the $\text{EH}_{111+\delta}$.

The DR cylinder measures a height of 8.4 mm and radius 6 mm, with a relative permittivity of 50 at room temperature. In similarity to the filter of tag A, does the DR permittivity show a temperature-dependency that leads to an increase of the resonance frequency with increasing temperature. The temperature coefficient of the chosen ceramic is $\tau_\epsilon = -200$ ppm/K at room temperature.

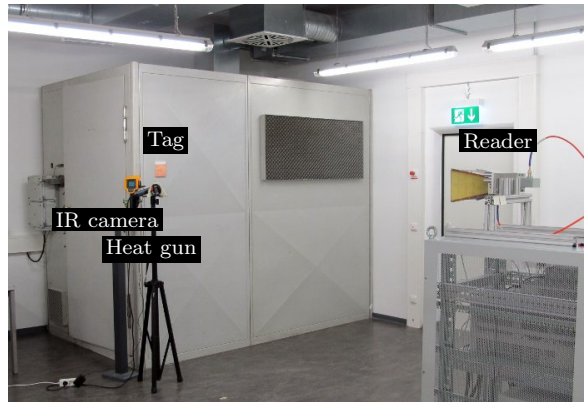
Besides being integrated into the sensor tag, has the DRA been manufactured as a single component with an SMA-to-microstrip adapter. This component allows for a measurement characterization. The radiation pattern of the DRA is plotted in Figure 4.14b, showing a broadside beam similar to the patch antenna. The tip of the DRA beam is slightly flattened, due to a uncritically weak superposition of a neighboring mode. The measured copolar gain in broadside direction is maximally 2.6 dBi as plotted in Figure 4.14d versus frequency for $\vartheta = 20^\circ\text{C}$. The gain shows a bandwidth Q -factor of 530. The figure also shows the measured crosspolar antenna gain, which indicates a crosspolar rejection of 16.5 dB at resonance and an (undesired) parasitic mode 32 MHz below the main peak with a rejection of 11.9 dB. Due to its weakness, this parasitic peak is negligible for usual wireless scenarios as the tag requires copolar excitation also on the Rx side. Yet, it can lead to sensing errors for bad alignment of tag and reader antennas.

A comparison of tag A and tag B reveals a few specific differences, that shall be noted. a) The main difference between the tags is their physical size. Tag A measures $37.5\text{ cm} \times 11.5\text{ cm}$ when assembled. Tag B has reduced this size by a factor of four to $10\text{ cm} \times 10\text{ cm}$. This size reduction has been the main motivation of the development of the second tag in order to increase the suitability of the approach for practical application. The size reduction has been obtained by increasing the operation frequency by a factor of two, by integrating the components onto a single hybrid substrate and by reducing the number of tag components from four to three. b) The harmonic generator of tag B has been improved compared to version A in terms of conversion gain and signal leakage. In the operation band, the conversion gain of tag B is at least 8 dB higher, which results from improved impedance matching. c) A comparison of the bandpass filters of the two tags (compare Figures 4.14c and 4.14d) reveals an advantage of the DR filter of tag A. The dedicated filter shows a cleaner peak generation with a higher rejection in the stopbands. This can lead to a more robust peak detection in wireless scenarios under low SNR and/or SIR values.

4. Chipless Sensing Concepts



(a) Setup of tag A



(b) Setup of tag B

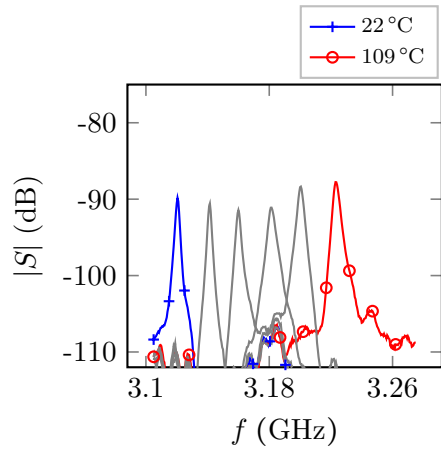
Figure 4.16.: Photographs of the wireless setups with a tag-to-reader distance of 1.5 m: In a) for tag A, © 2014 IEEE, [Kub+14c] refers; in b) for tag B, © 2015 IEEE, [Kub+15] refers.

4.2.2. Wireless Measurements and Temperature Sensing

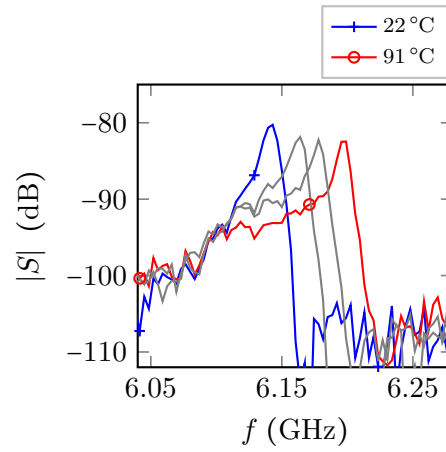
The harmonic radar tags A and B have been tested in wireless indoor scenarios. The first scenarios are described below and analyze the ability of a remote temperature measurement. The second scenarios are found in Chapter 4.4 and describe the measurement accuracy for different reading ranges, alongside with a comparison to the other chipless approaches of this thesis.

Figure 4.16 shows the wireless measurement setups for tags A and B. In both cases has the tag been mounted at a height of about 1.7 m on metallic building structures. For tag A, the DR and the harmonic generator are facing away from the reader antennas in order to reduce the reception of unwanted signal radiation from the DR filter or SMA-to-microstrip connectors of the assembly. The temperature of both tags has been controlled under support of an infra-red camera and a heat gun, that are located next to the tag on tripods. The reader consists of a signal generator, a receiver and two horn antennas connected to each. The Tx power is 10 dBm.

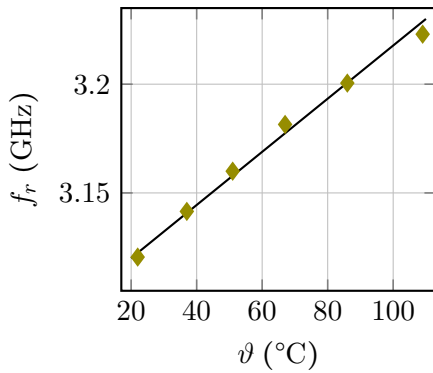
For a tag-to-reader distance of 1.5 m, the Rx spectrum of tag A is shown in Figure



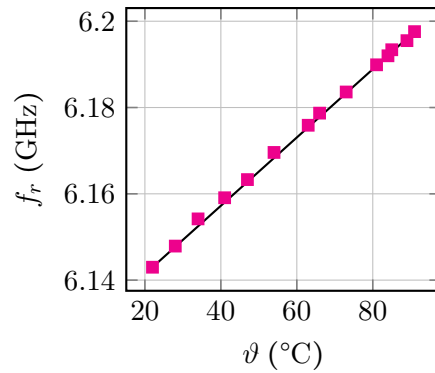
(a) Tag A, Rx Spectra



(b) Tag B, Rx Spectra



(c) Tag A, peak frequency



(d) Tag B, peak frequency

Figure 4.17.: Wireless measurement results of the two harmonic radar tags A and B. In a), b) measured Rx signals, normalized to the Tx power, at different temperatures, and in c), d) resonance frequencies versus temperature.

4. Chipless Sensing Concepts

4.17a. This spectrum is normalized to the Tx power and obtained without further signal processing. The figure shows the measurement for six different temperatures between 22 °C and 109 °C. The desired transmission peak is clearly recognizable and shifts to higher frequencies with increasing temperature. The peak power is around -90 dB and increases by approximately 2 dB for higher temperatures, which is most likely caused by ripples in the frequency-dependent conversion gain (compare Figure 4.15b). It becomes obvious that the Rx signal is free of radar clutter. The remaining signal distortions that are visible are due to receiver noise and the (above mentioned) unwanted tag radiation from connectors and the DR. Both, self-inflicted parasitic radiation and noise, are uncritically weak and do not harm the resonance detection in this scenario. The course of the harmonic resonance frequency of tag A in dependence of temperature is plotted in Figure 4.17c. The peak shifts linearly by 102 MHz from 3.121 to 3.223 GHz, when heating to 109 °C. This shift relates to a temperature sensitivity of $\Delta f_r/\Delta\vartheta = 1.2\text{ MHz/K}$ and a temperature coefficient of $\tau_f = \Delta f_r/(f_r \Delta\vartheta) = 380\text{ ppm/K}$, when normalizing to the operation frequency.

The Rx spectra of tag B are plotted in Figure 4.17b. Here, the tag temperature has been varied from 22 °C to 91 °C which results in a clearly visible resonance shift. The normalized Rx peak power is around -80 dB for a distance of 1.5 m. The dependence of the peak frequency on temperature is plotted in Figure 4.17d. The resonance reacts with a sensitivity of 0.79 MHz/K to increasing temperatures, which relates to a temperature coefficient of $\tau_f = 128\text{ ppm/K}$.

In comparison to tag A, tag B shows an about 10 dB higher Rx power for identical distances. This difference is partly caused by the higher conversion gain and reduced tag losses of version B. Despite lower Rx power, the resonance peaks of tag A are slightly easier to distinguish, which is caused by the higher stopband rejection of the DR filter, by the higher temperature sensitivity of its ceramic and by the nonlinear conversion of the DR filter characteristic (in the downstream harmonic generator). In fact, this nonlinear conversion increases the peak Q by roughly 50% compared to the linear filter characteristic (compare Figure 4.14c).

4.3. The High-Q Resonator Concept

This section introduces a chipless sensing concept, that is based on the slow decay of an EM resonance with low damping ratio. The concept includes basically three steps: first, the wireless excitation of an RF resonator by the reader's interrogation signal. Second, the reception of the backscatter signal, which includes the wanted radiation from the resonator as well as unwanted clutter. And third, the detection of the resonance signal by time-gating of the backscatter signal.

In relation to the first and second step, the RF resonator must be coupled to free-space. The coupling allows for both, the wireless excitation, as well as the transmission of the backscatter. The free-space coupling can either be realized by coupling the resonator to an additional antenna, or by using an antenna structure as resonator. These two types are denoted as loaded antenna, respective, shorted antenna in the introductory Section 2.2.

In order to realize sensing functionality, the resonator is designed to be sensitive to the measurand. I.e., the resonance frequency is detuned by changes of the measurement value, what is referred to as frequency-position encoding in Section 2.2.

In relation to the detection of the resonance backscatter, the resonance duration is of importance. The approach requires that the resonance decays slower than the clutter of the environment. As introduced in Section 2.3 the total power of the tag signal is usually significantly weaker than the total power of interferences from the reader antenna mismatch and environmental clutter. Yet, in many applications, the energy inside a low loss resonator at late time instants can be larger than the clutter, which decays faster. This allows for a detection at late time instants, realized by time-gating of the Rx signal as shown in Figure 4.18. The approach can therefore be understood as a Time Domain separation of clutter and tag signals. Figure 4.18b depicts the components of the received baseband signal s , which includes decaying power from a radiating resonator. The time constant τ of the exponential resonance decay

$$\tau = \frac{Q_0}{\pi f_r} \quad (4.11)$$

is proportional to the relation between the resonance quality factor Q_0 and the resonance frequency. It is consequently inversely proportional to the absolute resonance bandwidth. In logarithmic scale the resonance time decay is seen as a linear decrease with slope m ,

$$m = - \frac{\Delta s|_{\text{dB}}}{\Delta t} = \frac{20 \log(e)}{\tau}. \quad (4.12)$$

It is observed, that increasing the resonance Q will slow down the decay. All loss mechanisms of the resonator reduce the time constant τ and the total resonance quality factor

$$\frac{1}{Q_0} = \sum_i \frac{1}{Q_i} \quad (4.13)$$

is calculated from the summation of all individual loss quality factors Q_i . The individual loss factors usually include the radiation losses, given by Q_{rad} , dielectric

4. Chipless Sensing Concepts

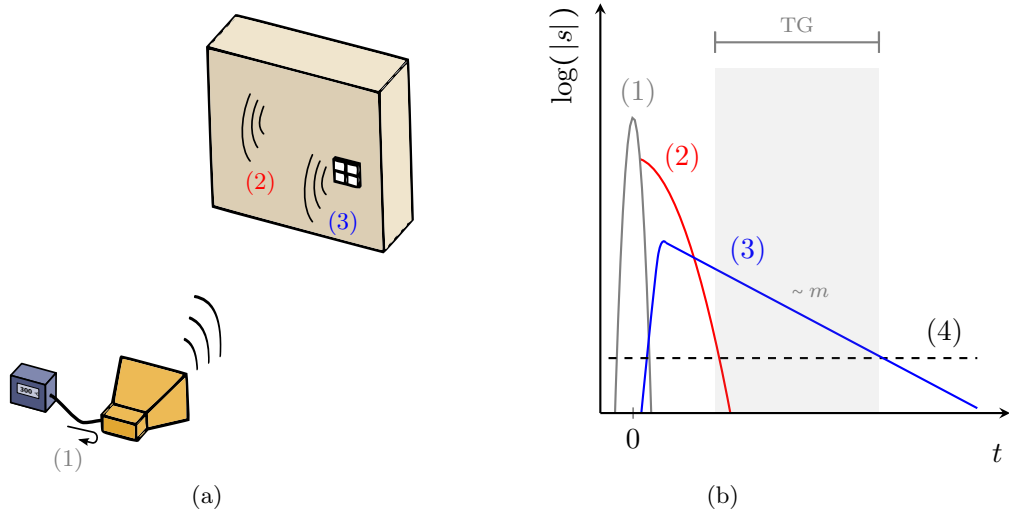


Figure 4.18.: Concept of the high- Q sensor: (a) schematic of reader and sensor in the environment; (b) baseband Rx signal in time domain, which consists of mismatch (1), clutter (2), sensor resonance (3), and noise (4). The time gate (TG) is marked.

losses, given by Q_{mat} as well as metallic losses, Q_M .

The approach of using time-gated resonances for the purpose of chipless wireless sensing has been introduced in [TCB09]. Here, a metallic cavity resonator is designed for pressure sensing in structural health monitoring. Another metal cavity sensor is presented in [Gha+13], which is capable of measuring temperatures up to 150°C . The slot antenna resonator in [CEG12] can as well be counted under the high- Q time-gating approach. The presented resonator allows for temperature sensing up to 1000°C , but has a reported read range of only 3 cm.

The high- Q resonator sensor presented in this work is based on a free Dielectric Resonator (DR). This approach allows for wireless sensing in temperature ranges significantly beyond 150°C , while at the same time having read ranges larger than 50 cm.

The design of the DR sensor has been chosen due to the following benefits compared to the named works: a) The DR is directly coupled to free-space, which avoids potentially lossy and temperature-unstable feeding structures; b) The DR is chosen with a lossless dielectric and avoids lossy metal conductors on its surface, to allow for high resonance Q even at high temperature; and c) Due to its high permittivity, the sensor benefits from a size reduction compared to an air-filled cavity. Temperature stability is achieved with the choice of a suitable ceramic DR material. The sensor has first been introduced in [Kub+13b].

4.3.1. Dielectric Resonator Sensor Tag

The design of the high- Q sensor is mainly oriented on three goals. First, the goal of generating a resonance with high quality factor in order to ease the TD separation of tag signal and clutter. Second, the operability at high temperature, and third, the desire for size compactness. These goals are of course (partly) oppositional. In order to meet them in an adequate compromise, the presented sensor is realized as a free DR and therefore named Dielectric Resonator Sensor (DRS).

Concerning the first goal and an operation frequency between 1 and 10 GHz, a usual free DR can excite resonance Q s, in ranges up to 5000.⁶ This quality factor can be compared to planar transmission line resonators, which have quality factors usually below 300 and metal cavity resonators, which can reach Q s in ranges up to 20000. Although, the potential quality factor of a DR is usually smaller than the potential Q of a hollow cavity, the DR will be smaller in size when high permittivities are used. This aspect refers to the third goal.

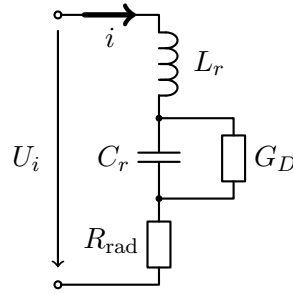
During operation of the sensor, a resonant mode is excited within the DR. Here, the choice of an adequate resonance mode is of importance. The mode should a) show a sufficiently high radiation quality factor in order to allow for the TD separation of tag signal and resonance, b) show a suitable radiation pattern, including a sufficiently high resonant RCS in the excitation direction, and c) should preferably be symmetrical to an electric wall inside the DR.

Aspects a) and b) refer to the detection of the sensor by time-gating, whereas aspect c) will allow for a mounting of the DR on a metal ground when split into half. The latter aspect is desired due to three reasons: 1) it allows for a direct on-metal mounting of the tag, e.g., on machines or tools in an application scenario; 2) it increases the resonant RCS by a factor of two, due to the mirrored EM fields; and 3) it reduces potential multipath propagation effects as backside radiation is suppressed.

The magnitude of the backscatter power of the DRS can be modeled with the equivalent circuit of Figure 4.19a. This circuit is based on the equivalent circuit of a shorted antenna in receiving mode as introduced in Figure 2.2a in Section 2.1. The DR is described by a series LC resonator with an ohmic resistance, representing dielectric losses, and the radiation resistance, that represents the radiation losses. The RCS of the DR is directly proportional to the power that dissipates in the radiation resistance. Figure 4.19b shows the RCS of the DR versus frequency. The resonant behaviour is observed as a peak in the spectrum. The smallest possible 3 dB peak bandwidth width is determined by the radiation quality factor Q_{rad} . Increasing dielectric losses reduce the magnitude of the RCS and increase the peak bandwidth. Additionally, it is observed that the magnitude of a high Q resonance is more sensitive to losses, than a low Q resonance. This is seen in the comparison between Figure 4.19b and Figure 4.19c, which refer to radiation quality factors of 780 and 195.

⁶The total Q of the DR is mainly limited by the dielectric material losses, which are seldomly smaller than $\tan \delta$ around 1×10^{-4} , compare (4.13).

4. Chipless Sensing Concepts



(a)

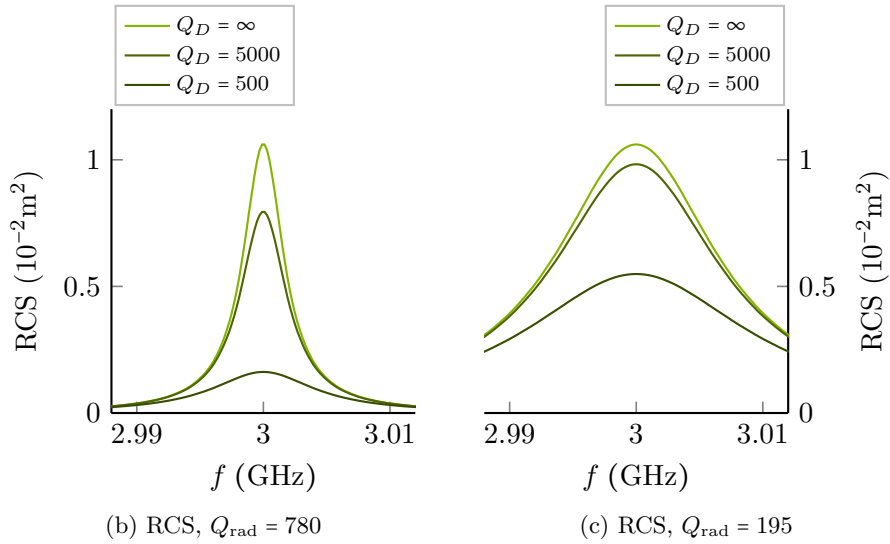


Figure 4.19.: (a) Equivalent circuit of a DR in a backscatter scenario, (b) and (c) RCS of the $\text{TE}_{011+\delta}$ mode versus frequency, for two different radiation quality factors and varying dielectric loss factor.

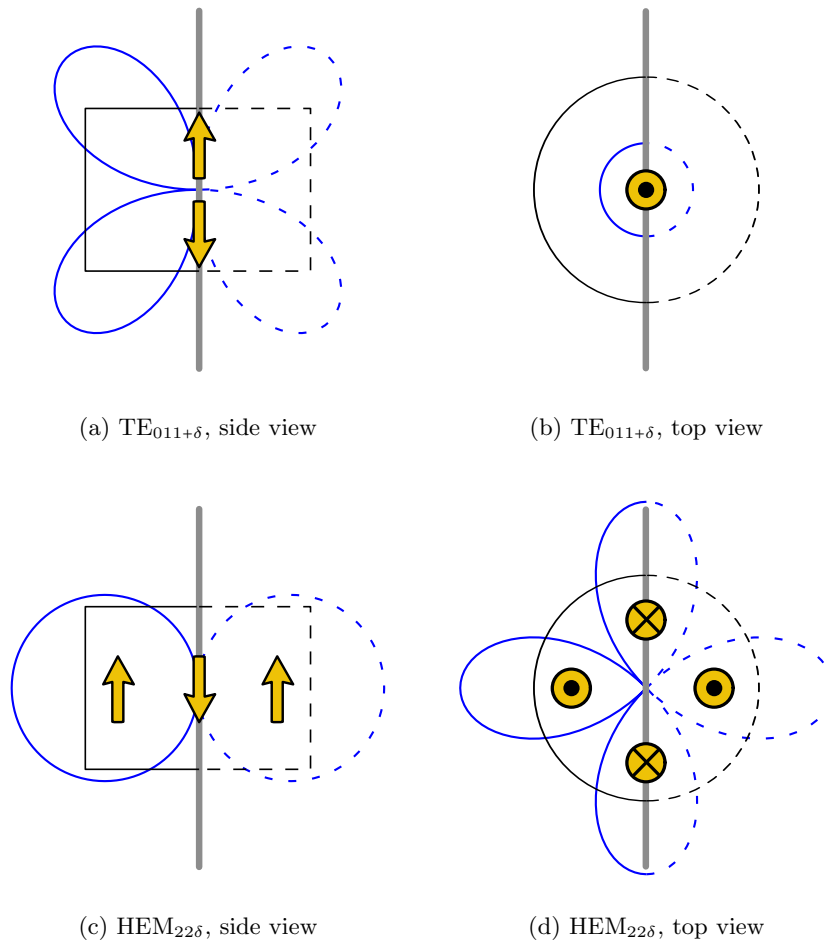


Figure 4.20.: DR modes on a metallic plane with magnetic dipoles (yellow arrows), and radiation pattern (blue lines). The dashed lines indicate the mirrored parts.

4. Chipless Sensing Concepts

Setup

According to the design goals discussed in the previous section, the DRS is setup as a half-split ceramic cylinder that is mounted on a metallic ground plane. The dielectric cylinder measures $h = 15$ mm in height, $\rho_0 = 20$ mm in diameter and is made of a ceramic with a relative permittivity of $\epsilon_r = 49.5$ at room temperature. The ceramic is denoted as K-50 in Sections 3.1 and 3.2.2. Its temperature-dependent permittivity and the dielectric loss tangent have been characterized and are given in Section 3.2.2. The basic setup of the DR sensor has been published in [Kub+13b].

In order to find a suitable DR mode, radiation properties of some modes have been introduced in Section 3.2.1. It has been observed, that the radiation quality factor Q_{rad} generally increases with increasing permittivity and with increasing mode order.

The presented sensor has been specifically designed to use either the $\text{TE}_{011+\delta}$ mode with resonance at 2.8 GHz or the $\text{HEM}_{22\delta}$ with resonance at 3.65 GHz. The dipole representations as well as the radiation patterns of these two modes are shown in Figure 4.20. The $\text{TE}_{011+\delta}$ is represented by two magnetic dipoles in axial orientation and exhibits a radiation quality of 780 for a permittivity of 50 and the given aspect ratio. Its radiation pattern shows two beams at $\theta = \pm 45^\circ$. The mode is therefore suitable for a tilted orientation between reader antenna and tag, as might be desired for example in applications where the reader antenna is mounted on the room or machine ceiling above the tag. The tilted orientation between reader and tag can reduce the room clutter significantly when primary clutter reflections from the environment are not mainly propagating back towards the reader.

The $\text{HEM}_{22\delta}$ mode is represented by four magnetic dipoles, and backscatters a main beam in broadside direction. It exhibits a radiation quality around 2000 for the given aspect ratio of $\rho_0/h = 0.67$ and $\epsilon_r = 50$.

The ceramic DR material is mounted on an alumina substrate with a gold metallized top side. The center area of the substrate carries an additional gold layer, that has been screen printed. This additional layer functions as a glue connection between DR and substrate. The setup has proofed mechanical and electrical stability in repeated heating cycles in temperatures from 20 °C to 900 °C. A photograph of the assembled tag is shown in Figure 4.21b.

4.3.2. Wireless High-Temperature Measurements

The sensing functionality of the chipless sensor is proofed in wireless measurements. Figure 4.21a shows the setup of the setup, in which the tag is placed inside a furnace. The reader consists of a VNA for transmit of the interrogation signal and reception of the backscatter. The VNA is therefore connected to a horn antenna, which is mounted 35 cm above the furnace, and 50 cm above the tag inside of it. The temperature is measured with a thermocouple inside the furnace. The control of the VNA, of the furnace as well as the processing of the backscatter signal (which includes the time-gating) is realized by a personal computer.

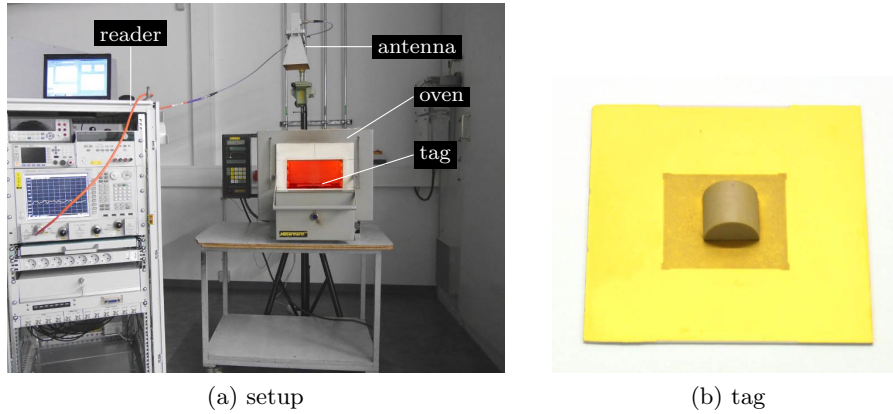


Figure 4.21.: a) Photograph of the wireless measurement setup. The furnace door is closed during the measurements. b) Photograph of the sensor tag.

Examples of the TD Rx signals of the setup are plotted in Figure 4.22. The figure shows the baseband envelope of the backscatter signal, when no tag is present, and when the tag is inside the furnace at 100 °C and 400 °C. One observes initial strong radar echoes of the interrogation signal at early time instants as well as the decaying resonance signal. The slope of the resonance decay increases from 100 °C to 400 °C, which indicates increasing material losses according to Equations (4.11) and (4.12).

The time-gating of the Rx signal cancels the main parts of the undesired clutter. The processed Rx signals show the desired resonance peak of the DR in FD. as shown in Figure 4.23a, the resonance peak shifts to higher frequencies for increasing temperature. In the range from 50 °C to 800 °C, the resonance frequency increases from 3.66 GHz by 182 MHz. This monotonous increase is plotted in Figure 4.23b. The resonance frequency tuning relates to a mean sensitivity of $\Delta f_r / \Delta \vartheta = 243 \text{ kHz/K}$. At room temperature, the sensitivity is slightly higher and equals 380 kHz/K. According to Equation (3.2), this sensitivity is equivalent to a temperature coefficient of 104 ppm/K.

For temperatures above 500 °C, a significant decrease of the power of the resonance peak is observed. This decreasing Rx power correlates to decreasing peak quality factors. The peak Q decreases from 1900 at 50 °C to 330 at 800 °C. The quality reduction is caused by increasing dielectric losses in the DR as noted in Figure 3.13c, as well as by increasing metallic losses in the ground layer.

Further analysis of the range and measurement accuracy of the DR sensor is found in Section 4.4. There, the sensor is tested in three different environments at room temperature and compared to the other chipless sensors of this thesis.

Discussion

The presented DR sensor proves the ability of chipless wireless sensing in temperatures ranges significantly above 175 °C. The approach allows for application in

4. Chipless Sensing Concepts

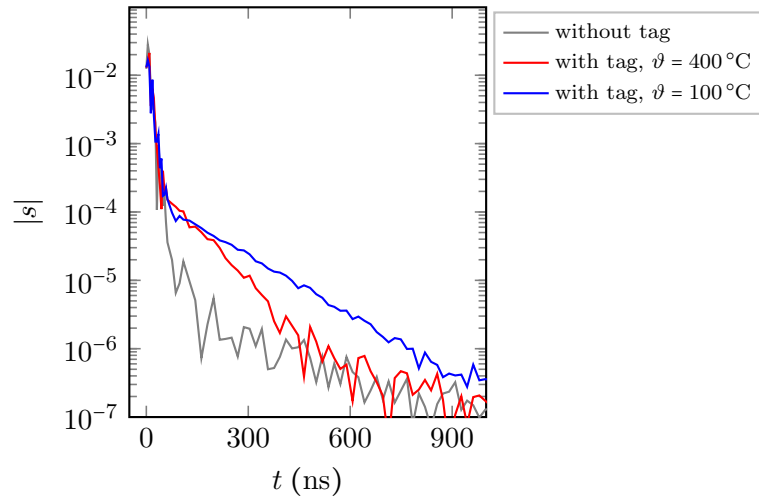


Figure 4.22.: Time domain Rx signal envelopes of the setup with and without the sensor tag.

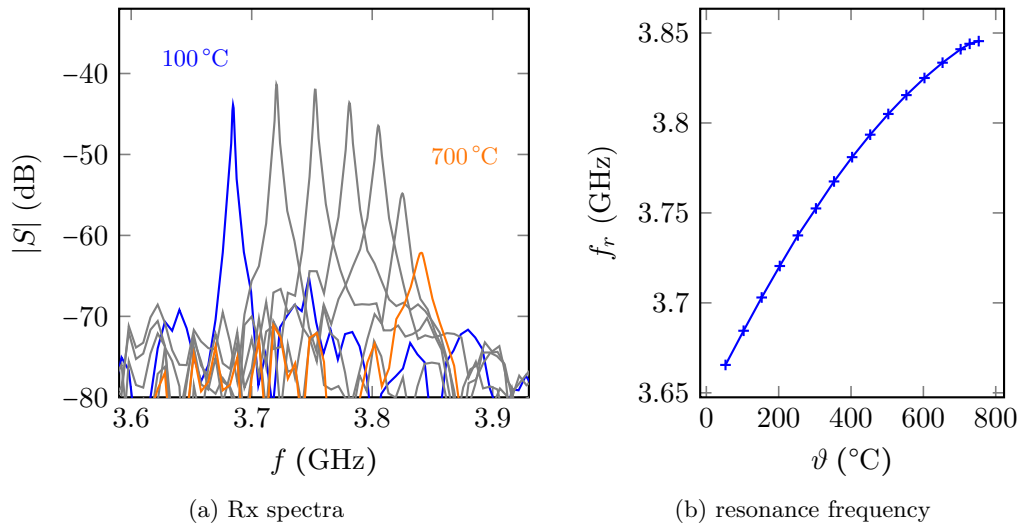


Figure 4.23.: Measured Rx signals in frequency domain and the resonance frequency in dependence of temperature.

4.3. The High-Q Resonator Concept

time-variant environments, where the tag and environmental objects are allowed to move. Furthermore, operation without an optical line-of-sight is demonstrated.

The developed sensor shows applicability in temperatures up to 800 °C. In temperature ranges above 800 °C the resonance Q and the SIR are too low to allow for a reliable detection in the given scenario. Herein, it is believed that the furnace cladding, i.e. the fire brick, impose additional RF propagation losses, which increase with increasing temperature.

An even higher operation temperature can be achieved by reducing the tag-to-reader distance, by weakening the environment clutter (i.e. by changing the environment), or by choosing a DR material with a smaller loss tangent at high temperature. Concerning the latter case, the choice of a material with a lower permittivity can decrease the high-temperature loss tangent, as indicated by the lower loss of alumina compared to K-50 in Section 3.2.3.

4.4. Comparison and Proof of Concepts

This thesis presents three conceptual approaches for chipless wireless temperature sensors. For each approach a sensor tag has been developed: (1) A sensor based on a dual-/cross-polarization concept, that has been presented in Section 4.1, subsequently called Crosspolar Sensor (XPS); (2) a sensor based on harmonic radar, represented by setup B of Section 4.2, subsequently called Harmonic Radar Sensor (HRS); and (3) a sensor based on a high- Q dielectric resonator that has been introduced in Section 4.3, subsequently named Dielectric Resonator Sensor (DRS). In the following, the wireless operation of these three sensors is demonstrated and performance aspects are compared. For these purposes, the three sensors are measured in three different environments, which include a nearly clutter-free anechoic chamber, and two indoor rooms. Setups and results are presented subsequently.

4.4.1. Test Scenarios and Measurement Setups

As mentioned, all three sensor tags are measured in three different environments, which are called scenarios I, II and III in the following. Each tag and its corresponding reader is setup inside each scenario. In each setup the tag-to-reader distance d has been varied from 0.25 m to 4.5 m, in 25 cm steps. This distance variation is undertaken in order to determine the reading ranges as well as to imitate a radial dynamic movement of the tag or reader. Herein, the clutter is unknown at all distances in all setups. This unknown clutter occurrence will hence verify the clutter suppression of each approach.

The tags have been measured solely at room temperature in all setups. The three environments differ significantly in their room constitution, leading to three significantly different clutter constitutions. This includes the clutter strength, time-decay and polarization:

- I) The first scenario is inside an anechoic chamber as pictured in Figure 4.24a. The tag is mounted on a styrofoam stand, which has a dielectric material permittivity close to 1. The reader antennas are mounted on tripods and connected to the VNA, that stands outside of the chamber. The styrofoam with the tag is moved in order to measure at varying distances. The anechoic setup is expected to show the weakest and fastest decaying clutter of all three scenarios.
- II) The second scenario is an indoor lab room, where the tag is mounted on a brick wall as shown in Figure 4.24b. A couple of metallic and dielectric objects such as gas pipes, lamps and tables are present. The room measures 8 m in length.
- III) The third scenario is an indoor lab room and shown in Figure 4.24c. The tag is mounted on a metal wall. Metallic ventilation pipes are mounted on the ceiling, metallic lab trolleys, metallic lab drawers and tables are present. The

room measures 13 m in length. This scenario is expected to cause the strongest and slowest decaying clutter signals among the three.

In scenarios II and III, the reader consists of a metallic lab trolley with the VNA inside of it and the reader antennas connected to it. The trolley is moved in order to measure at varying distances d , while the tag remained fixed at the walls.

In all three scenarios, the same VNA for signal Tx and Rx is used. Yet, the reader antenna configuration is different for each sensor tag. The crosspolar setup uses two equal horn antennas in orthogonal orientation, each with a gain of 13 dBi. The DR sensor uses only one of these horn antennas in copolar orientation to the tag. The harmonic radar setup uses one of the 13 dBi antennas for Tx of the fundamental and receives with a 15 dBi horn antenna at the harmonic frequency.

In all scenarios, the VNA has a Tx power of 10 dBm, uses an IF bandwidth of 1 kHz and is connected to the reader antennas with the same cables. This way nearly identical receiver noise levels are expected. Furthermore, 10 measurement sample signals are taken at each distance d , for each setup. For each of these received sample signals, the resonance frequency of the tag is determined by the reader. This determination will either detect the resonance peak (in case of the DR and harmonic radar sensors) or the resonance notch (in case of the crosspolar sensor) after processing the Rx signal. The difference between the true resonance frequency f_r of each tag at the given temperature and the measured/determined frequency position \bar{f}_r of each measurement sample signal is called resonance position error

$$\epsilon_f = f_r - \bar{f}_r. \quad (4.14)$$

This error is given in the following subsection for all scenarios. Due to the 10 sample repetitions, the position error can be evaluated with statistical means, resulting in a mean value and a standard deviation of ϵ_f . This way, both the impact of noise as well as the impact of the free-space propagation, including multipath or (de-)polarization effects, on the determination of the resonance position can be evaluated. Furthermore, the resonance position error is normalized to the sensor's absolute temperature sensitivity $s_\vartheta = \Delta f_r / \Delta \vartheta$, in order to describe the temperature detection inaccuracy

$$\epsilon_\vartheta = \frac{\epsilon_f}{s_\vartheta} \quad (4.15)$$

at a given distance.

The processing of the Rx signals by the reader includes time-gating for the crosspolar and DRS tags, and the determination of the resonance position for all tags. The time-gating is chosen under consideration of the time-spread of the tag signal and the time-spread of the clutter of each scenario. The crosspolar sensor has a fast-decaying signal in comparison to the high-Q resonance of the DRS. Hence, for the crosspolar setup a short time gate is used, that is meant to filter out the reader antenna coupling at early time instants and clutter signals at late time instants. For the DR sensor, a comparatively long time gate is used, that is meant to start after the clutter has decayed sufficiently. The harmonic radar signals are not time-gated.

4. Chipless Sensing Concepts

The resonance peak of the DRS and the harmonic radar setup, is identified as the absolute maximum of the (gated) Rx signal in FD. The resonance notch position of the crosspolar setup is identified as the deepest local minimum, between the absolute maximum of the Rx signal and its neighboring most significant local maximum in FD.

The achieved tag results are obtained without knowledge of the clutter, i.e., without including clutter reference measurements in the processing. All subsequently presented signal amplitudes and signal powers are given after normalization to the Tx amplitude, respective, Tx power.

4.4.2. Results and Discussion

First, note is taken of the clutter signals of the three scenarios. Figures 4.25a and 4.25b show the clutter signals of the three scenarios for the crosspolar and for the DR sensor setup in TD. The depicted baseband Rx signals s are normalied to the amplitude of the Tx signal. These signals have been obtained by calculating the IFFT of the FD Rx signals of the setups, when no tag is present. The plots show the clutter signals for a distance $d = 2$ m. Although, the clutter is principally different at each distance, these examples can represent qualitatively the clutter of other distances as well. The Rx signals show the received antenna mismatch (for the copolar DRS) or antenna coupling (for the crosspolar setup) in the first nanoseconds ($t < 20$ ns), and radar echoes from the environment, that arrive afterwards. It becomes clear that the clutter strength increases significantly from scenario I to scenario II and III, in both, the copolar and crosspolar setups. As an example, at 200 ns the received clutter signal of the crosspolar setup has reached the noise level with amplitudes below 1×10^{-7} in the anechoic chamber (scenario I). At the same time, scenarios II and III show roughly a factor 10 and 100 times higher amplitudes. In the copolar DRS setup, scenarios II and III show 100 and 700 times higher amplitudes than scenario I at the same time instant. As expected the room of scenario III with its many metallic surfaces, leads to the strongest clutter power. It shows the slowest clutter decay, due to its large size and the nearly lossless reflections at the metallic surfaces.

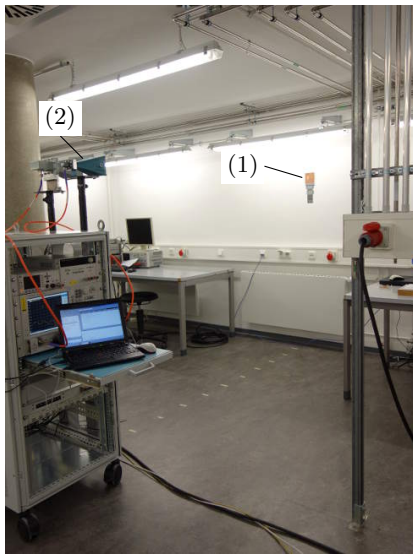
Furthermore, it is noted, that in the first 60 ns of the crosspolar setup, the Rx signals of scenarios II and III have comparable amplitudes, but are significantly weaker than in the corresponding copolar setups. On the contrary, at time instants > 200 ns, the difference between corresponding crosspolar and copolar setups is usually smaller than a decade. This underlines the occurrence of depolarization by multiple reflections as discussed in Section 4.1.1.

Based on these clutter observations, the time-gate of the DRS is taken from 100 ns to 800 ns in scenario I, from 150 ns to 800 ns in scenario II, and from 350 ns to 800 ns in scenario III. The time-gate of the crosspolar sensor, allows only for small adaptations to the environment, due to the comparatively short time-period of the tag signal. It is chosen from 20 ns to 60 ns in scenario I and III and from 25 ns to 60 ns in scenario II.

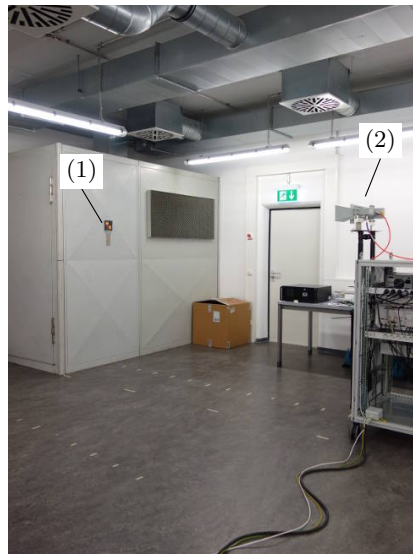
4.4. Comparison and Proof of Concepts



(a) scenario I



(b) scenario II



(c) scenario III

Figure 4.24.: Photos of the three scenarios with the sensor setups: (1) sensor tag, (2) antenna(s) of the reader.

4. Chipless Sensing Concepts

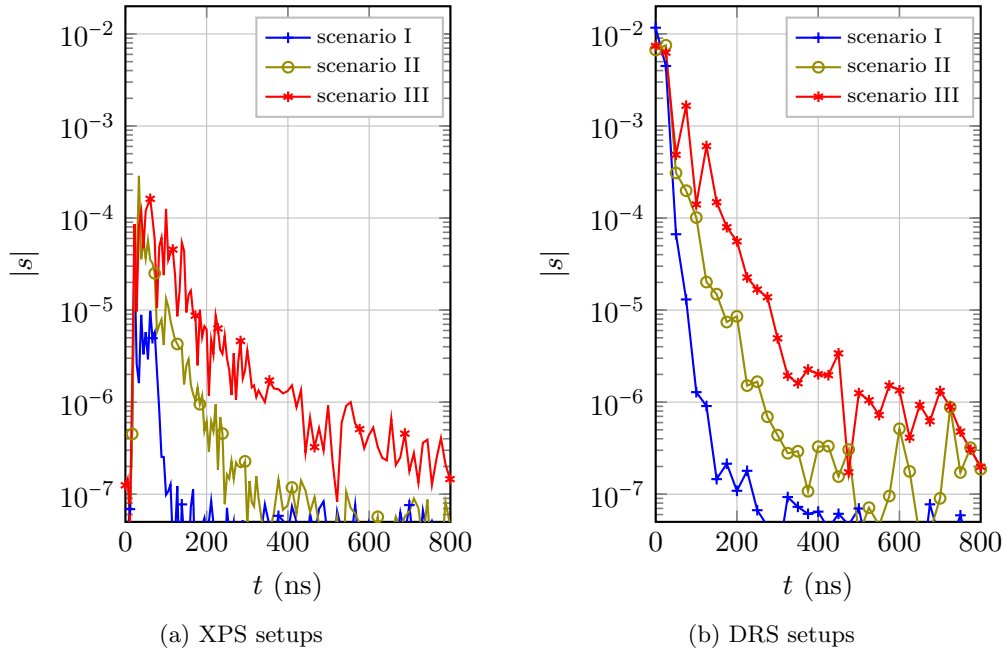


Figure 4.25.: Clutter signals in time domain.

Second, note is taken of a few examples of the Rx signals of the three tags. Figure 4.26 shows the processed tag signals of scenario I and III, the 'easiest' and 'most difficult' scenario. In the anechoic chamber the notch of the crosspolar tag at 2.925 GHz is easily recognized at 1 m and 3 m distance as shown in Fig. 4.26a. In scenario III, in contrast, the tag signal at 1 m distance is hardly distinguished from the clutter of the empty room and the tag notch is not detected properly (Fig. 4.26b).

Figures 4.26c and 4.26d show Rx signals of the harmonic radar setups in scenarios I and III. For 1 m and 3 m distance, the tag peak is recognized at 6.147 GHz. It becomes obvious, that shape and amplitude of the Rx signals, as well as the power of the noise floor, are nearly independent of the environment. Nevertheless, for 3 m distance in scenario III, a slight peak shift of 3 MHz is recognizable.

Figure 4.26e shows the Rx signal of the DR sensor for distances of 1 m and 3 m inside the anechoic chamber. The resonance peak is easily identified at 3.650 GHz. As mentioned above, in scenario III (see Figure 4.26f) the time-gate is chosen to start at a later time-instant in order to account for the increased clutter power. This reduces the power of the tag signal, but enables proper tag reading. The resonance peak at 1 m is only slightly interfered, with an SIR around 15 dB.

Third, the measurement accuracy is evaluated. Inaccuracies in the determination of the resonance peak or notch relate directly to inaccuracies of the temperature measurements. The resonance position error and the temperature detection error, according to Equations (4.14) and (4.15), are plotted in Figures 4.27 to 4.28, for all

4.4. Comparison and Proof of Concepts

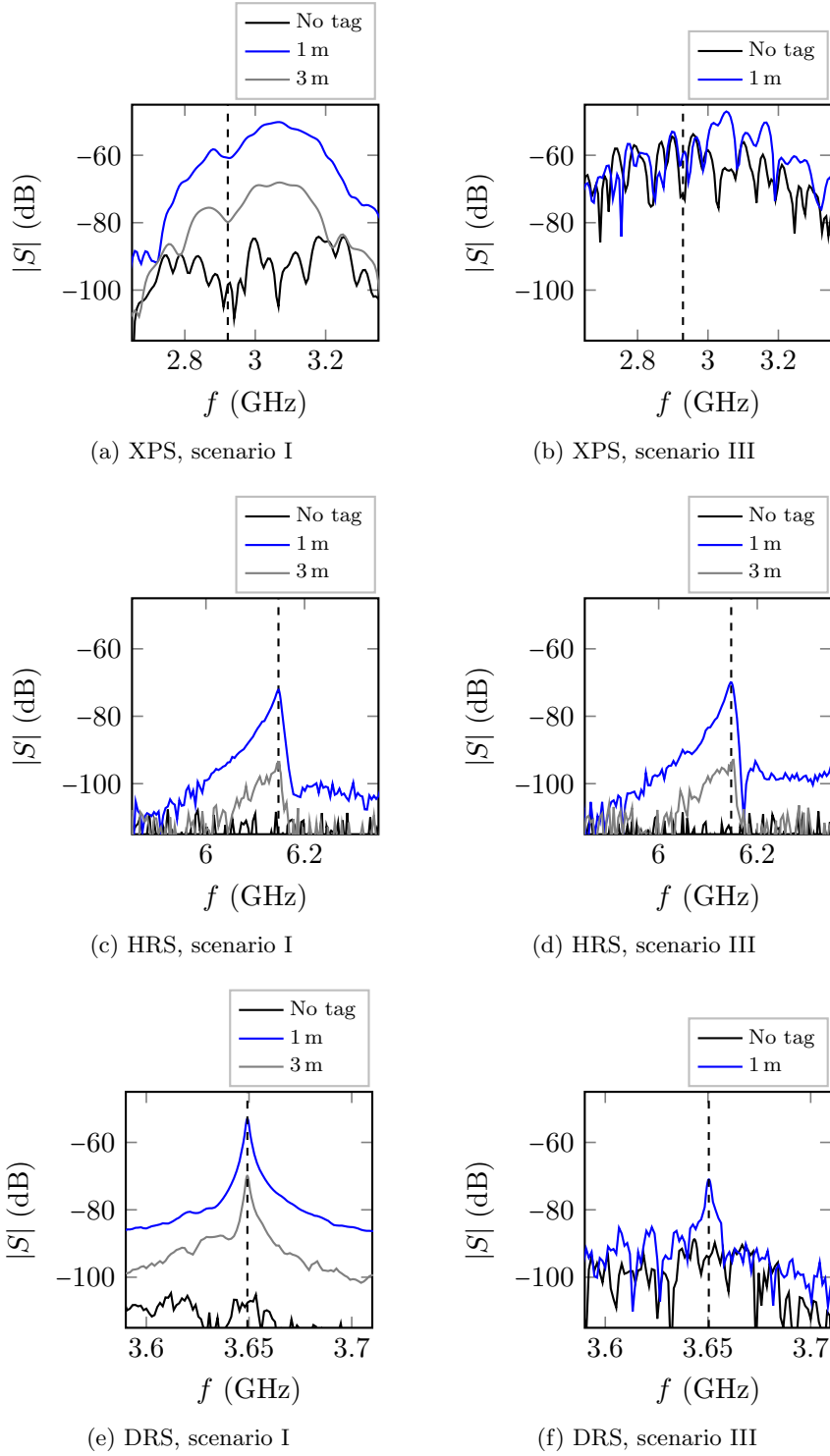


Figure 4.26.: Examples of Rx signals in frequency domain. XPS: crosspolar sensor; HRS: harmonic radar sensor; DRS: dielectric resonator sensor.

4. Chipless Sensing Concepts

three setups in all three scenarios. As mentioned above, here both the mean and standard deviations of the sample measurements at each distance are given.

Starting with the crosspolar setup in the anechoic chamber as plotted in Fig. 4.27a. It becomes obvious that receiver noise has only weak influence on the notch detection as indicated by a standard deviation smaller than 1 MHz for most distances up to 4.5 m. Yet, the mean values of the detected notch positions, show recognizable offsets up to 11 MHz, especially for distances larger than 1.5 m. These offsets relate to mean temperature detection errors up to 3.6 K, when assuming a sensor sensitivity of 3.1 MHz/K (compare Section 4.1.3). When moving to scenario II and III, it becomes obvious that the detection errors of the crosspolar tag increase significantly at distances larger than 1 m. As indicated in Figure 4.26b, the increased clutter power of these scenarios, make the crosspolar tag detection at larger distances practically impossible. Here, the read range of the tag is judged to be at 1 m in scenario II and 0.75 m in scenario III. This judgement is based on a maximally acceptable detection error of 6 K.

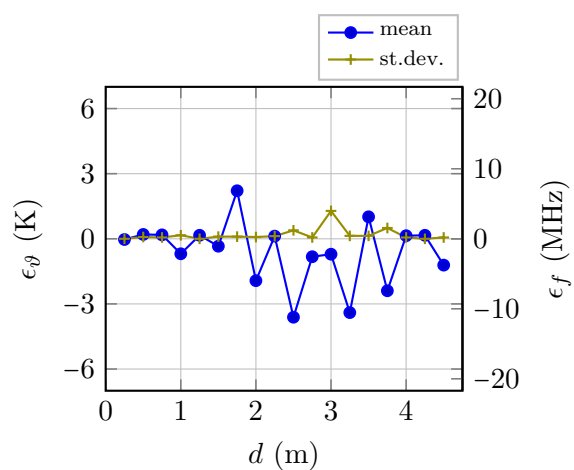
The results of the harmonic radar sensor are presented in Figure 4.28a to 4.28c for scenarios I to III. The sensor shows a range of 4 m in scenario I, and 3.25 m in scenarios II and III. Hence, the harmonic radar system shows the largest reading distance in the "most difficult" environment (scenario III). It becomes obvious that the range of this sensor is only weakly dependent on the environment as the reading is practically clutter-independent. Nevertheless, the harmonic radar sensor shows a recognizable impact of noise onto the peak determination, as it has the lowest Rx power in comparison. This circumstance is mainly caused by the harmonic conversion loss of the tag, which does not occur in the other concepts. The mean temperature measurement error is smaller than 1 K in scenario II and smaller than 3.5 K in scenario III for distances smaller than the named maximum range.

The DR sensor shows mean peak errors smaller than 0.26 MHz for distances up to 4.50 m in the anechoic chamber. Here, the deviations due to noise are nearly negligible and the mean temperature accuracy is better than 0.7 K (see Fig. 4.29a). In scenarios II and III the maximum reading range is observed at 3.50 m and 2.25 m. The peak is detected with an error smaller than 0.56 MHz or 1.5 K.

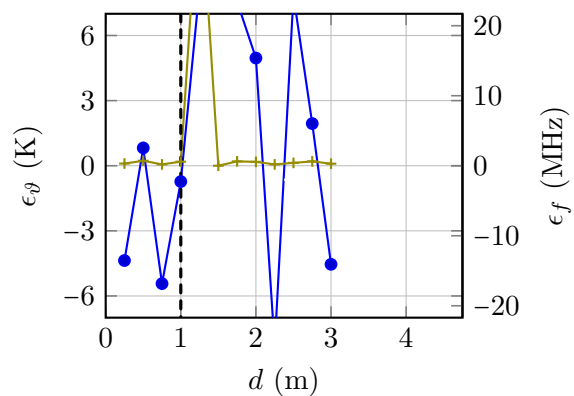
As a last step, the Rx power at the resonance position of each setup is plotted in Figure 4.30. The measured Rx power of the crosspolar setup in the anechoic chamber follows the description of a link budget calculation according to Equation (4.8) very well for distances between 0.5 m and 3 m. The DRS setup in scenario I is approximated by the radar equation (2.4) and is directly proportional to $1/d^4$. For the harmonic radar system of the anechoic chamber, the Rx power is approximated by Equation 4.10 under consideration of the input power dependent conversion loss. The power of scenarios II and III are partly showing significant deviations from the theoretical approximations. These deviations are discussed in the following subsection.

The maximum range and the maximum mean temperature detection inaccuracies of the setups for a distance of 1.5 m are summarized in Table 4.1.

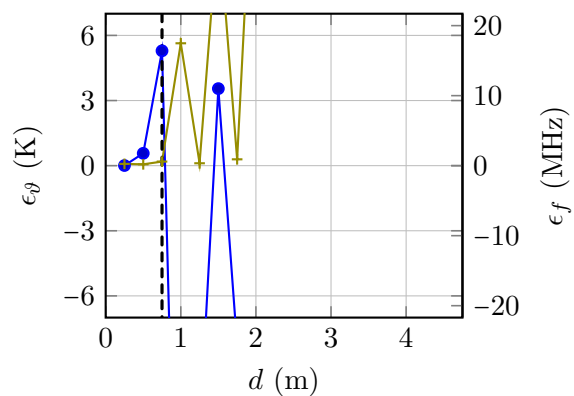
4.4. Comparison and Proof of Concepts



(a) scenario I



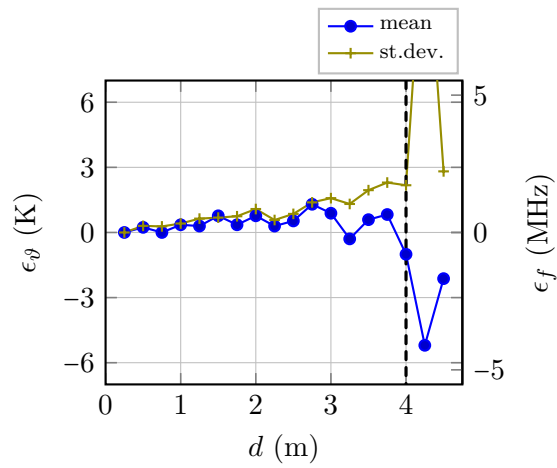
(b) scenario II



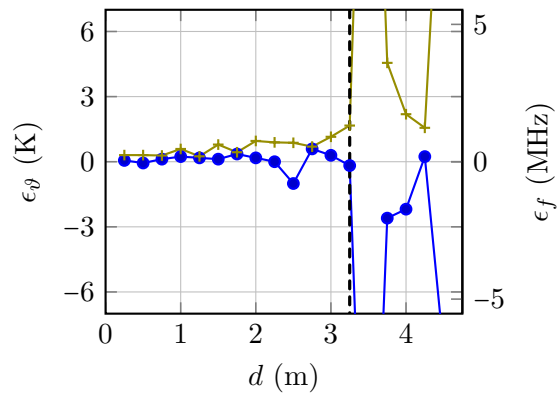
(c) scenario III

Figure 4.27.: Resonance position error of the crosspolar sensor (XPS) setup.

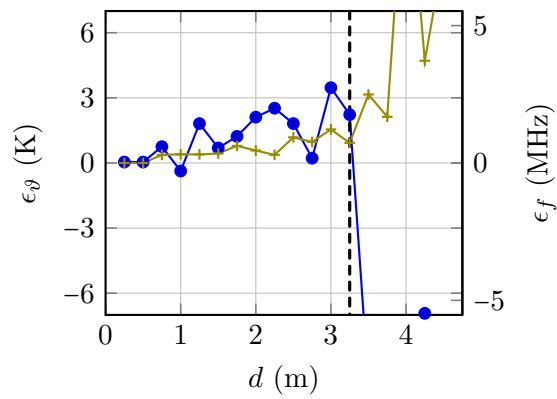
4. Chipless Sensing Concepts



(a) scenario I



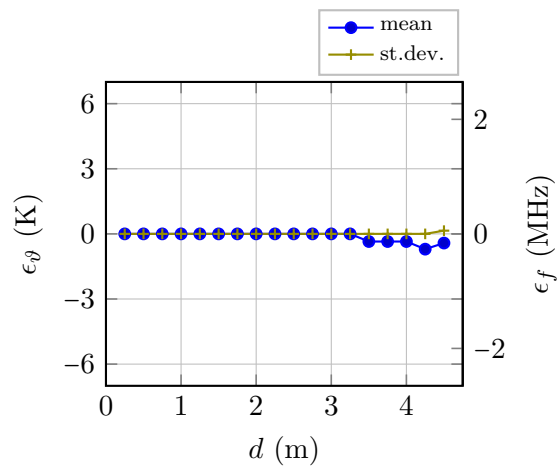
(b) scenario II



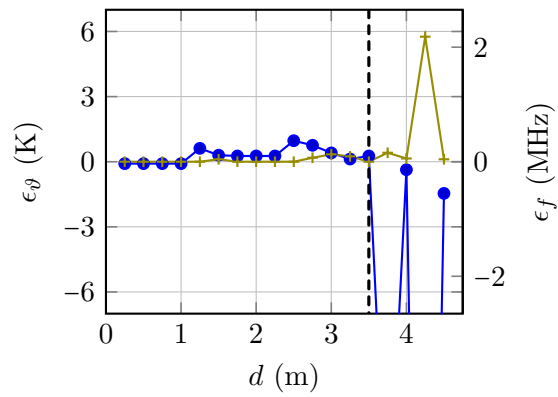
(c) scenario III

Figure 4.28.: Resonance position error of the harmonic radar sensor (HRS) setup.

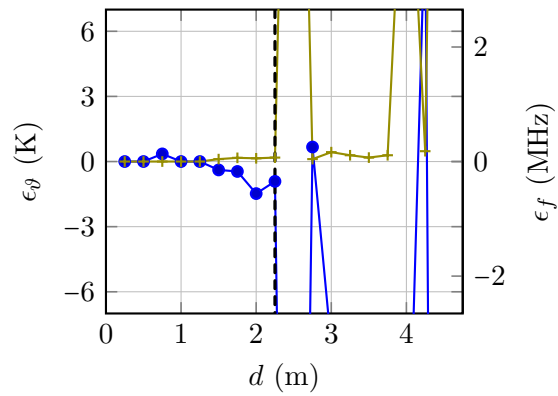
4.4. Comparison and Proof of Concepts



(a) scenario I



(b) scenario II



(c) scenario III

Figure 4.29.: Resonance position error of the dielectric resonator sensor (DRS) setup.

4. Chipless Sensing Concepts

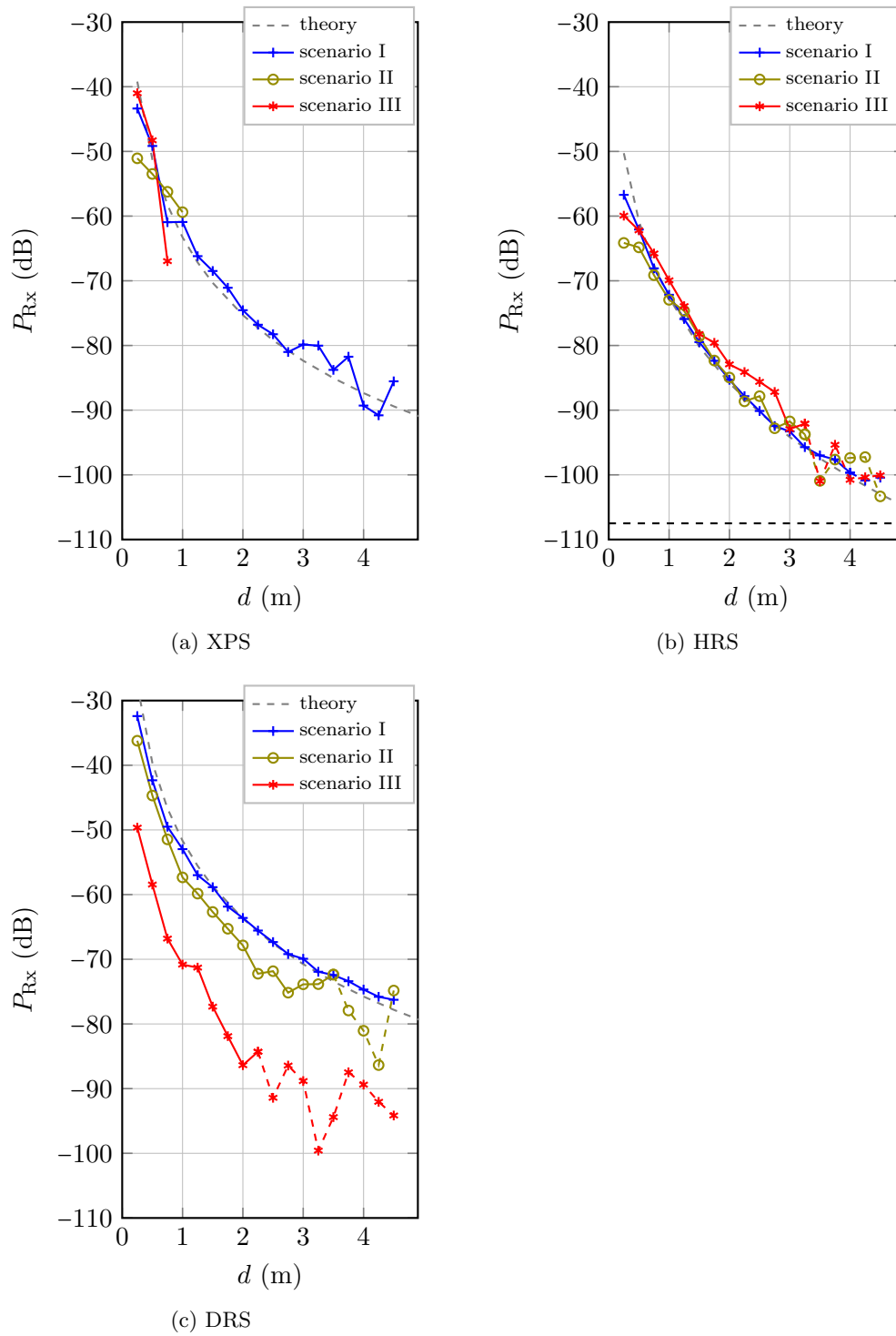


Figure 4.30.: Mean Rx power versus distance d . The dashed line extensions indicate a strong impact of clutter on the Rx power and therefore an erroneous detection.

Table 4.1.: Measured range and temperature inaccuracy error at 1.5 m distance of the three setups. XPS: crosspolar sensor; HRS: harmonic radar sensor; DRS: dielectric resonator sensor.

Setup		Scenario I	Scenario II	Scenario III
XPS	<i>range:</i>	> 4.5 m	1.0 m	0.75 m
	<i>error:</i>	0.7 K	(> 5.4 K)	(> 5.3 K)
HRS	<i>range:</i>	4.0 m	3.25 m	3.25 m
	<i>error:</i>	0.8 K	0.3 K	1.8 K
DRS	<i>range:</i>	> 4.5 m	3.5 m	2.25 m
	<i>error:</i>	< 0.4 K	0.6 K	0.4 K

Discussion

The description of the tags' Rx powers in Figure 4.30 indicate the occurrence of effects related to the free-space propagation.

For the crosspolar and DR setups in scenarios II and III increasing tag-to-reader distances lead to increasing free-space path losses. This decreases the Rx power of the tag to values similar or even smaller than the clutter power. This reduced SIR is indicated by sharp drops or rises of the Rx power at the resonance position. For distances larger than 1 m and 0.75 m in scenarios II and III of the crosspolar setup as well as for distances larger than 3.5 m and 2.25 m in scenarios II and III of the DR setup, the tag signals cannot be separated from the clutter. This coincides with increasing detection errors.

For the harmonic radar sensor, in contrast, the clutter power is negligible and the noise power is nearly independent of the scenario. Nevertheless, noteworthy deviations of the tag's Rx power from the linkbudget calculation and from the anechoic chamber measurement occur (see Figure 4.30b). For example in scenario III the Rx power drops by almost 9 dB when increasing the distance by only 7% from 3.25 to 3.5 m. This drop is unlikely caused by noise interference as the SNR at 3.25 m is still 20 dB. Instead, this and similar drops are most likely caused by multipath propagation effects, in the form of destructive self-interference. Especially scenario III inherits multiple propagation paths due to the metallic ventilation pipes mounted on the ceiling. These objects are stronger 'illuminated' by the radiation beams of reader and tag antennas at large distances.

In addition, a slight depolarization of the backscatter signal of the harmonic radar in scenario III is suspected. As mentioned in Section 4.2.1, the DRA backscatter antenna of the tag shows an undesired parasitic mode with a crosspolar radiation direction. This mode can lead to a shift of the resonance peak, when the free-space propagation has an impact on the polarization due to reflections. This is probably the reason of the larger measurement errors of scenario III, which increase roughly

4. Chipless Sensing Concepts

by a factor 2 compared to scenario I.

Another noteworthy aspect is the observation, that the detection of the crosspolar sensor in scenario II appears more difficult than in scenario III at 0.25 m distance. In fact, the former setup is the only one of all 9 setups with an unprecise detection at the shortest distance. This is most likely caused by a significant depolarized initial clutter reflection from the brick wall. The nearly planar metal wall of scenario III, in contrast, will likely cause a mainly copolar initial reflection, and only secondary reflections from the reader antennas, the reader trolley or other objects lead to crosspolar interference as discussed in Section 4.1.1.

As a summary, it is noted, that the DR sensor allows for the most precise temperature detection. Up to a range of 1 m, the temperature detection error of all DR setups is smaller than 0.35 K. This performance is reached due to the high Q factor of the DR resonance which equals 1780 at room temperature. This is a factor of 3.4 times larger than the Q factor of the harmonic radar tag, and about 35.6 times higher than the one of the crosspolar tag. It is noted, that the resonance position error ϵ_f scales with the resonance bandwidth of the tags. The average resonance position error of the setups of scenario III within the reading range of each tag, results to an error-to-bandwidth relation of roughly 20% for the three setups. A sharper peak is obviously less sensitive to noise and to multipath interferences.

Furthermore, it is mentioned, that an optimization of the time-gating of the crosspolar and DR setups can lead to slight increases of the reading accuracy, when the tag-to-reader distance is known. This can be an entry point for further optimizations, but limits a dynamic movement of tag or reader and is hence, not of special interest at this point.

5. Dynamic Clutter Estimation

In a classical wireless communication system, signals that carry information, are transmitted from a transmitter to a receiver station via a radio channel. The radio channel usually adds noise to the Tx signal and comprises multipath propagation. The latter effect leads to fading and in turn, to distortion of the Tx signal. In order to counteract these distortions and to reduce implicated transmission errors, Channel Estimation (CE) methods are used. Pilot-based channel estimation uses a priori known Tx symbols, that are transmitted from transmitter to receiver in order to estimate the channel's transfer function and to equalize the subsequently received signals, that carry unknown data symbols [Kam11]. In an Orthogonal Frequency-Division Multiplexing (OFDM)-system the time-frequency grid can be used to arrange a pattern of pilot and data symbols, where each pilot is spaced by a certain time- or frequency-distance to its pilot neighbours [Col+02].

Such established channel estimation methods gave inspiration to the subsequently presented method of radar clutter estimation in chipless systems. As explained in Section 2.3, clutter often presents the strongest limiting factor for chipless systems in harsh industrial environments. In order to counteract clutter interference, the method estimates clutter signals and yields an estimate of the non-interfered tag signal. For this estimation, two frequency bands are used that surround the tag resonance frequency range. These estimation bands might remind the reader of the pilots in an OFDM system. Hence, the proposed method could be called *channel estimation* as it estimates the *channel* of the tag-to-reader communication. Yet, in a stricter sense, the clutter interference is not directly equivalent to self-inflicted multipath-interference of a user signal¹ as clutter represents rather an additional signal. However, the reader will find both denotations, *channel estimation* and *clutter suppression*, throughout the chapter as they incorporate the two views.

The following sections take a closer look at the clutter-disturbed tag signal and at the estimation method as published in [Kub+13a] and [Kub+14a].

5.1. Clutter interference

In a wireless sensor scenario the sensor is usually placed on and surrounded by several objects as shown in Figure 5.1. A radar pulse, that is transmitted by the reader, excites the wanted tag backscatter signal as well as unwanted reflections from the objects, which are called clutter. The Rx signal at the reader is a superposition of all of these signals, leading to interference of wanted and unwanted components.

¹'Nutzsinal' in german

5. Dynamic Clutter Estimation

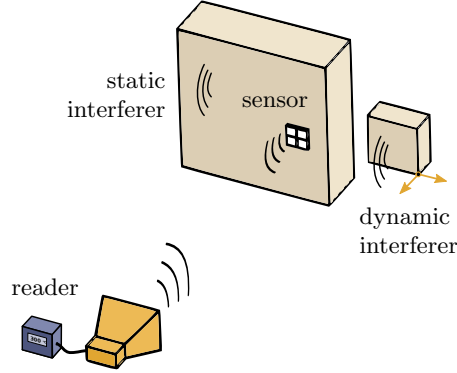


Figure 5.1.: Reading scenario with static and dynamic objects that cause clutter.

The objects of the environment can be divided into static objects, i.e., objects that do not move relative to the reader antenna and dynamic objects, i.e., objects that move, vibrate or rotate. Consequently, the clutter is composed of static and dynamic signals. From these two, the dynamic signals are in the focus of the estimation method and two assumptions are taken:

- static interference signals (including the static clutter, and potentially the static reader antenna mismatch) can be neglected as they are known from clutter reference measurements and pre-subtracted from following measurements. Usually, this reduces the power of the interference signals significantly.
- Doppler shifts due to the movement of the objects or of the tag can be neglected. This appears reasonable, as an object speed of less than $v_d = 100$ km/h will cause a frequency shift of less than $\Delta f_d = \frac{v_d}{c_0} f_0 = 280$ Hz, which is small compared to a resonance peak bandwidth in the MHz-range.

The interference power can be further reduced by time-gating of the Rx signal. This cancels unwanted signals that arrive either very early or very late compared to the tag signal. This may include reader antenna mismatch, reflections from objects far away from the reader or late echoes.

Using far-field approximation, the backscatter power, that is received by the reader antenna from an arbitrary object with a Radar Cross Section (RCS) at distance r is given by the radar equation (2.4). From this, the normalized Rx signal can be derived, whose magnitude relates proportional to the root of the RCS and which possesses a frequency-dependent phase. This Rx signal can either represent the wanted tag signal or an unwanted interference. If the tag's RCS is given by RCS_T and its Rx phase described by φ_T , then the tag signal is given by

$$S_T(f) = \sqrt{\text{RCS}_T(f)} \frac{A_R f}{\sqrt{4\pi c_0} r^2} e^{j\varphi_T(f)} \quad (5.1)$$

if the reader antenna is modeled as an aperture with gain $G = 4\pi A_R/\lambda^2$.

Unwanted signals, that originate from environment objects can be described in a similar fashion to (5.1). For a number of N_I objects the interference signal is given by the sum

$$S_I(f) = \sum_{i=1}^{N_I} \sqrt{\text{RCS}_{I_i}(f)} \frac{A_R f}{\sqrt{4\pi c_0 r^2}} e^{j\varphi_{I_i}(f)} = \sum_{i=1}^{N_I} A_{di} e^{j\varphi_{I_i}(f)} \quad (5.2)$$

in which cross-section RCS_{I_i} and phase φ_{I_i} are assigned to the i -th object. The resulting Rx amplitude A_{di} can be estimated for metallic objects according to equation (2.5), which describes the RCS of a flat metal surface with cross-sectional area for normal incidence. The interference signal magnitude of a plain metal block

$$A_{di} \propto A_M f^2 \quad (5.3)$$

is then proportional to its cross area A_M and increases quadratically with frequency. The total clutter interference signal of (5.2) will superimpose with the tag signal.

The clutter estimation method is designed for chipless tags, that encode information in the transmission peak of a resonance, denoted as frequency-position encoding in Section 2.2. The RCS of these tags varies strongly with frequency, and has a maximum at the resonance position. In TD the resonance is seen as a damped oscillation. The damping creates an exponential decay of the oscillation with time constant τ as shown in Figure 5.2a. The phase of the resonance signal in FD shows the typical 180° phase jump with a maximum slope equal to τ at resonance f_0 , as plotted in Figure 5.2b.

The amplitude of the clutter signal of a single metal block is, in comparison to the resonance, slowly varying in frequency. In TD, this interference is therefore represented by a short pulse, and approximated by a single dirac pulse. Multiple interferers are then given by a set of N_I dirac pulses, as shown in Figure 5.2a, where the i -th pulse has magnitude A_{di} and is located at time instant t_{di} . The time instant is used to describe the relative delay of the clutter pulse to the onset of the exponential decay of the tag resonance. In FD, the single dirac has a linear phase, whose slope is given by the pulse delay, $\varphi_{I_i} = -2\pi f t_{di}$. According to the Fourier-transform, the single dirac pulse will show a constant amplitude in FD which approximates the f^2 -increase in (5.3) in a narrow frequency range.

Yet, one or several *additional* dirac interferer will lead to a non-constant, rippled amplitude of the total interference signal in FD. For two pulses, the amplitude is nearly sinusoidal with ripple magnitude $\sqrt{2A_{d1}A_{d2}}$ and period $1/(t_{d2} - t_{d1})$. The oscillation period decreases with increasing time difference between the pulses. This amplitude-‘oscillation’ is analog to channel fading in wireless communications, where it motivates the use of channel estimation methods as mentioned in the previous introduction. The phase of the interference signal in FD is now rippled as well, and exemplarily plotted in Figure 5.2b. In relation to communication channels, the total time span T_M , measured from the resonance onset to the time instant of the last interferer (see Figure 5.2a) is called delay spread. It is the inverse of the coherence bandwidth

$$\text{BW}_c = 1/T_M, \quad (5.4)$$

5. Dynamic Clutter Estimation

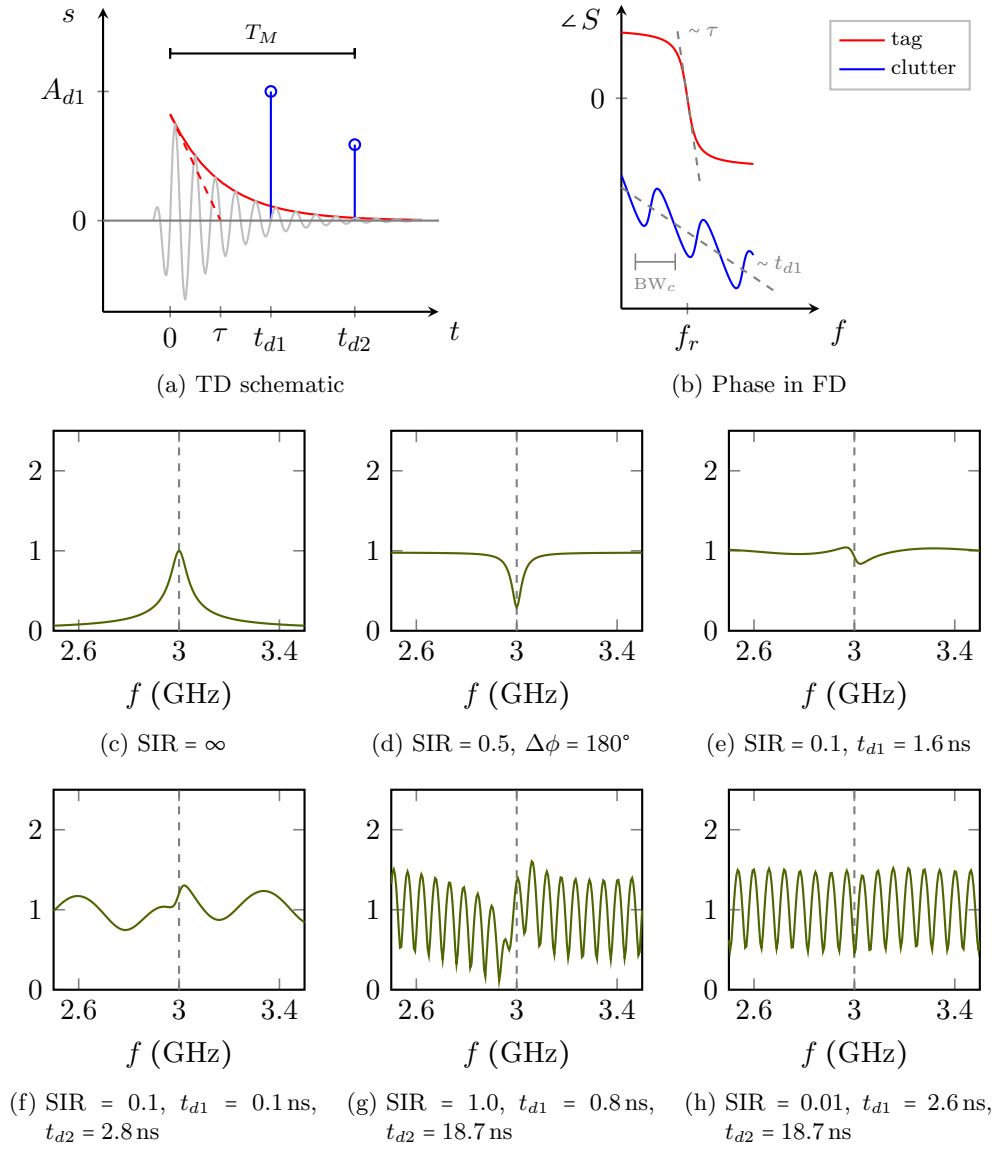


Figure 5.2.: Modeled interference of the tag signal with a clutter pulses: (a) tag resonance oscillation and dirac interference pulses in TD, (b) tag and interference signal in FD, (c) undisturbed tag Rx signal, (d) - (h) disturbed Rx signal for different constellations of SIR and t_{di} , for $N_I = 1$ and $N_I = 2$.

which is a measure for ‘how fast’ the channel changes along the frequency axis.

The wireless propagation leads to the superposition of interference and tag signal at the reader, which includes both, amplitude and phase of the two signals. The sum signal $S = S_T(f) + S_I(f)$ is exemplarily shown in Figures 5.2c to 5.2h for $N_I = 1$ and 2. Here, different constellations of Signal to Interference Power Ratio (SIR), according to (2.8), and interference pulse time delays are depicted. For $N_I = 1$, it becomes obvious that the initial resonance peak at f_0 can remain a maximum if tag and interference are in phase, it becomes a minimum for destructive superposition, $\varphi_T(f_0) - \varphi_I(f_0) = \pi$, or it can have any amplitude value in between for arbitrary phase constellations. For $N_I > 1$, additional local maxima appear from the channel fading. Consequently, one sees the resonance peak shifting, vanishing or drowning. As a consequence, the chipless sensing becomes erroneous or impossible. The severity of the disturbance increases with decreasing SIR and decreasing tag-to-interference phase slope relation $\frac{d\varphi_T}{df} / \frac{d\varphi_I}{df}$. The latter holds for the observation that high- Q resonances and short channel responses are beneficial for the chipless reading.

The following estimation method is based on the model of signal superposition and counteracts the peak disturbance in order to yield an improved detection of the resonance.

5.2. Estimation Method

The measured Rx signal \bar{S} at the reader is assumed to be the sum of the measured non-interfered tag signal \bar{S}_T and of the measured backscatter \bar{S}_I of the relevant dynamic interferers

$$\bar{S}(f) = \bar{S}_T(f) + \bar{S}_I(f). \quad (5.5)$$

Here, the measured tag and interference signals can be approximated by the theoretical expressions $S_T(f)$ and $S_I(f)$ in (5.1) and (5.2). The clutter estimation/CE method splits the received signal \bar{S} into three bands as depicted in Figure 5.3:

- The set of frequencies between $f_{1,2}$ and $f_{2,1}$ is called the tag backscatter band $B_0 = [f_{1,2}, f_{2,1}]$. In this frequency range, the tag resonance peak is expected to be found. The band carries both, the useful signal and the interfering signal

$$\bar{S}_{B,0}(f) = \bar{S}_T(f) + \bar{S}_I(f) \text{ for } f \in B_0 \quad (5.6)$$

as given by (5.5). Here, it is assumed that further coupling, beyond signal superposition, between tag and interfering object can be neglected.

- The estimation band $B_1 = [f_{1,1}, f_{1,2}]$ lies below the tag band and is spaced from the resonance range. It is assumed that the clutter signal is dominant and the magnitude of the resonance backscatter is negligible small

$$\bar{S}_{B,1}(f) \approx \bar{S}_I(f) \text{ for } f \in B_1. \quad (5.7)$$

Consequently, the band can be used to approximate the interference signal.

5. Dynamic Clutter Estimation

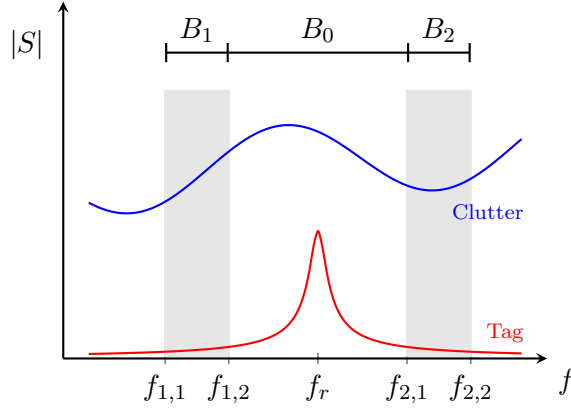


Figure 5.3.: Separation of the Rx signal into estimation bands B_1 and B_2 and the tag backscatter band B_0 .

- The upper estimation band $B_2 = [f_{2,1}, f_{2,2}]$ is an equivalent of the lower estimation band B_1 and lies above the resonance range. Here, the magnitude of the tag backscatter signal is usually negligible as well,

$$\bar{S}_{B,2}(f) \approx \bar{S}_I(f) \text{ for } f \in B_2 \quad (5.8)$$

and B_2 is also used to estimate the interference.

The splitting of the Rx signal allows a view onto spectral characteristics of the dynamic interference signal in a limited frequency range. This separation of the interference component is a key element of the presented method. The spectrum of the interference signal in the central tag backscatter band is estimated from spectral properties found in the outer estimation bands: Based on $\bar{S}_{B,1}$ and $\bar{S}_{B,2}$, an estimate \hat{S}_I of \bar{S}_I in B_0 is developed. The estimate is complex in order to include both magnitude and phase of the interference. In order to develop an adequate estimation, two basic cases are considered:

- in the first case, the width of the backscatter band B_0 is small compared to the coherence bandwidth, i.e., $f_{2,1} - f_{1,2} \ll \text{BW}_c$. Then the interference is a slowly varying signal in FD compared to the tag resonance peak and the peak shift. Linear interpolation of magnitude and phase of the interference signal across the tag backscatter range is sufficient. This leads to a minimal computational effort. The bandwidth of the estimation bands B_1 and B_2 can be chosen very small (in the range of a few kHz) as principally only two frequency support points are necessary.
- in the second case, the resonance peak is wide compared to the channel coherence bandwidth, $f_{2,1} - f_{1,2} > \text{BW}_c$. Then linear interpolation will usually be insufficient as the clutter variation versus frequency is fast. This case is

subject of the subsequently described ‘advanced interpolation’ approach and of the scenarios in the measurement section. In this case the width of the estimation bands should be chosen large (comparably wide as the width of B_0) in order to possess adequate detection sharpness. The difficulty of interpolating the clutter signal increases now with increasing delay spread T_M .

Following case b), first, \hat{S}_I is settled to approximate amplitude and phase of the lower and upper estimation band signals $\bar{S}_{B,1}$ and $\bar{S}_{B,2}$, as the approximations of (5.7) and (5.8) suggest. In order to describe the complex difference between estimation and measurement in these two bands, two estimation errors ϵ_1 and ϵ_2

$$\epsilon_1 = \int_{f_{1,1}}^{f_{1,2}} |\bar{S}_{B,1}(f) - \hat{S}_I(f)| df \quad (5.9)$$

$$\epsilon_2 = \int_{f_{2,1}}^{f_{2,2}} |\bar{S}_{B,2}(f) - \hat{S}_I(f)| df \quad (5.10)$$

are defined. The sum ϵ_t

$$\epsilon_t = \epsilon_1 + \epsilon_2 \rightarrow 0 \quad (5.11)$$

of these two errors is taken as an optimization criterion. It will be minimized by a suitable interference signal estimate. As described in the previous Section 5.1 clutter reflections from flat metal surfaces in the far-field can be approximated by short pulses in TD. The estimate \hat{S}_I of the unknown interference signal \bar{S}_I is consequently setup of N_I Dirac pulses

$$\hat{s}_I(t) = \sum_{i=1}^{N_I} (A_i e^{j\varphi_i} \delta(t - t_{di}) * g_i(t)), \quad (5.12)$$

each at time instant t_{di} , with relative phase φ_i and convoluted with the weighting function g_i . In FD, the diracs are represented as a sum of complex oscillations and the estimation signal is given by

$$\hat{S}_I(f) = \sum_{i=1}^{N_I} A_i e^{j(2\pi f t_{di} - \varphi_i)} G_i(f). \quad (5.13)$$

Each oscillation is multiplied with the Fourier-transformation of the weighting function $G_i(f) = \mathcal{F}(g_i(t))$. This frequency-dependent weighting is applied primarily due to the observation in Equation 5.3, which sees an increasing Rx power of a metal block’s backscatter signal versus frequency, when using aperture antennas. This behavior is imitated by the weighting

$$G_i(f) = (f - f_{1,1}) \alpha_i + 1 \quad (5.14)$$

with linear slope α_i .

The interference pulse approach leads to four unknowns for each Dirac pulse in \hat{S}_I : magnitude A_i , time instant t_{di} , phase φ_i and slope α_i . Consequently, a set of N_I pulses leads to a total number of $4N_I$ unknowns, which are to be found with

5. Dynamic Clutter Estimation

a suitable optimization method. Here, a sequential optimization algorithm is used to satisfy the criterion of (5.11). It is described in Section 5.2 and delivers the estimation signal \hat{S}_I . The desired tag signal S_T is afterwards estimated as \hat{S}_T

$$\hat{S}_T(f) = \bar{S}(f) - \hat{S}_I(f) \quad (5.15)$$

by subtracting the interference signal estimate \hat{S}_I from the measured Rx signal.

In order to evaluate the quality of the clutter estimation and suppression, the detection of the tag's resonance peak position is the most important indicator. The true resonance position at f_r , is estimated as the frequency \hat{f}_r which shows the largest magnitude in the estimated tag signal $\hat{S}_T(f)$ in B_0 . The true resonance position f_r is determined by measuring the tag without interference. The difference between estimated and true resonance position

$$\begin{aligned} \epsilon_{f_r} &= f_r - \hat{f}_r \\ &= f(\max |\bar{S}_T(f)|) - f(\max |\hat{S}_T(f)|), \quad f \in B_0 \end{aligned} \quad (5.16)$$

is called resonance position error ϵ_{f_r} . It is strongly linked to the accuracy of the crucial estimation of the phase of the interference signal. The phase estimation error

$$\epsilon_\varphi = \bar{\varphi} - \hat{\varphi} = \angle \bar{S}(f) - \angle \hat{S}_I(f) \quad (5.17)$$

in the second place and the resonance position error in the first place are taken to judge the estimation quality in the reading scenarios of the following measurement section 5.3.

Sequential Optimization of the Estimate

As described above, the goal of the channel estimation method is to find an adequate mathematical description of the interference signal. The taken approach to reach this goal is the summation of N_I time-shifted Dirac pulses. As (5.13) indicates, this approach leads to $4N_I$ unknowns in order to describe magnitude, time instant, phase and slope of each pulse. This leads to an optimization problem, that allows for different solutions. In this work, the problem is solved by a sequential routine with N_I sequences.

In each sequence i of N_I , an initial estimate of the four unknowns is found by calculating the FFT of the Rx signal in the estimation bands $\bar{S}_{B,1}$ and $\bar{S}_{B,2}$. Here, the relevant interference pulse should be seen as a peak in the spectrum. The peak amplitude and time instant is optimized to fulfill the criterion in (5.11) using (5.13) with $N_I = 1$. This leads to an intermediate estimate of S_I , which is subsequently subtracted from the measured Rx signal \bar{S} . Afterwards the $(i + 1)$ -th sequence is started, which takes the rest of the latter subtraction as its starting point. Finally, the complete estimate \hat{S}_I is the summation of all Diracs as found in the sequences as given by (5.13).

The sequential estimation is used mainly in order to reduce the computational complexity. Instead of solving a joint $4N_I$ -dimensional criterion, N_I statements with 4 unknowns are solved.

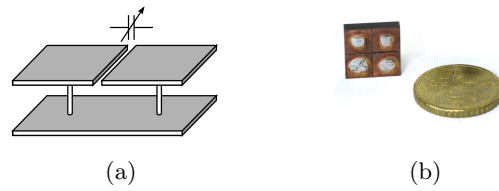


Figure 5.4.: The strain sensor from [MSJ11]: (a) mushroom structure with gap capacity, (b) photograph. © 2011 IEEE

5.3. Measurements

Wireless measurements have been performed to prove the presented clutter interference method. Details on the measurement setup and results are found in the following sections. During these measurements, two different chipless sensor tags have been used.

The first tag is the DR temperature sensor of Section 4.3.1. It consists of a ceramic resonator mounted on a ground sheet. The temperature-dependence of the ceramic's permittivity leads to a temperature-dependence of the tag's resonance frequency and hence, allows for a remote temperature measurement. In this setup the dielectric $TE_{011+\delta}$ -mode is used (compare Section 4.3.1).

The second tag is a strain sensor, that has been presented in [MSJ11]. It is setup as a composite right-/left-handed microstrip antenna. The antenna is formed by two mushroom elements and measures $1.5 \times 1.5 \text{ cm}^2$ as shown in Figures 5.4a and 5.4b. The mushroom elements are spaced by a gap, that is mechanically loaded by applied strain tension. The resulting mechanical deformation of the gap width between $250 \mu\text{m}$ and $600 \mu\text{m}$ shifts the antenna resonance from 3.05 GHz to 3.2 GHz . This tuning is detected by the reader who concludes the measured strain value from the resonance position.

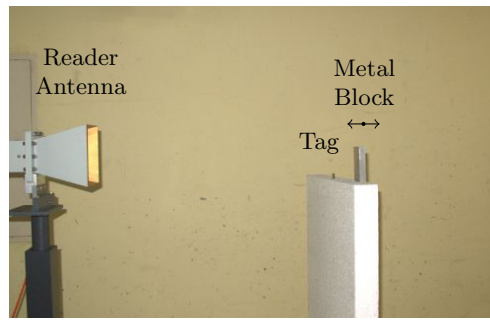
The two different tags use very similar principles for the chipless sensing: they both use frequency-position encoding of the measurement value, they both operate close to 3 GHz and they are both electrically small. Yet, the tags have significantly different resonance bandwidths: the strain sensor shows resonance quality factors of 50, the DR temperature sensor of 550, a factor 11 times higher. The impact of this bandwidth difference will be discussed.

In order to create an interference scenario, the tags are placed next to a metal block. This block causes the interference signal, and it will be placed at different locations in order to imitate a dynamic movement.

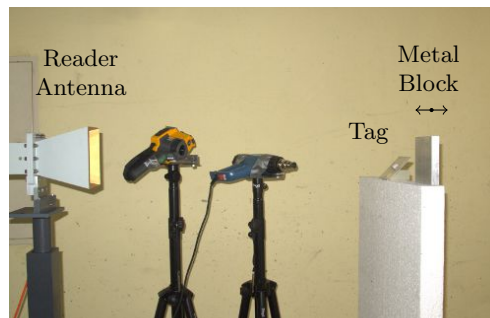
5.3.1. Measurement Setups

Two similar reading scenarios are analyzed. The first scenario with the temperature sensor and the second with the strain sensor. In both cases, the measurements are conducted in the same indoor room. The sensor tag and the metal block interferer

5. Dynamic Clutter Estimation



(a) Strain tag



(b) Temperature tag

Figure 5.5.: Photographs of the two measurement setups. © Cambridge University Press, reproduced with permission, [Kub+14a] refers.

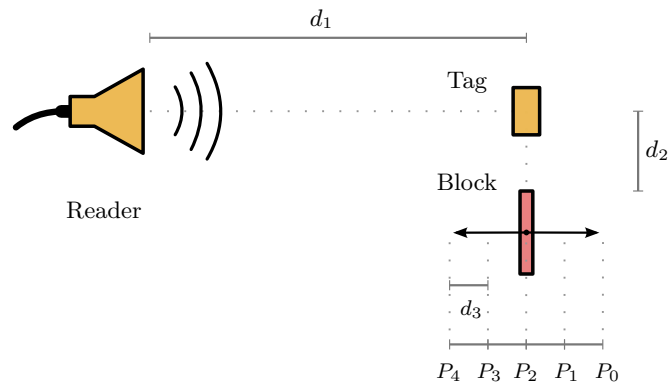


Figure 5.6.: Top view of the placement of reader antenna, sensor tag and metal block during the measurements.

are placed on a stand, facing the reader antenna at distance d_1 . The reader horn antenna is connected to a vector network analyzer, that transmits the interrogation signal and receives the backscatter. The setups are shown in Figures 5.5a and 5.5b. In the scenario of the temperature sensor, a heat gun and an infra-red camera are used to control the temperature of the tag.

The distance d_1 between tag and horn antenna has been 85 cm in the temperature scenario and 60 cm in the strain scenario. These slightly different distances have been chosen in order to have identical tag Rx powers, as the DR temperature sensor has a slightly higher peak RCS.

The metal block, which causes the dynamic interference, has a cross-section of $10 \times 12 \text{ cm}^2$ (40 times the area of the DR) in the first scenario and $4.5 \times 9 \text{ cm}^2$ (18 times the area of the strain tag) in the second. These metal block sizes have been selected in order to achieve comparable SIR power relations in both scenarios.

In both scenarios, the block is placed at a distance $d_2 = 10 \text{ cm}$ next to the corresponding tag as shown in Figure 5.6. From this point the block is moved stepwise in radial direction to five different positions in order to imitate a dynamic movement of the interferer. Each of these five positions is spaced by $d_3 = 1 \text{ cm}$ to its neighbor position and named P_i with $i = 1, \dots, 5$. At the center operation frequency of 3 GHz, each 1 cm step equals a phase shift of 72° of the interference signal relative to the tag signal. Hence, the five steps comprise a total 360° phase shift with constructive, destructive and intermediate superposition.

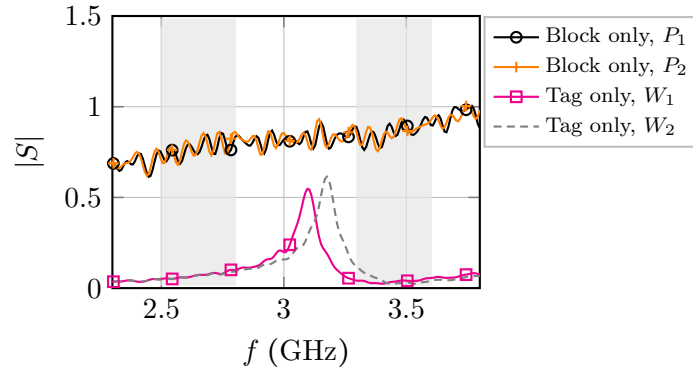
According to the consideration of Section 5.1, static clutter signals of the measurement environment are subtracted under support of a reference measurement and time-gating. This way the channel estimation focuses on the variant interference parts which are caused by the metal block. The subsequently presented Rx and estimation signals (Figures 5.7 and 5.8) are consequently given after this pre-processing and are normalized to $\frac{1}{100}$ of the Tx signal amplitude.

For each scenario, i.e. for each sensor tag, two different measurement values are evaluated. These measurement values, i.e. resonance positions, have been chosen for a comparable relation between resonance shift and peak bandwidth $\frac{\Delta f_0}{BW_p} = 1.2$ in both scenarios. The temperature in the first scenario is set to $\vartheta_1 = 20^\circ\text{C}$ and $\vartheta_2 = 35^\circ\text{C}$, leading to DR resonances at 2.914 GHz and 2.920 GHz. The gap of the strain sensor is mechanically set to $W_1 = 345 \mu\text{m}$ and $W_2 = 535 \mu\text{m}$ corresponding to sensor resonances at 3.100 GHz and 3.176 GHz.

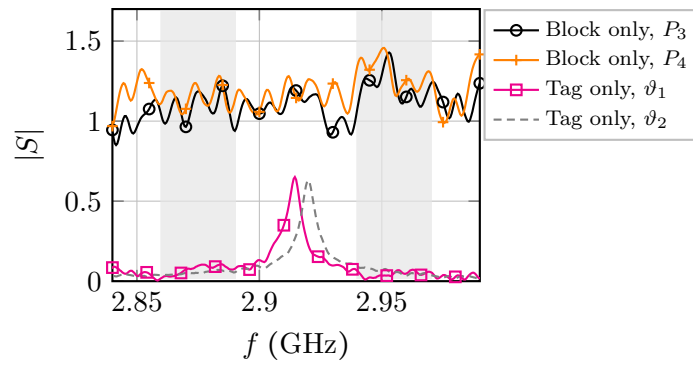
Consequently, there are ten combinations of resonance and block position per scenario. The estimation method has been applied to all of these combinations.

It is noted, that the calculation of the interference estimate has been performed in post-processing steps after the measurement on a standard office computer. Each estimation required about 0.6s computation time. In an application, this allows for real-time processing of the algorithm with update rates in the lower Hertz range.

5. Dynamic Clutter Estimation



(a) Strain tag



(b) Temperature tag

Figure 5.7.: Measurements of the sensor tags (without metal block) and of the metal blocks (without sensor tags). (a) Strain tag with gap widths W_1 and W_2 and metal block at positions P_1 and P_2 . (b) Temperature tag at temperatures ϑ_1 and ϑ_2 and the metal block at positions P_3 and P_4 . The two estimation bands are marked grey shaded.

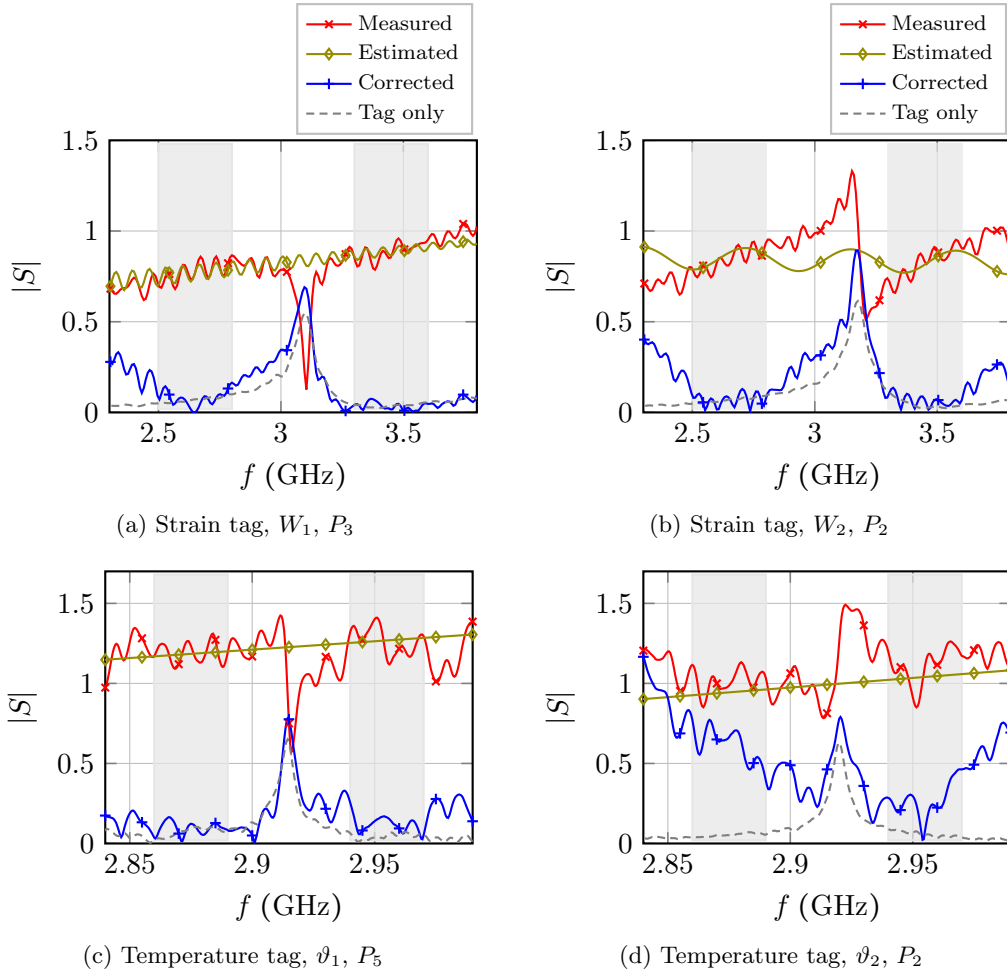


Figure 5.8.: Four example results of the clutter suppression method with measured, estimated, corrected and tag only Rx signals. The two estimation bands are marked grey shaded. The legend applies to all sub-figure. For the strain tag with gap W_i and block position P_i in (a) and (b), for the temperature tag with temperature ϑ_i and block position P_i in (c) and (d).

5. Dynamic Clutter Estimation

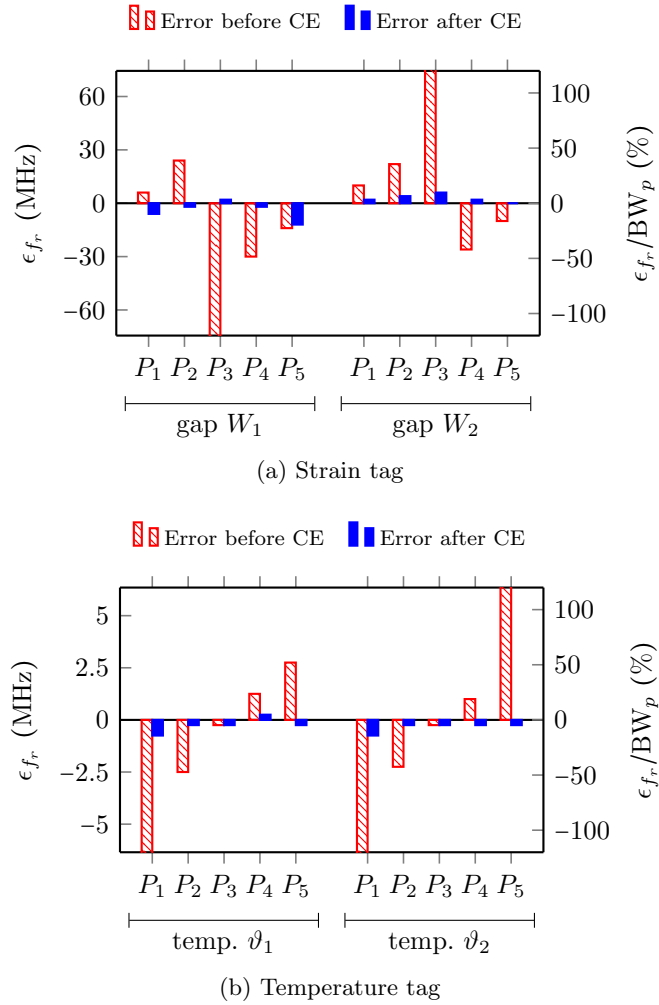


Figure 5.9.: Resonance position error, according to (5.16), before and after application of the clutter estimation method (CE); the error is given in MHz and relative to the peak bandwidth.

5.3.2. Measurement Results

First, note is taken of the isolated backscatter signals of the tag (without interferer) \overline{S}_T and of the metal block (without tag) \overline{S}_I .

Figure 5.7b shows the Rx signal of the DR tag for ϑ_1 and ϑ_2 with its resonance peaks at 2.914 GHz and 2.920 GHz, and peak amplitudes of 0.64. The plot also shows the backscatter response of the metal block alone, at position P_3 and P_4 , as representatives of all five block positions. The block signal has a rippled course with mean amplitude of 1.17, resulting in an SIR of 0.3.

Figure 5.7a shows the Rx signal of the isolated strain sensor. The resonances are easily identified for gap widths W_1 and W_2 . The Figure also includes two isolated signals of the corresponding metal block. Its rippled magnitude increases with frequency as (5.3) suggests. A comparison between the two block signals indicates a very similar shape, as well as a pulse delay offset according to the spacing d_3 , recognized in the frequency shift of the ripples. The SIR is equal to 0.5.

Second, note is taken of the disturbed Rx signal \overline{S} , with both, tag and interference components. The disturbed Rx signal is plotted in Figures 5.8c and 5.8d for two examples of the temperature tag scenario; and in Figures 5.8a and 5.8b for two examples of the strain sensor scenario. In all of these cases the tag resonance cannot be clearly identified anymore. The tag signal is significantly disturbed. In the cases of Figures 5.8c and 5.8a, the disturbance leads to a local amplitude decrease, or minimum in the resonance peak range. In the cases of Figures 5.8d and 5.8b, the disturbance has created signal amplitude increases, distorted local maxima, around the peak position. These depicted examples show consequently destructive and constructive interferences cases. It is noted, that in all cases, the new minima and maxima positions are in the proximity, but not identical to the true resonance positions.

Third, the channel estimation method is applied to the disturbed Rx signals. For the temperature scenario, $N_I = 1$ Dirac pulse has been taken to approximate the clutter. The estimation bands are chosen in the ranges $B_1 = [2.86 \text{ GHz}, 2.89 \text{ GHz}]$ and $B_2 = [2.94 \text{ GHz}, 2.97 \text{ GHz}]$. For the strain sensor scenario, $N_I = 2$ Dirac pulses have been taken to approximate the interference within $B_1 = [2.5 \text{ GHz}, 2.8 \text{ GHz}]$ and $B_2 = [3.3 \text{ GHz}, 3.6 \text{ GHz}]$. With these settings the estimation algorithm has been applied to estimate the interference signal and to subtract it from the Rx signal. This yields the estimations of the tag signals as shown in Figures 5.8c to 5.8b. Inside the central backscatter band B_0 , the tag estimates show good agreement to the non-interfered tag signals in the cases of Figures 5.8c, 5.8a and 5.8a; and acceptable agreement in the case of Figure 5.8d. The resonance peaks are reconstructed. Although, amplitude and ripple differences are visible between original and estimation (especially in the latter case), the decisive peak positions are found with satisfying accuracy in all four cases. In these examples, the offset ϵ_{f_r} between true and estimated peak frequency, according to Equation (5.16), is equal to -0.25 MHz in both temperature measurement examples and equal to 2.0 MHz and 4.0 MHz in the strain measurement examples.

Subsequently, a comment on the phase estimation shall be noted. Due to the 11

5. Dynamic Clutter Estimation

times larger bandwidth of the strain resonator, the strain scenario copes with a significantly larger phase difference of the interference signal across the backscatter band B_0 . This makes the phase estimation of the strain scenario potentially more difficult and error-prone. Yet, this difficulty is counteracted with a larger bandwidth of the estimation bands B_1 and B_2 in this scenario and the phase estimation error, according to Equation (5.17), is smaller than $\pm 20^\circ$ within B_1 and B_2 in all four examples.

Finally, the results of all ten combinations of block position P_i and sensor resonance of both scenarios are listed in Figure 5.9. Without application of the estimation method, the search for a resonance peak in B_0 is as difficult as expected from the theoretical considerations in Section 5.1. Although, for a few constructive interference cases with $\varphi_T - \varphi_I \approx 0^\circ$, an acceptable determination of the peak resonance is possible despite the interference, most un-corrected Rx signals show large resonance detection errors. After application of the channel estimation algorithm, the tag resonance shapes are reconstructed, or at least well approximated, in all cases. The resonance position is found within significantly smaller error intervals after application of the clutter suppression. For the temperature sensor scenario, the resonance position error ϵ_{f_r} lies in the interval -15.5 to $+8.0$ MHz when no clutter estimation is applied. This error interval is reduced to -0.75 to $+0.25$ MHz when applying the proposed method. For the strain sensor scenario, the clutter interference leads to resonance detection errors within $[-102, +90]$ MHz without countermeasures. Application of the method reduces the error to $[-12, +6]$ MHz. Consequently, the resonance position error is reduced by a factor of 20 in the first scenario, and by a factor of 10 in the second.

Discussion

The channel estimation method, as proposed in this chapter, has proven to enable detection of clutter-interfered tag resonances. The impact of a dynamically placed metal block is strongly reduced in both chipless scenarios.

For the temperature sensor, the average resonance estimation error is 0.35 MHz which is equivalent to a temperature measurement uncertainty of 1.2 K, as the sensor sensitivity is given by 0.3 kHz/K (compare Section 4.3.1 and [Kub+13b]). In the second scenario, the average resonance estimation error is 3.8 MHz, which correlates to a strain measurement uncertainty of 16.6×10^3 ppm, when assuming a strain sensitivity of 228 Hz/ppm [MSJ11].

It is evident, that the temperature scenario yields 10.8 times smaller absolute measurement errors, despite having nearly the same operation frequency and a slightly smaller SIR. On the contrary, the temperature sensor has an 11 times higher resonance Q . This leads to the conclusion, that the resonance position estimation error does scale with the peak bandwidth. In fact, Figure 5.9 shows very similar error-to-bandwidth relations ϵ_{f_r}/BW_p of the two scenarios. Higher resonance Q -factors leads consequently to a more robust detection in absolute terms.

Aside, it is expected that the estimation errors will increase for decreasing SIR

and for decreasing coherence bandwidth. A large time-spread of strong clutter pulses leads to a fast-varying interference signal in FD and very difficult tag detection. In such cases the proposed estimation method could work together with clutter suppression by crosspolar, or high- Q time-gated approaches, such as presented in Chapters 4.1 and 4.3.

6. Conclusion and Outlook

Wireless sensors are used in numerous application fields to monitor and control various processes and physical states. Commercially available wireless sensors at the current state-of-the-art can support the majority of these tasks, but reach their limits in certain specific applications. Some of these specific applications are found in harsh environments, e.g., at high temperatures. Here, disadvantageous limitations of available sensors include the maximum operating temperature, the requirement of an optical line-of-sight, and/or the sensor durability. As an example, a usual silicon chip-based wireless sensor is limited to temperatures below 175 °C. This thesis has investigated chipless wireless sensors to exceed or overcome these limitations.

A chipless sensor is based on passive RF backscatter mechanisms. The sensor is setup as an entirely electromagnetic circuit and avoids the usage of semiconductor ICs. Due to this avoidance and due to propagation and penetration properties of RF signals, a chipless sensor can enable operation in temperatures significantly beyond 175 °C and does not require an optical line-of-sight. Conceptual and design challenges concerning the operation of chipless sensors have been analysed in the thesis. The challenges mainly include (1) the occurrence of interfering time-variant radar clutter in relation to wireless communication aspects and (2) the choice and design of suitable measurement transducers in relation to high temperature. Referring to the first challenge, three general chipless sensor concepts as well as a chipless channel estimation method have been introduced, realized and validated. The concept realizations focus on temperature sensing, but are generally suitable for the sensing of other physical quantities as well. Main findings of the approaches are summarized subsequently. Referring to the second challenge, measurand-sensitive dielectrics are used as transducer materials in order to serve the chipless concepts in a favorably way. A microwave high-temperature dielectric material characterization method has therefore been developed and presented.

A concluding look is taken at the characterization method. It is based on resonances of a free Dielectric Resonator (DR) as it takes advantage of its high field concentration inside the dielectric and its comparatively slow resonance decay when a suitable mode is chosen. Field and radiation characteristics of DR resonances have prior been analysed and reveal the suitability of higher order modes. The characterization method has shown capability of measuring small loss tangents in ranges as low as 2×10^{-3} to 1×10^{-4} . Complex permittivity characterization results of a commercial proprietary ceramic compound in temperatures up to 600 °C and of aluminum oxide in temperatures up to 900 °C are presented.

Referring to the chipless sensor concepts, a short conclusion is given. As mentioned, the three concepts are based on three different approaches to realize the

6. Conclusion and Outlook

necessary separation between wanted tag signals and unwanted clutter. The concepts are realized and proofed with dedicated temperature sensor demonstrators. The clutter separations as well as the temperature sensing capabilities of these sensors are proofed in indoor measurement scenarios. The demonstrated measurement accuracies are generally dependent on the SIR and SNR of the measurement scenarios as well as on the sensor's resonance bandwidths. Therefore, increasing measurement accuracies are reached at lower reading distances and higher resonance quality factors.

The first one of the three sensor concepts is based on polarization separation between the wanted tag response and unwanted clutter. The realized sensor tag is setup as a Printed Circuit Board (PCB) with two patch antennas and a temperature-sensitive notch filter. Wireless measurements have demonstrated its sensing capability in temperatures between 20 °C and 110 °C. Under beneficial conditions in the anechoic chamber, the sensor shows a read range of more than 4.5 m. In practical applications, the range is more limited due to depolarization effects in the environment. Nevertheless, a measurement accuracy of 4 K is observed in two indoor scenarios for ranges up to 0.5 m.

The second sensor uses a harmonic radar concept to separate clutter and tag signals in frequency domain. The sensor tag converts the fundamental excitation signal to the first harmonic by exploiting the non-linearity of an unbiased diode. The tag design includes a temperature-sensitive narrowband Dielectric Resonator Antenna (DRA), as well as matching circuits for the complex diode impedance. Harmonic conversion losses as low as 19 dB for small input powers of -20 dBm have been achieved. The approach leads to a practically clutter-free tag detection and to the largest read ranges of 3.25 m in the measured indoor scenarios. Temperature measurement accuracies of better than 1.8 K are observed at reading distances of 1.5 m.

The third sensor concept is based on a time domain separation of wanted and unwanted signals. The sensor consists of a high- Q resonator, whose energy decays slower than the environment clutter. The corresponding demonstrator is setup as a ceramic DR cylinder, which is mounted on a metallic ground plane. This comparatively simple device has demonstrated wireless temperature measurements in ranges up to 800 °C, without requiring an optical line-of-sight. Due to its high resonance quality factor, the sensor offers measurement accuracies of at least 0.6 K at room temperature and 1.5 m reading distance. The sensor's read range is mainly limited by the environment clutter and only weakly influenced by the reader's transmit power. Read ranges of more than 2.25 m have been demonstrated in three different environment scenarios.

In addition to the realized sensors, a channel estimation method for chipless systems has been developed. This estimation method is used to suppress clutter interferences by measuring the backscatter response in two frequency bands adjacent to the tag resonance. The method has proved capability of allowing tag detection and significant error reduction in two scenarios with small SIRs values of 0.5.

To the author's best knowledge, the dynamic clutter suppression presents the

first published application of channel estimation means in chipless systems. Furthermore, it is noted that the DR sensor has been the first chipless sensor to prove operability in temperatures above 175 °C with read ranges significantly higher than 20 cm. Concerning operation at ‘usual’ temperatures below 100 °C, the DR sensor has demonstrated higher measurement accuracies with similar read ranges compared to chip-based RFID sensors at the current state-of-the art. Concerning operation at high temperatures, the DR sensor significantly exceeds the maximum temperature limit of commercially available SAW sensors, which is at 400 °C. Therefore, it appears as a promising candidate for industry-oriented wireless temperature sensing demands in harsh environments.

Regarding further developments of the topic, a couple of improvements and advancements shall be mentioned. The prototypes developed in this thesis have focused on proofs of the concepts. By adjusting resonance frequencies and sensor sensitivities, the prototypes can be designed to operate according to legal frequency regulations. A straightforward adaption would probably target the ISM bands at 2.4 GHz and 5.8 GHz or the UWB frequency ranges between 3.1 GHz and 10.6 GHz.

Regarding the DR sensor, one drawback of the setup is its resonance sensitivity to materials on the cylinder surface. This undesired sensitivity can cause measurement errors in application scenarios with dirt or liquids touching the sensor. It can probably be counteracted by a suitable radome, realized e.g. as a low-permittivity coating or a proper housing.

The maximum operating temperature of the DR sensor is mainly limited by the increasing dielectric losses at high temperatures. In order to further increase the sensor’s temperature range, other ceramic materials can be used. Here, materials with lower permittivities can show smaller loss tangents at high temperature, as already observed in the characterization of aluminum oxide. Currently ongoing research activities concerning the DR sensor include: efforts of a size reduction by increasing the operation frequency to mm-waves, the localization of the sensor within the environment by using advanced reader architectures, and the translation of the concept towards chipless RF identification by using multiple resonators.

Concerning the harmonic radar sensor, further investigations focusing on the non-linear element can extend its temperature range. The used diode represents currently the strongest temperature limitation of the sensor. The diode can be replaced by a metal-to-metal or metal-insulator-metal junction, which promises stable non-linearity in ranges significantly above 200 °C.

In contrast to the DR sensor, both the harmonic radar concept as well as the crosspolar concept do not generally require high- Q transducer materials. As a consequence, they offer promising application potential when only low- Q transducer materials are available. This can be the case at very high temperatures, or when other measurands shall be monitored wirelessly. The latter goal may include mechanical strain sensing with piezoelectric transducers, electric field strength sensing with BST, or gas sensing with transducing functional materials.

A. Appendix

Temperature Limit of a Doped Semiconductor

The operation of a semiconductor IC is based on the combination of doped semiconductor layers. The doping of a semiconductor adds a number of potential carriers to the material lattice. These carriers can either be donor electrons or acceptor holes, referring to n-type or p-type materials. Focusing on the former material, the total number of donor electrons in the lattice is denoted as N_D , and the number of majority carriers in the conduction band as n_C . Furthermore, a number of n_i intrinsic carriers can exist in the conduction band, which have been excited across the valence band of the intrinsic material. In dependence of temperature, a doped semiconductor can be in one of three different regimes, which are called the ionization or freeze-out region, the extrinsic region and the intrinsic region. They are plotted in Figure A.1 for a typical n-type Silicon semiconductor that is phosphorus doped with $N_D = 1 \times 10^{16} \text{ cm}^{-3}$ donor electrons. The regions are distinguished by the number of majority carriers n_c in relation to the number of doping carriers N_D and to the number of intrinsic carriers n_i :

- In the **freeze-out region** ($\vartheta \rightarrow 0 \text{ K}$) the available thermal energy is insufficient to excite intrinsic electrons across the band gap and only few to none electrons are released from donor sites, i.e., $n_c \rightarrow 0$ and $n_i \rightarrow 0$. Hence, current conduction is hardly possible; the semiconductor practically acts as an insulator.
- The **extrinsic region** is the standard operation region of an IC. All donor electrons are excited to the conduction band, i.e., the number of majority carriers is approximately equal to the total number of donor electrons in the lattice, $n_c \approx N_D$. The material now acts as an n-type, and the setup of space charge regions in p-n-junctions or metal-semiconductor junctions becomes possible. This, in turn, leads to the desired possibility of current control in diodes and transistors.
- When temperature increases, the increased thermal energy excites an increasing number of intrinsic electrons across the bandgap, i.e., $n_C > N_D$ and one enters the **intrinsic region** of the material. As the number of intrinsic electrons n_i now outnumbers the donor electrons, the material practically behaves as a conductor. [Pie96]

From the observation of carrier concentration, it becomes obvious that both an upper and a lower temperature limit exist for the operation of a semiconductor IC. As diodes and transistors rely on the combination of doped layers, the control of

A. Appendix

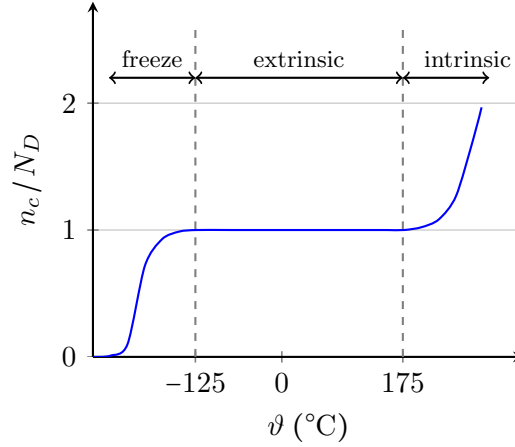


Figure A.1.: Typical majority-carrier concentration in a doped Silicon semiconductor versus temperature, based on [Pie96].

current and voltage in an IC is based on the behaviour of extrinsic carriers. Both p- and n-type materials become insulators or conductors when temperature limits are exceeded. Excess of the limits leads to malfunction of the device as it either stops operation or breaks down, eventually including thermal breakthrough and device destruction.

The temperature limits of a specific semiconductor material are dependent on its doping and its bandgap energy E_G . As the number of intrinsic carriers increases approximately proportional to the Boltzmann factor $e^{-E_G/2k\vartheta}$, with Boltzmann constant k and temperature ϑ , a large bandgap and a high doping will raise the intrinsic temperature limit. [TS02] names 175 °C as the upper application limit of usual silicon semiconductors circuits. Most commercially available ICs are specified to an even stricter maximum operation temperature of 125 °C (or less) for reliable operation [Wika].

Gallium arsenide (GaAs), silicon carbide (SiC) and gallium nitride (GaN) are used to develop high-temperature electronics as their bandgaps of 1.42 eV, 3.26 eV and 3.49 eV are significantly higher than the 1.12 eV of silicon.

B. Acronyms

B_p	Pulse bandwidth
D	Antenna directivity
\vec{E}	Electric field vector
f	Frequency
f_r	Resonance frequency
G	Antenna gain
γ_m	Material-dependent reflection factor
\vec{H}	Magnetic field vector
P_{Rx}	Receive/Rx power
P_{Tx}	Transmit/Tx power
Q_{rad}	Radiation quality factor
σ	Radar cross section
S	Rx Signal in frequency domain, $S(f)$
s	Rx Signal in time domain, $s(t)$
S_{nn}	Scattering parameter
t	Time
τ_ε	Temperature coefficient of the material permittivity
τ_f	Temperature coefficient of the resonance frequency
ϑ	Temperature
Z_w	Line impedance

B. Acronyms

BST	Barium Strontium Titanate
CMOS	Complementary Metal-Oxide-Semiconductor
CW	Continuous Wave
CE	Channel Estimation
EM	Electro-Magnetic
DR	Dielectric Resonator
DRA	Dielectric Resonator Antenna
DRS	Dielectric Resonator Sensor
FD	Frequency Domain
FFT	Fast Fourier Transform
HPBW	Half Power Beam Width
HRS	Harmonic Radar Sensor
IFFT	Inverse Fast Fourier Transform
IC	Integrated Circuit
IR	Infra-Red
OFDM	Orthogonal Frequency-Division Multiplexing
PCB	Printed Circuit Board
RFID	Radio-Frequency Identification
RF	Radio Frequency
RCS	Radar Cross Section
SAW	Surface Acoustic Wave
SIR	Signal to Interference Power Ratio
SNR	Signal to Noise Power Ratio
TD	Time Domain
TE	Transversal Electric
TL	Transmission Line
TM	Transversal Magnetic

UWB Ultra Wideband
VNA Vector Network Analyzer
XPS Crosspolar Sensor

Bibliography

- [AK11] E. M. Amin and N. Karmakar. “Development of a Chipless RFID Temperature Sensor Using Cascaded Spiral Resonators”. In: *IEEE Sensors Conference*. Oct. 2011.
- [AR13] F. Alimenti and L. Roselli. “Theory of zero-power RFID Sensors based on Harmonic Generation and Orthogonally Polarized Antennas”. In: *Progress In Electromagnetics Research*. Vol. 134. 2013, pp. 337–357.
- [Bac+12] R. Baccarelli, G. Orecchini, F. Alimenti, and L. Roselli. “Feasibility study of a fully organic, CNT based, harmonic RFID gas sensor”. In: *IEEE International Conference on RFID – Technologies and Applications*. Nov. 2012.
- [BBF11] A. Binder, G. Bruckner, and R. Fachberger. *SAW Transponder - RFID for Extreme Conditions, Deploying RFID - Challenges, Solutions, and Open Issues*. InTech, 2011. URL: <http://www.intechopen.com/books/deploying-rfid-challenges-solutions-and-open-issues/saw-transponder-rfid-for-extreme-conditions>.
- [Beh+13] R. Behanan, S. C. Moulfol, M. Call, G. Bernhardt, D. Frankel, R. J. Lad, and M. Pereira da Cunha. “Thin films and techniques for SAW sensor operation above 1000°C”. In: *IEEE International Ultrasonics Symposium*. July 2013, pp. 1013–1016.
- [Boc+14] J.-M. Boccard, T. Aftab, J. Hoppe, A. Yousaf, R. Hütter, and L. M. Reindl. “Far-Field Passive Temperature Sensing up to 700 °C using a Dielectric Resonator”. In: *IEEE Int. Conference on Wireless for Space and Extreme Environments*. Oct. 2014.
- [Bou+13] S. Bouaziz, F. Chebila, A. Traille, P. Pons, H. Aubert, and M.M. Tentzeris. “Novel Microfluidic Structures for Wireless Passive Temperature Telemetry Medical Systems Using Radar in Ka Band”. In: *IEEE Antennas and Wireless Propagation Letters* 11 (Jan. 2013), pp. 1536–1225.
- [CEG12] Haitao Cheng, Siamak Ebadi, and Xun Gong. “A Low-Profile Wireless Passive Temperature Sensor Using Resonator/Antenna Integration Up to 1000 °C”. In: *IEEE Antennas and Wireless Propagation Letters* 11 (2012), pp. 369–372.

Bibliography

- [Che+15] H. Cheng, X. Ren, S. Ebadi, Y. Chen, L. An, and X. Gong. “Wireless Passive Temperature Sensors Using integrated Cylindrical Resonator/Antenna for Harsh-Environment Applications”. In: *IEEE Sensors Journal* 15 (Mar. 2015), pp. 1453–1462.
- [Chu48] L. J. Chu. “Physical Limitations of Omni-Directional Antennas”. In: *Journal of Applied Physics* 19 (1948), pp. 1163–1175.
- [Coh68] S. B. Cohn. “Microwave Bandpass Filters Containing High-Q Dielectric Resonators”. In: *IEEE Transactions on Microwave Theory and Techniques* 16.4 (Apr. 1968), pp. 218–227.
- [Col+02] S. Coleri, M. Ergen, A. Puri, and A. Bahai. “Channel Estimation Techniques Based on Pilot Arrangement in OFDM Systems”. In: *IEEE Transactions on Broadcasting* 48 (3 2002), pp. 223–229.
- [Col01] R. E. Collin. *Foundations for Microwave Engineering*. Wiley-Interscience, 2001.
- [Con] Intechno Consulting. *Sensors Markets 2016 - Press Release*. accessed May 01, 2016. URL: <http://intechnoconsulting.com/ic/press/details/e-press-se2016-us.pdf>.
- [CTR] CTR Carinthian Tech Research AG. *Datasheet, RadFIT Sensors and Tags*. German. accessed June 11, 2015. URL: http://www.ctr.at/fileadmin/user_upload/2.F_E_Technologien/SAW/CTR_RadFIT_Datasheet_web.pdf.
- [Dan10] D. J. Daniels. *EM Detection of Concealed Targets*. New Jersey: Wiley, 2010.
- [EM] EM Microelectronic Marin S.A. *Datasheet EM4325*. accessed June 18, 2015. URL: <http://www.emmicroelectronic.com/sites/default/files/public/products/datasheets/4325-ds.pdf>.
- [FGL11] S. Fargeot, D. Guihard, and P. Lahitte. “Dielectric Characterization at High Temperature (1600°C) for Space Application”. In: *IEEE International Conference on Microwave Technology and Computational Electromagnetics*. May 2011.
- [Fin03] K. Finkensteller. *RFID Handbook*. West Sussex: Wiley, 2003.
- [Flu] Fluke Corporation. *Datasheet - TiX 1000*. German. accessed July 09, 2015. URL: <http://www.testequity.com/documents/pdf/TiX1000-TiX660-TiX640-ds.pdf>.
- [Ger+99] D. L. Gershon, J. P. Calame, Y. Carmel, T. M. Antonsen, and R. M. Hutcheon. “Open-Ended Coaxial Probe for High-Temperature and Broad-Band Dielectric Measurements”. In: *IEEE Transactions on Microwave Theory and Techniques* 47 (9 Sept. 1999).

- [Gha+13] M. Ghafourian, G. E. Bridges, Z. N. Abolghasem, and D. J. Thomson. “Wireless overhead line temperature sensor based on RF cavity resonance”. In: *Smart Materials and Structures* 22 (2013), pp. 1–7.
- [Gir+12] D. Girbau, A. Ramos, A. Lazaro, S. Rima, and R. Villarino. “Passive Wireless Temperature Sensor Based on Time Coded UWB Chipless RFID Tags”. In: *IEEE Transactions on Microwave Theory and Techniques* 60 (Sept. 2012), pp. 3623–3632.
- [Han81] R. C. Hansen. “Fundamental Limitations in Antennas”. In: *Proceedings of the IEEE* 69 (2 1981), pp. 170–182.
- [Har+91] N. H. Harris, J. R. Chow, R. L. Eisenhart, and B. M. Pierce. “Dielectric Properties of Ceramics at Microwave Frequencies”. In: *Proceedings of the Symposium on Microwave Theory and Application in Materials Processing*. Apr. 1991.
- [Har60] R. F. Harrington. “Effect of Antenna Size on Gain, Bandwidth, and Efficiency”. In: *Journal of Research of the National Bureau of Standards* 64 (1960), pp. 1–12.
- [HC60] B. W. Hakki and P. D. Coleman. “A Dielectric Resonator Method of Measuring Inductive Capacities in the Millimeter Range”. In: *IRE Transactions on Microwave Theory and Techniques* 8 (4 July 1960), pp. 402–410.
- [HK96] T. Hauschild and R. Knöchel. “Measurement of complex permittivity of solids up to 1000°C”. In: *IEEE MTT-S International Microwave Symposium Digest*. June 1996.
- [Ho88] W. W. Ho. “High-Temperature Dielectric Properties of Polycrystalline Ceramics”. In: *Symposium M – Microwave Processing of Materials I*. Vol. 124. MRS Proceedings. 1988.
- [Hor+98] J. Hornsteiner, E. Born, G. Fischerauer, and E. Riha. “Surface Acoustic Wave Sensors for high-temperature Applications”. In: *Proc. of the IEEE International Frequency Control Symposium*. May 1998, pp. 650–620.
- [Inc] Global Industry Analysts Inc. *Temperature Sensors: A Global Strategic Business Report*. accessed May 01, 2016. URL: http://www.strategyr.com/MarketResearch/Temperature_Sensors_Market_Trends.asp.
- [IR76] T. Itoh and R. Rudokas. “New Method for Computing the Resonant Frequencies of Dielectric Resonators”. In: *6th European Microwave Conference*. Sept. 1976, pp. 702–706.
- [Kam11] K.-D. Kammeyer. *Nachrichtenübertragung*. Vieweg und Teubner, 2011.

Bibliography

- [KEM96] D. Kajfez, A. Elsherbeni, and A. Mokaddem. “Higher order modes in dielectric resonators”. In: *Antennas and Propagation Society International Symposium*. July 1996, pp. 306–309.
- [KG98] D. Kajfez and P. Guillon. *Dielectric Resonators*. Noble, 1998.
- [KGJ84] D. Kajfez, A. W. Glisson, and J. James. “Computed Modal Field Distributions for Isolated Dielectric Resonators”. In: *IEEE Transactions on Microwave Theory and Techniques* 32.12 (Dec. 1984), pp. 1609–1616.
- [Kör98] Lászlò Körtvélyessy. *Thermoelement Praxis, 3. Auflage*. Essen: Vulkan Verlag, 1998.
- [Kub+12a] B. Kubina, C. Mandel, M. Schüßler, M. Sazegar, and R. Jakoby. “A Wireless Chipless Temperature Sensor utilizing an Orthogonal Polarized Backscatter Scheme”. In: *Proceedings of the 42nd European Microwave Conference*. Oct. 2012.
- [Kub+12b] B. Kubina, M. Schüßler, C. Mandel, H. Maune, D. Mueller, A. Zirotto, and R. Jakoby. “A coherent multi-reader approach to increase the working range of passive RFID systems”. In: *IEEE International Conference on RFID – Technologies and Applications*. 2012, pp. 350–355.
- [Kub+13a] B. Kubina, C. Mandel, M. Schüßler, and R. Jakoby. “Dynamic interference suppression for chipless wireless sensors: An out-of-band channel estimation approach”. In: *European Microwave Conference*. Oct. 2013.
- [Kub+13b] B. Kubina, M. Schüßler, C. Mandel, A. Mehmood, and R. Jakoby. “Wireless High-temperature Sensing with a Chipless tag based on a dielectric resonator antenna”. In: *IEEE Sensors Conference*. Nov. 2013.
- [Kub+14a] B. Kubina, C. Mandel, M. Schüßler, and R. Jakoby. “Dynamic Interference Suppression for Chipless Wireless Sensors based on an Out-of-Band Channel Estimation Method”. In: *International Journal of Microwave and Wireless Technologies* 6 (3 2014), pp. 353–360.
- [Kub+14b] B. Kubina, J. Romeu, C. Mandel, M. Schüßler, and R. Jakoby. “A Quasi-Chipless Wireless Temperature Sensor based on Harmonic Radar”. In: *Electronics Letters*. Vol. 50. Jan. 2014.
- [Kub+14c] B. Kubina, J. Romeu, C. Mandel, M. Schüßler, and R. Jakoby. “Design of a Quasi-Chipless Harmonic Radar Sensor for Ambient Temperature Sensing”. In: *IEEE Sensors Conference*. Nov. 2014.
- [Kub+15] B. Kubina, C. Mandel, M. Schüßler, and R. Jakoby. “Compact Quasi-Chipless Harmonic Radar Sensor with a Dielectric Resonator Antenna”. In: *IEEE International Microwave Symposium*. May 2015.
- [Lin89] J. F. Lindsey. “Radar Cross-section Effects Relating to a Horn Antenna”. In: *IEEE Transactions on Antennas and Propagation* 37 (2 Feb. 1989), pp. 257–260.

- [LSE11] C. Larsson, D. Sjöberg, and L. Elmkvist. “Waveguide Measurements of the Permittivity and Permeability at Temperatures of up to 1000°C”. In: *IEEE Transactions on Instrumentation and Measurement* 60 (8 Aug. 2011), pp. 2872–2880.
- [Man+11a] C. Mandel, B. Kubina, M. Schüßler, and R. Jakoby. “Passive Chipless Wireless Sensor for Two-Dimensional Displacement Measurement”. In: *41st European Microwave Conference* (Oct. 2011).
- [Man+11b] C. Mandel, H. Maune, M. Maasch, M. Sazegar M. and Schüßler, and R. Jakoby. “Passive Wireless Temperature Sensing with a BST-Based Chipless Transponder”. In: *German Microwave Conference*. Mar. 2011.
- [Man+11c] C. Mandel, H. Maune, M. Maasch, M. Sazegar, B. Kubina, M. Schüßler, and R. Jakoby. “Wireless Temperature Sensing with BST-Based Chipless Transponder Utilizing a Passive Phase Modulation”. In: *Frequenz* 65 (June 2011), pp. 225–231.
- [Man+12] C. Mandel, B. Kubina, M. Schüßler, and R. Jakoby. “Group-delay modulation with metamaterial-inspired coding particles for passive chipless RFID”. In: *IEEE International Conference on RFID – Technologies and Applications*. 2012.
- [Man+13] C. Mandel, B. Kubina, M. Schüßler, and R. Jakoby. “Metamaterial-inspired passive chipless radio-frequency identification and wireless sensing”. In: *Annals of Telecommunications* 68 (Aug. 2013), pp. 385–399.
- [Man+14] C. Mandel, C. Schuster, B. Kubina, M. Schüßler, and R. Jakoby. “Dual Frequency Selective Multiple Access With Quasi-Chipless/Powerless RFID Mixer Tags”. In: *IEEE Microwave and Wireless Components Letters* 24 (8 Aug. 2014), pp. 572–574.
- [Man+15] C. Mandel, M. Schüßler, M. Nickel, B. Kubina, R. Jakoby, M. Pöpperl, and M. Vossiek. “Higher order pulse modulators for time domain chipless RFID tags with increased information density”. In: *European Microwave Conference*. 2015, pp. 100–103.
- [Mat79] R. A. Matula. “Electrical Resistivity of Copper, Gold, Palladium and Silver”. In: *Journal of Physical and Chemical Reference Data* 8 (4 1979), pp. 1147–1298.
- [Mau+11] Holger Maune, Mohsen Sazegar, Yuliang Zheng, Xianghui Zhou, Andre Giere, Partick Scheele, Florian Paul, Joachim R. Binder, and Rolf Jakoby. “Nonlinear Ceramics for Tunable Microwave Devices, Part II: RF-characterization and component design”. In: *Microsystem Technologies* 17 (2 Feb. 2011).

Bibliography

- [MB94] R. K. Mongia and P. Bhartia. “Dielectric Resonator Antennas - A review and General Design Relations for Resonant Frequency and Bandwidth”. In: *International Journal of Microwave and Millimeter-Wave Computer-Aided Engineering* 4.3 (Aug. 1994), pp. 230–247.
- [Men+11] W. Menesklou, F. Paul, X. Zhou, H. Elsenheimer, J. R. Binder, and E. Ivers-Tiffée. “Nonlinear Ceramics for Tunable Microwave Devices, Part I: material properties and processing”. In: *Microsystem Technologies* 11 (2 Feb. 2011).
- [MI97] R. K. Mongia and A. Ittipiboon. “Theoretical and Experimental Investigations on Rectangular Dielectric Resonator Antennas”. In: *IEEE Transactions on Antennas and Propagation* 45.9 (Sept. 1997), pp. 1348–1356.
- [MSJ11] C. Mandel, M. Schüßler, and R. Jakoby. “A Wireless Passive Strain Sensor”. In: *IEEE Sensors Conference*. Oct. 2011, pp. 207–210.
- [NR06] P. V. Nikitin and K. V. S. Rao. “Theory and measurement of backscattering from RFID tags”. In: *IEEE Antennas and Propagation Magazine* 48 (6 2006), pp. 212–218.
- [NXP] NXP Semiconductors AG. *Datasheet UCODE G2iL*. accessed June 18, 2015. URL: http://www.nxp.com/documents/data_sheet/SL3S1203_1213.pdf.
- [Pal+15] V. Palazzi, C. Mariotti, F. Alimenti, M. Virili, G. Orecchini, P. Mezzanotte, and L. Roselli. “Demonstration of a chipless harmonic tag working as crack sensor for electronic sealing applications”. In: *Wireless Power Transfer* 2 (2 Sept. 2015), pp. 78–85.
- [Pie96] R. F. Pierret. *Semiconductor Device Fundamentals*. Addison-Wesley, 1996.
- [PK09] S. Preradovic and N. C. Karmakar. “Design of Fully Printable Planar Chipless RFID Transponder with 35-bit Data Capacity”. In: *Proceedings of the 39th European Microwave Conference*. Oct. 2009.
- [PK10] S. Preradovic and N. Karmakar. “Chipless RFID Tag with Integrated Sensor”. In: *IEEE Sensors Conference*. Nov. 2010.
- [Poz05] D. M. Pozar. *Microwave Engineering*. Wiley, 2005.
- [Ram+11] A. Ramos, A. Lazaro, D. Girbau, and R. Villarino. “Time-Domain Measurement of Time-Coded UWB Chipless RFID Tags”. In: *Progress in Electromagnetics Research* 116 (2011), pp. 313–331.
- [REC] RECCO AB. *Avalanche Awareness provided by RECCO, White Book*. accessed March 01, 2016. URL: http://recco.com/upload/Global/Images/Downloads/WB%5C_English.pdf.

- [Ril+96] J. R. Riley, A. D. Smith, D. R. Reynolds, A. S. Edwards, J. L. Osborne, I. H. Williams, N. L. Carreck, and G. M. Poppy. “Tracking bees with harmonic radar”. In: *Nature* 379 (Jan. 1996), pp. 29–30.
- [SAB] SAB Bröckskes GmbH. *Mantel - Thermoelement und Mantel - Widerstandsthermometer*. German. accessed July 08, 2015. URL: https://www.sab-kabel.de/fileadmin/user_upload/pdf/catalog_dt/Thermotechnik_dt/Thermoelemente/MTE_und_MWT.pdf.
- [Sch+13] M. Schüßler, B. Kubina, C. Mandel, and R. Jakoby. “Readout scheme for resistive chipless wireless sensors”. In: *IEEE Sensors Conference*. 2013.
- [Sch+14a] M. Schüßler, C. Kohler, A. Wiens, B. Kubina, C. Mandel, A. Friedrich, J. Binder, and R. Jakoby. “Screen Printed Chipless Wireless Temperature Sensor based on BST Thick Film Capacitor”. In: *IEEE Sensors Conference*. Nov. 2014.
- [Sch+14b] M. Schüßler, C. Mandel, B. Kubina, and R. Jakoby. “Realization Concepts for Chipless Wireless Temperature Sensing”. In: *Proceedings of the 17th ITG/GMA Symposium; Sensors and Measuring Systems*. 2014.
- [Sch+98] G. Scholl, F. Schmidt, T. Ostertag, L. Reindl, H. Scherr, and U. Wolff. “Wireless Passive SAW Sensor Systems for Industrial Applications”. In: *Proc. of the IEEE International Frequency Control Symposium*. May 1998, pp. 595–601.
- [Seb08] M. T. Sebastian. *Dielectric Materials for Wireless Communications*. Elsevier, 2008.
- [Sha+16] J. F. Shackelford, Y.-H. Han, S. Kim, and S.-H. Kwon. *CRC Materials Science and Engineering Handbook*. CRC Press, 2016.
- [She09] J. Sheen. “Comparisons of microwave dielectric property measurements by transmission/reflection techniques and resonance techniques”. In: *Measurement Science and Technology* 20 (Jan. 2009).
- [Sko08] M. Skolnik. *Radar Handbook*. Mc Graw Hill, 2008.
- [SP09] Sean Scott and Dimitrios Peroulis. “A Capacitively-Loaded MEMS Slot Element for Wireless Temperature Sensing of up to 300°C”. In: *IEEE MTT-S International Microwave Symposium Digest*. June 2009.
- [Tan+03] A. K. Tangantsev, V. O. Sherman, K. F. Astafiev, J. Venkatesh, and N. Setter. “Ferroelectric Materials for Microwave Tunable Applications”. In: *Journal of Electroceramics* 11 (Nov. 2003), pp. 5–66.
- [TCB09] D. J. Thomson, D. Card, and G. E. Bridges. “RF Cavity Passive Wireless Sensors With Time-Domain Gating-Based Interrogation for SHM of Civil Structures”. In: *IEEE Sensors Journal* 9.11 (Nov. 2009).

Bibliography

- [TCI] TCI Ceramics. *Materials: Dielectric*. accessed March 10, 2016. URL: http://www.magneticsgroup.com/m_dielec.htm.
- [Tha+10a] T. T. Thai, F. Chebila, J.M. Mehdi, P. Pons, H. Aubert, G.R. DeJean, M.M. Tentzeris, and R. Plana. “Design and Development of a Millimetre-Wave Novel Passive Ultrasensitive Temperature Transducer for Remote Sensing and Identification”. In: *European Microwave Conference*. Sept. 2010.
- [Tha+10b] T. T. Thai, M. Jatlaoui, P. Pons, H. Aubert, M. Tentzeris, G. DeJean, and R. Plana. “A Novel Passive Wireless Ultrasensitive RF Temperature Transducer for Remote Sensing”. In: *IEEE MTT-S International Microwave Symposium Digest*. May 2010.
- [Tra+11a] A. Traille, S. Bouaziz, S. Pinon, P. Pons, H. Aubert, A. Boukabache, and M. Tentzeris. “A novel wireless passive temperature sensor utilizing microfluidic principles in millimeter-wave frequencies”. In: *IEEE Sensors Conference*. Oct. 2011.
- [Tra+11b] A. Traille, S. Bouaziz, S. Pinon, P. Pons, H. Aubert, A. Boukabache, and M. Tentzeris. “A wireless Passive RCS-based Temperature Sensor using Liquid Metal and Microfluidics Technologie”. In: *European Microwave Conference*. Oct. 2011.
- [TS02] Ulrich Tietze and Christoph Schenk. *Halbleiter - Schaltungstechnik*. Berlin: Springer, 2002.
- [Var+91] V. V. Varadan, R. D. Hollinger, D. K. Ghodgaonkar, and V. K. Varadan. “Free-Space, Broadband Measurements of High- Temperature, Complex Dielectric Properties at Microwave Frequencies”. In: *IEEE Transactions on Instrumentation and Measurement* 40 (5 Oct. 1991), pp. 842–846.
- [Ven+14a] A. Vena, L. Sydänheimo, M.M. Tentzeris, and L. Ukkonen. “Fully Inkjet Printed Wireless and Chipless Sensor for CO₂ and Temperature Detection”. In: *IEEE Sensors Journal* 15 (July 2014), pp. 89–99.
- [Ven+14b] A. Vena, L. Sydänheimo, L. Ukkonen, and M.M. Tentzeris. “A fully inkjet-printed chipless RFID gas and temperature sensor on paper”. In: *IEEE RFID Technology and Applications Conference*. Sept. 2014.
- [Ves+97] A. Vescan, I. Daumiller, P. Gluche, W. Ebert, and E. Kohn. “Very high temperature operation of diamond schottky diode”. In: *IEEE Electron Device Letters* 18 (11 1997), pp. 556–558.
- [Vol+08] M. A. Volz, B. Crowgey, G. L. Charvat, E. Rothwell, and L. Kempel. “Recent Developments in Miniaturized Planar Harmonic Radar Antennas”. In: *Antennas Measurement Techniques Association Conference*. Nov. 2008.

- [VPT11] A. Vena, E. Perret, and S. Tedjini. “Chipless RFID Tag Using Hybrid Coding Technique”. In: *IEEE Transactions on Microwave Theory and Techniques* 59.12 (2011), pp. 3356–3364.
- [VPT13] A. Vena, E. Perret, and S. Tedjini. “A Depolarizing Chipless RFID Tag for Robust Detection and Its FCC Compliant UWB Reading System”. In: *IEEE Transactions on Microwave Theory and Techniques* 61.8 (2013), pp. 2982–2993.
- [VZ00] O. G. Vendik and S. P. Zubko. “Ferroelectric phase transition and maximum dielectric permittivity of displacement type ferroelectrics (Ba(x)Sr(1-x)TiO₃)”. In: *Journal of Applied Physics* 88.9 (2000), pp. 5343–5350.
- [Wika] Wikipedia, the free encyclopedia. *High performance plastics*. accessed July 08, 2015. URL: <http://de.wikipedia.org/wiki/Eigenleitungsdichte>.
- [Wikb] Wikipedia, the free encyclopedia. *High performance plastics*. accessed July 08, 2015. URL: http://en.wikipedia.org/wiki/High_performance_plastics.
- [Yin+10] J. Yin, J. Yi, M. K. Law, Y. Ling, M. C. Lee, K. P. Ng, B. Gao, H. C. Luong, A. Bermak, M. Chan, W.-H. Ki, C.-Y. Tsui, and M. Yuen. “A System-on-Chip EPC Gen-2 Passive UHF RFID Tag With Embedded Temperature Sensor”. In: *IEEE Journal of Solid-State Circuits* 45 (11 2010), pp. 2404–2420.
- [Zai+14] S. H. Zainud-Deen, M. A. Abo-Elhassan, H. A. Malhat, and K. H. Awadalla. “Dual-Polarized Chipless RFID Tag with Temperature Sensing Capability”. In: *National Radio Science Conference (NRSC)*. Apr. 2014.

Own Publications

- [Kub+12a] B. Kubina, C. Mandel, M. Schüßler, M. Sazegar, and R. Jakoby. “A Wireless Chipless Temperature Sensor utilizing an Orthogonal Polarized Backscatter Scheme”. In: *Proceedings of the 42nd European Microwave Conference*. Oct. 2012.
- [Kub+12b] B. Kubina, M. Schüßler, C. Mandel, H. Maune, D. Mueller, A. Ziroff, and R. Jakoby. “A coherent multi-reader approach to increase the working range of passive RFID systems”. In: *IEEE International Conference on RFID – Technologies and Applications*. 2012, pp. 350–355.
- [Kub+13a] B. Kubina, C. Mandel, M. Schüßler, and R. Jakoby. “Dynamic interference suppression for chipless wireless sensors: An out-of-band channel estimation approach”. In: *European Microwave Conference*. Oct. 2013.
- [Kub+13b] B. Kubina, M. Schüßler, C. Mandel, A. Mehmood, and R. Jakoby. “Wireless High-temperature Sensing with a Chipless tag based on a dielectric resonator antenna”. In: *IEEE Sensors Conference*. Nov. 2013.
- [Kub+14a] B. Kubina, C. Mandel, M. Schüßler, and R. Jakoby. “Dynamic Interference Suppression for Chipless Wireless Sensors based on an Out-of-Band Channel Estimation Method”. In: *International Journal of Microwave and Wireless Technologies* 6 (3 2014), pp. 353–360.
- [Kub+14b] B. Kubina, J. Romeu, C. Mandel, M. Schüßler, and R. Jakoby. “A Quasi-Chipless Wireless Temperature Sensor based on Harmonic Radar”. In: *Electronics Letters*. Vol. 50. Jan. 2014.
- [Kub+14c] B. Kubina, J. Romeu, C. Mandel, M. Schüßler, and R. Jakoby. “Design of a Quasi-Chipless Harmonic Radar Sensor for Ambient Temperature Sensing”. In: *IEEE Sensors Conference*. Nov. 2014.
- [Kub+15] B. Kubina, C. Mandel, M. Schüßler, and R. Jakoby. “Compact Quasi-Chipless Harmonic Radar Sensor with a Dielectric Resonator Antenna”. In: *IEEE International Microwave Symposium*. May 2015.
- [Man+11a] C. Mandel, B. Kubina, M. Schüßler, and R. Jakoby. “Passive Chipless Wireless Sensor for Two-Dimensional Displacement Measurement”. In: *41st European Microwave Conference* (Oct. 2011).
- [Man+11c] C. Mandel, H. Maune, M. Maasch, M. Sazegar, B. Kubina, M. Schüßler, and R. Jakoby. “Wireless Temperature Sensing with BST-Based Chipless Transponder Utilizing a Passive Phase Modulation”. In: *Frequenz* 65 (June 2011), pp. 225–231.

Own Publications

- [Man+12] C. Mandel, B. Kubina, M. Schüßler, and R. Jakoby. “Group-delay modulation with metamaterial-inspired coding particles for passive chipless RFID”. In: *IEEE International Conference on RFID – Technologies and Applications*. 2012.
- [Man+13] C. Mandel, B. Kubina, M. Schüßler, and R. Jakoby. “Metamaterial-inspired passive chipless radio-frequency identification and wireless sensing”. In: *Annals of Telecommunications* 68 (Aug. 2013), pp. 385–399.
- [Man+14] C. Mandel, C. Schuster, B. Kubina, M. Schüßler, and R. Jakoby. “Dual Frequency Selective Multiple Access With Quasi-Chipless/Powerless RFID Mixer Tags”. In: *IEEE Microwave and Wireless Components Letters* 24 (8 Aug. 2014), pp. 572–574.
- [Man+15] C. Mandel, M. Schüßler, M. Nickel, B. Kubina, R. Jakoby, M. Pöpperl, and M. Vossiek. “Higher order pulse modulators for time domain chipless RFID tags with increased information density”. In: *European Microwave Conference*. 2015, pp. 100–103.
- [Sch+13] M. Schüßler, B. Kubina, C. Mandel, and R. Jakoby. “Readout scheme for resistive chipless wireless sensors”. In: *IEEE Sensors Conference*. 2013.
- [Sch+14a] M. Schüßler, C. Kohler, A. Wiens, B. Kubina, C. Mandel, A. Friedrich, J. Binder, and R. Jakoby. “Screen Printed Chipless Wireless Temperature Sensor based on BST Thick Film Capacitor”. In: *IEEE Sensors Conference*. Nov. 2014.
- [Sch+14b] M. Schüßler, C. Mandel, B. Kubina, and R. Jakoby. “Realization Concepts for Chipless Wireless Temperature Sensing”. In: *Proceedings of the 17th ITG/GMA Symposium; Sensors and Measuring Systems*. 2014.

Supervised Student Theses

- **A. Kimmerle:** *Entwurf schmalbandiger Patchantennen für einen passiven drahtlosen Temperatursensor*, Master Thesis, January 2014
- **T. Schreck:** *Drahtlose Temperaturmessung mit Chiplosen RFID-Mixer-Tags*, Master Thesis, November 2013
- **J. Romeu:** *Design of a Chipless Harmonic Radar Temperature Sensor*, Master Thesis, July 2013
- **M. Wahib:** *Fundamental investigations of electromagnetic backscattering of Ultra-wideband passive chipless time-coded RFID tags for remote identification and temperature sensing applications*, Bachelor Thesis, July 2013
- **C. Schuster:** *Design of a Passive Chipless RFID Mixer Tag based on Planar Multi-Band Slot Antennas*, Bachelor Thesis, December 2012
- **S. Pongratz:** *Modellierung eines passiven chiplosen RFID-Systems unter besonderer Berücksichtigung des Übertragungskanal*, Studienarbeit, December 2011

Erklärung laut §9 PromO

Ich versichere hiermit, dass ich die vorliegende Dissertation allein und nur unter Verwendung der angegebenen Literatur verfasst habe. Die Arbeit hat bisher noch nicht zu Prüfungszwecken gedient.

Darmstadt, 12. Juli 2016
